Summer 2019

Electrodeposition of epitaxial metal thin films on silicon for energy conversion and flexible electronics

Qingzhi Chen

Department: Chemistry

ELECTRODEPOSITION OF EPITAXIAL METAL THIN FILMS ON SILICON FOR ENERGY CONVERSION AND FLEXIBLE ELECTRONICS

by

QINGZHI CHEN

A DISSERTATION

Presented to the Faculty of the Graduate School of the

MISSOURI UNIVERSITY OF SCIENCE AND TECHNOLOGY

In Partial Fulfillment of the Requirements for the Degree

DOCTOR OF PHILOSOPHY

in

CHEMISTRY

2019

Approved by

Jay A. Switzer, Advisor
Nicholas Leventis
Jeffrey G. Winiarz
Manashi Nath
F. Scott Miller

PUBLICATION DISSERTATION OPTION

This dissertation consists of the following three published articles:

Paper I: Photoelectrochemistry of ultrathin, semitransparent, and catalytic gold films electrodeposited epitaxially onto n-silicon (111), found on pages 21 - 52, is published in *ACS Applied Materials & Interfaces* 2018, 10(25), pp 21365–21371.

Paper II: Epitaxial lift-off of electrodeposited single-crystal gold foils for flexible electronics, found on pages 53 - 82, is published in *Science*, 2017, 355 (6330), pp 1203-1206.

Paper III: Electrodeposition of nanometer-thick epitaxial films of silver onto single-crystal silicon wafers, founds on pages 83 - 102, is published in *Journal of Material Chemistry C*, 2019, 7 (24), pp 1720–1725.

ABSTRACT

This research focuses on epitaxial electrodeposition of two coinage metals: Au and Ag thin films on the silicon surface and their applications in flexible electronics and energy conversion and storage. The first paper: *Photoelectrochemistry of ultrathin, semi-transparent, and catalytic gold films electrodeposited epitaxially onto n-silicon (111)* describes the epitaxial electrodeposition of Au thin films on n-type Si using a simple $HAuCl_4$ bath and the photoelectrochemical properties of the Au-Si junction barrier. The effect of the Au layer on the interfacial energetics as well as the stability of the photoelectrode as a function of the Au coverage/thickness is determined in a regenerative cell. The second paper: *Epitaxial lift-off of electrodeposited single-crystal gold foils for flexible electronics* shows a technique for epitaxial lift-off of Au foils as semi-transparent, flexible and single crystal-like substrates for flexible electronics. A Au thin film is first deposited on Si and then photooxidation is performed followed by a lift-off process. The Au foils exhibit a low sheet resistance down to 7 ohms per square and show only a 4% increase in resistance after 4000 bending cycles. A flexible organic light-emitting diode that was spin-coated on a Au foil exploited the transmittance and flexibility of the foil. The third paper: *Electrodeposition of nanometer-thick epitaxial films of silver onto single-crystal silicon wafers* introduces the electrodeposition of epitaxial Ag thin films on n-type Si of three different low-index orientations from an acetate bath. A comparison of silver acetate electrolyte and cyanide electrolyte was also performed, showing advantages of the acetate bath over the cyanide bath for growth of epitaxial films of Ag on Si surfaces.

ACKNOWLEDGMENTS

I would like to express my heartful thanks to my advisor, Prof. Jay A. Switzer, since it has been a great honor and privilege working with him and with the group, and for his conscientious guidance throughout my six years of research life. I would also like to thank my committee members, Prof. Nicholas Leventis, Prof. Jeffrey G. Winiarz, Prof. Manashi Nath, and Prof. F. Scott Miller, for their perceptive suggestions during my study and research. Dr. Eric W. Bohannan offered exceptional assistance in X-Ray diffraction measurements. Dr. Xiaoqing He and Dr. Jingjing Qing provided encouraging technical support in TEM imaging. Thanks go to all the faculty and staff at the Materials Research Center (MRC) as well for their efforts to create an efficient and friendly working environment in MRC.

I would like to thank all my friends and my lab mates: Dr. Allen Liu, Dr. Naveen K. Mahenderkar, Meagan V. Kelso, and Dr. Caleb M. Hull. They have all been really supportive in the lab. I would also like to thank my family for their endless motivation and support to me. Finally. funding for this work has been provided by the U.S. Department of Energy, Office of Basic Science under Grant No. DE-FG02- 08ER46518.

TABLE OF CONTENTS

Page

LIST OF ILLUSTRATIONS

SECTION Page

PAPER II

PAPER III

1. INTRODUCTION

1.1. ELECTRODEPOSITION

Electrodeposition (also known as electroplating) has been one of the most commonly used methods for material fabrication, thin film synthesis, surface treatment and decoration for more than a century.[1–4] As a simple, inexpensive and sophisticated soft solution-based method, electrodeposition has the capability for tuning many properties of the deposited material including chemical composition, surface morphology, porosity, hardness, epitaxy, chirality, etc. simply by varying a few parameters such as temperature, solution pH, potential and current densities.[5–11] This gives electrodeposition a great advantage over some traditional thin film synthesis methods such as physical vapor deposition (PVD), chemical vapor deposition (CVD), molecular beam epitaxy (MBE) and atomic layer deposition (ALD), which usually produce thin films with limited composition and features, as well as involve high temperature and high vacuum conditions and need expensive equipment.[12–19] Moreover, combined with the Lithographie Galvanoformung Abformung (lithographic electroforming fabrication, LIGA) technique, electrodeposition could go one step beyond its conventional surface nature and provide a path to producing cheaper micro-electromechanical systems (MEMS) parts compared with current micro-fabricating techniques, and provide more precise micro features compared with 3D printing fabrication.[20–23]

A major application of electrodeposition is to produce a variety of metals and alloys, from simple metals such as Au, Cu and Ag to complicated alloys such as the Fe-Co-Ni ternary alloy.[24–30] The mechanism of metal deposition usually includes metal ion

reduction from higher oxidation states to zero oxidation state on the electrode surface and can be expressed as follows:

$$M^{n+} + ne^- \rightarrow M \quad (1)$$

However, electrodeposition is not confined to this category only. There are studies focused also on the electroforming of catalysts, semiconductors and metal oxides or ceramics.[9,31–33] The mechanism of electrodeposition of metal oxides or ceramics generally involves two steps: a charge transfer between the electrode and the electrochemically active species at given potential/current followed by a non-redox chemical reaction. Such mechanism is called an electrochemical-chemical (EC) mechanism. Two typical applications taking advantage of this process are the deposition of amphoteric metal oxides (e.g., ZnO) by generating either base or acid electrochemically at the electrode surface in a solution containing dissolved metal ion,[7] and the deposition of multivalent metal oxides or hydroxides by generating unstable metal complex species by oxidizing or reducing a stable metal complex followed by a chemical precipitation of the final product (e.g., Fe_3O_4, Cu_2O, Co_3O_4 and $Co(OH)_2$].[33–36] Taking Fe_3O_4 as an example, this compound can be deposited by reducing Fe(III)-TEA (triethanolamine) complex ion in an alkaline solution:

$$Fe(TEA)^{3+} + e^- \rightarrow Fe(TEA)^{2+} \quad (2)$$

$$Fe(TEA)^{3+} + 8OH^- + 2Fe(TEA)^{2+} \rightarrow Fe_3O_4 + 3TEA + 4H_2O \quad (3)$$

In this dissertation, discussion will mainly focus on the electrodeposition of two noble metals, gold (Au) and silver (Ag) on a special surface – silicon (Si).

1.1.1. Electrodeposition of Au on Si. Besides the demands of decoration, Au electrodeposition has become more and more devoted to the electronics industry and specific surface science and technologies since the 1970's.[37–40] A general electrochemical

reaction of Au deposition can be written as:

$$Au^{3+} + 3e^- \rightarrow Au,\ E^0 = 1.498\ V\ vs.\ NHE \quad (4)$$

As an industrial standard process, cyanide and sulfite Au plating baths are most frequently used as electrolyte solutions for Au deposition. These solutions usually generate smooth, ductile and bright Au deposits with low stress.[41] However, most studies and applications based on these methods are still performed on metal surfaces, and are not deposited epitaxially (the importance of being epitaxial will be discussed later). Allongue and co-workers pioneered the deposition of epitaxial metals on semiconductors by depositing an ultra-thin and smooth layer of Au on miscut Si (111) surface using very negative deposition potentials in a solution containing very dilute $HAuCl_4$.[24] Switzer's group further developed this method and had brought it to a new level: An ultra-thin epitaxial Au layer was deposited onto Si with three different orientations of (111), (110) and (100) using a solution containing the same Au salt. These Au on Si samples can be used as a proxy for single-crystal Au, and thin Au deposited on n-Si(111) can be further used as photoanodes for photoelectrochemical regenerative cells.[25,42] Furthermore, a lift-off process was developed for the thin Au layer to produce a single-crystal Au foil for flexible electronics.[43]

Electrodeposition can be performed on any conductive or semiconductive surfaces. However the Si surface is a special semiconductive surface that requires additional attention. The active chemical nature of this surface causes Si always to develop a passivating thin native oxide layer. Thus, the pretreatment of Si surfaces before electrodeposition is crucial to the whole process. A 5% hydrofluoric acid (HF) solution is used to etch the Si surface for 30 s to remove the native oxide layer, followed by soaking in hot water (85 °C or above) for 15 min and an additional 10s 5% HF etching step to form

a hydrogen-terminated layer. This layer is capable to protect the Si surface from O_2 oxidation for a few hours and makes subsequent epitaxial deposition feasible. Besides surface treatment, the back contact is also important, especially for those Si with low doping densities, or so called non-degenerate Si. A low work function metal must be applied to the back of n-Si to form an ohmic contact. This is usually achieved by sputtering a thin layer of Al or by brush-painting an indium-gallium eutectic alloy. A Ag wire along with Ag paste is used to form the electrical contact and silicone paste sealing is used to insulate the backside of the sample.

A plating solution containing 0.1 mM $HAuCl_4$, 0.1 M K_2SO_4, 1 mM KCl and 1 mM H_2SO_4 is used in the electrodeposition process of Au on Si, and the pH of the solution is adjusted to 3 by HCl. A pre-polarizing process with a constant potential of -1.9 V vs. satd. Ag/AgCl is applied while depositing. The pre-polarizing step is carried out to prevent oxidation of Si surface when it is submerged into the solution and this negative potential is not only to prevent the Si oxidation (it has about a 0.62 V overpotential for the reduction reaction of SiO_2 to Si) but also to involve the hydrogen evolution reaction (HER) which serves as surface agitation and increases the surface smoothness of deposited Au layer. The deposition time varies from 10 s to 30 min based on the desired thickness. A Au coil is used as the counter electrode and a stirred solution with 200 rpm is used during the deposition. The detail of deposited epitaxial Au layer on Si serving as photoelectrodes or being lifted-off as substrates for flexible electronics will be discussed later in this introduction and can be found in Paper I and Paper III.

1.1.2. Electrodeposition of Ag on Si. Ag is one of the most important metals in the electronic industry and it has the lowest electrical resistance and outstanding optical

properties. Research has shown that Ag thin films/nanostructures are ideal for fabrication of plasmonic devices, surface enhanced Raman scattering substrates, surface catalysts and highly selective absorbers/emitters.[44–49] Conventional Ag electrodeposition requires cyanide as a complexing agent to produce smooth, dense and dendrite-free deposits, and have been developed over the past hundred years.[3] A general electrochemical equation of this process can be written as:

$$Ag(CN)_2^- + e^- \rightarrow Ag + 2CN^- \quad (5)$$

The cyanide electrolyte bath however, is known to be toxic and harmful to the environment. There have been several non-cyanide Ag deposition techniques developed and alternative organic additives such as tartaric acid, uracil, HEDTA, hydroxypyridine. can be added to the electrolyte to achieve a similar effect to the cyanide salt.[50–54] Nevertheless, these extra additives increase the cost and sometimes make the plating solution unstable and hard to maintain. In Paper III of this dissertation, epitaxial Ag thin films on Si(111), (110) and (100) were electrodeposited from a different path in analogy to the Au deposition process introduced above, and a simple silver acetate bath was used.

The same procedure for Si surface treatment and back contact introduced above is applied to the Si substrate prior to the electrodeposition of Ag films. A plating solution containing 0.1 mM AgOAc, 0.1 M K_2SO_4, 1 mM KOAc and 1 mM H_2SO_4 with a pH of 3.6 is prepared. Before anything is deposited on the Si surfaces, a linear sweep voltammetry (LSV) scan is performed on a plain Au electrode from the open circuit potential (OCP) towards more negative potentials at a scan rate of 10 mV s^{-1} in a stirred solution under 200 rpm rotation rate. The polarization curve (shown in Paper II) suggests that Ag(I) reduction reaction starts at about -0.1 V vs. Hg/Hg_2SO_4. The deposition potential of -2.34 V vs.

Hg/Hg_2SO_4 was adopted to avoid Si oxidation during deposition and to evolve hydrogen. The X-ray Laue oscillation analysis shows that a thickness of about 10 nm can be obtained for Ag deposited for 10 minutes. As a comparison to the traditional Ag plating procedure as well as an attempt of acquiring smoother film on Si, a cyanide bath containing 2.4 mM AgCl, 8.5 mM KCN, and 0.1 M K_2CO_3 was also used for deposition. However, epitaxial Ag films were obtained only on Si(111) surfaces from the cyanide bath.

1.2. EPITAXY

The word "epitaxy" is made up with two Greek roots – *epi*, "above" and *taxy*, derived from *taxis* which means "an ordered manner." We define epitaxy as the growth of crystalline deposits on an ordered substrate where the crystalline orientation of the deposits is controlled by the substrate orientation. The substrate is usually a piece of single crystal or crystals made up with multiple grains but possess out-of-plane and in-plane order. Based on the material composition difference between the deposits and the substrate, this concept can be further divided into homoepitaxy and heteroepitaxy. Homoepitaxy refers to the process in which the same material is grown onto the substrate and heteroepitaxy refers to those in which different material is grown. Homoepitaxy has a long history of being investigated both theoretically and practically, as one of its applications covers the most important process in the semiconductor industry – growth of bulk single crystalline Si or other types of semiconductor by the Czochralski method, in which a small seed crystal is dipped from top into the free melt surface of the feed material and the seed is slowly withdrawn from the melt, leading the melt to crystallize at the interface.[55] Heteroepitaxy however, provides more diverse approaches and possibilities for single crystalline material

synthesis and will be mainly emphasized in this work. Typically, in the case of heteroepitaxy, the less mismatch in lattice parameter between deposited material and the substrate, the less defects are produced in the interface and less strain the deposits would have. Here, the lattice mismatch is defined by the equation below:

$$\text{mismatch} = \frac{a_F - a_S}{a_S} \times 100\% \quad (6)$$

where, a_F is the lattice parameter of the film deposited and a_S is the lattice parameter of the substrate. In general, epitaxially grown thin films exhibits less grain boundaries, less defects and less electron-hole recombination sites and thus can provide better electronic or optical properties.[25,43] An instance can be found in Paper II where epitaxially deposited Cu_2O films present a diode quality factor *n* of 1.6 in a diode produced using a rectifying contact with InGa eutectic. This *n* value is much closer to the ideal *n* = 1 than the polycrystalline Cu_2O film deposited on stainless steel which means less electron-hole recombination.

Epitaxial growth can be conducted by a) conventional vapor-phase epitaxy methods such as MBE, CVD, PVD and pulsed laser deposition (PLD), b) liquid-phase epitaxy (LPE, commonly used in semiconductor industry) and c) soft solution-based methods such as electrodeposition, hydrothermal processing,[56] chemical bath deposition[57,58] or even simple dip-coating methods.[59,60] The mechanism of vapor-phase epitaxial growth and LPE has been extensively studied over time.[15,61–65] However, the mechanism of solution-based heteroepitaxial growth is less well understood and is under research. In fact, the lattice mismatch factor mentioned above is over-simplified and cannot explain some epitaxial growth system, such as epitaxial deposition of Au and Ag on Si. The lattice mismatch between Au/Ag and Si can be calculated using Equation (5) to be about -24.9%. This is a

very large value for 1×1 lattice epitaxial growth. An expanded lattice mismatch model needs to be invoked, known as coincident site lattices (CSLs). Figure 1.1 shows the interface model of Ag on Si (111) and the diagrammatic illustration of the CSL. As shown by the red triangles 4 unit meshes of Ag lattice coincides with 3 unit meshes of Si lattice, and the mismatch is reduced from -24.9% to 0.13%. These CSLs make the epitaxial growth of Ag on Si plausible and create very limited in-plane compressive stress to the Ag film.[27]

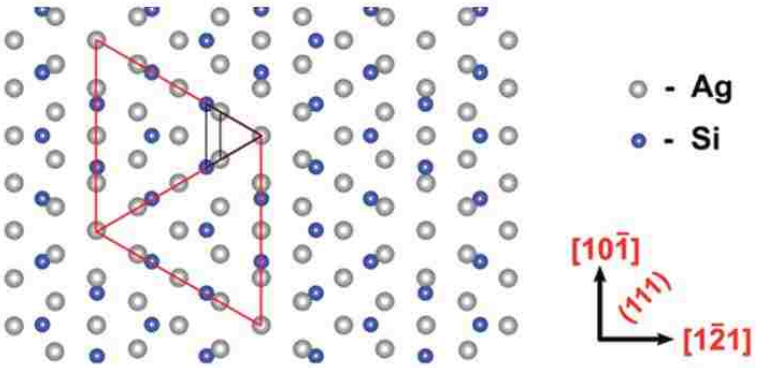

Figure 1.1. The atomic interfacial model of Ag on Si

There are several techniques to characterize epitaxially grown thin films. Cross sectional hi-resolution transmission electron microscopy (HRTEM) can visualize the lattice structure and give interfacial lattice fringe images. Crystal lattice *d*-spacing values can be measured directly from the HRTEM images thus they can be used to determine the crystalline orientation of the materials and to interpret the epitaxial relationship between the films and the substrate. A selected area electron diffraction (SAED) pattern can be further obtained from TEM sometimes to help analyze the epitaxial relationship as well. However, a focused ion beam (FIB) lift-off process is usually required prior to conducting

the TEM analysis in order to obtain a cross-section with the right thickness (typically about 100 nm or less), which could be time consuming, involving damage to the sample and requires additional equipment such as an SEM. X-ray diffraction (XRD) azimuthal scans or pole figures on the other hand, provide easy and non-destructive information on the heteroepitaxy. Different from the symmetric scan used commonly in powder X-ray diffraction (PXRD), the incident angle θ is fixed to a Bragg angle where Bragg's law is fulfilled:

$$n\lambda = 2d\sin\theta \tag{7}$$

where, λ is the X-ray wavelength, d is the lattice spacing and θ is the diffraction angle and n is the diffraction order. Then the sample is tilted at an angle χ from 0° to 90° and rotated through azimuthal angles φ from 0° to 360°. Diffraction signals collected from the azimuthal φ scans at each tilt angle, χ, are used to construct a pole figure. A diagrammatic sketch is shown in Figure 1.2 below to display the measurement geometry for the pole figures. After a pole figure is acquired, the crystalline stereographic projections of the substrate and the film which reveal the expected peak (spot) position can be used to help interpret the epitaxial relationship. A textured, or an out-of-plane oriented only growth will present a ring pattern at certain χ angles in the pole figure. A detailed example about the interpretation to the Au on Si pole figures can be found in Paper I.

1.3. ENERGY CONVERSION THROUGH THE PHOTOELECTRO CHEMICAL (PEC) PROCESS

Ever since the urgent demand for sustainable, inexhaustible energy sources was introduced back in 1970's, the research topic of solar energy acquisition through

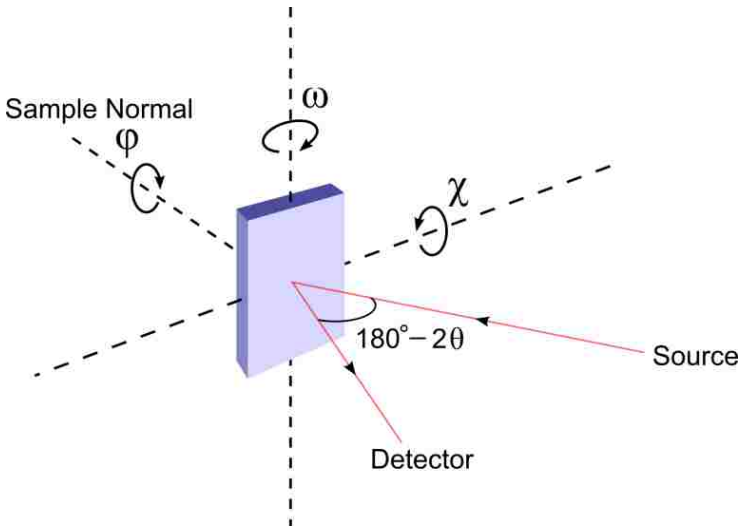

Figure 1.2. X-ray diffraction geometry showing θ, ω, φ, χ angles (image source: [25])

photoelectrochemical process has thrived for decades and is still receiving massive attention today.[66] Generally, the PEC energy conversion includes two basic categories: a photosynthetic cell stores energy by converting light to chemical energy – that is, a new chemical species (or multiple species) which possesses higher energy density is synthesized during this process. The most frequently investigated two examples of this category are PEC water splitting, sometimes called water photoelectrolysis, and PEC CO_2 reduction.[67] Another path is to convert light to electricity through PEC process without overall chemical change. The device that performs this path is usually called a PEC regenerative cell. Both approaches require not only a semiconductor that is capable of absorbing light of appropriate wavelengths and producing electron−hole pairs, but also a catalyst that accelerates the PEC reactions, because typically the semiconductor itself is usually passive or non-catalytic to most PEC reactions.

1.3.1. PEC Water Splitting and OER Catalysts. A general idea of taking advantage of solar energy besides photovoltaics and solar thermal is to have it split water, which covers 70% area of the earth, into environmentally friendly fuels – hydrogen and oxygen. The first PEC water splitting cell was carried out in 1972 by Honda and Fujishima using TiO_2 photoelectrodes.[68] After decades of investigation, a spectrum of semiconductor and catalyst materials for PEC water splitting has been well established.[69–71]

The chemical principle of water splitting is rather simple. The water molecules or protons get reduced at the cathode/photocathode and evolve hydrogen:

$$2H_2O + 2e^- \rightarrow H_2 + 2OH^- \quad (8)$$

or,

$$2H^+ + 2e^- \rightarrow H_2 \quad (9)$$

And the water molecules or hydroxide ions get oxidized at the anode/photoanode and evolve oxygen:

$$2H_2O - 4e^- \rightarrow O_2 + 4H^+ \quad (10)$$

or,

$$4OH^- - 4e^- \rightarrow O_2 + 2H_2O \quad (11)$$

However, it takes a standard cell voltage of 1.23 V to drive this process to take place, as the Gibbs free energy change of the overall reaction per water molecule is 237 kJ/mol. Thus, a semiconductor with the appropriate band gap and band edge positions must be chosen to meet the basic theoretical energetic requirements.[69] Furthermore, due to the large overpotential that occurs to the half reaction on the photoelectrodes, especially the anodic oxygen evolution reaction (OER), efficient catalysts applied to the electrodes are also important to the whole water splitting process.

Compared to the cathodic hydrogen evolution reaction (HER), OER is a kinetically slower half reaction and is a four-electron electrochemical process. Hence, extensive research and huge effort is devoted to improving the kinetics of the OER process, mostly finding more efficient catalysts. Conventional precious metal oxides catalysts such as IrO_2 and RuO_2 have been found to show the highest OER performances to date, and several approaches have been developed to efficiently produce these catalysts.[72–76] Nevertheless, the scarcity of these precious metal elements elevates the product price and limits the mass scale applications of these catalysts. Earth-abundant transition metal based OER catalysts, especially Mn, Fe, Co and Ni compounds provide an intriguing solution for this predicament. Cobalt oxide and oxyhydroxide for example, are two candidates that shows good OER catalytic properties, and can be easily fabricated through electrochemical deposition.[77] Co thin films can be deposited onto n-Si to form a metal-insulator-semiconductor (MIS) junction for efficient PEC water oxidation.[78] Recent research also pointed out that some selenides are capable to show remarkable OER catalytic performance such as binary and ternary Co, Fe and Ni selenide.[79–81]

1.3.2. PEC Regenerative Cell. Although higher solar energy conversion efficiency can be realized by multijunction (sometimes called multi-bandgap) semiconductor cells,[82] a study into single junction PEC regenerative cell can be important and helps provide understanding of the fundamentals of the interfacial kinetics and the physics behind the regenerative PEC process. Typically in a PEC regenerative cell in which only one kind of semiconductor is involved, the interfacial kinetics can be controlled mainly by two sources: the junction formed by the semiconductor/liquid contacts or the junction formed by the contact between semiconductor and the catalyst or surface coating. Under the former

situation, the semiconductor is immerged into a solution that contains a redox couple O/Re having a thermodynamic equilibrium potential of $E°_{(O/Re)}$. The redox couple can serve as acceptors and donors in this case. Electrons flow freely through the interface until equilibrium is reached and a semiconductor/liquid junction is established, as shown in Figure 1.3. The barrier height φ, which is generated by the band bending in the semiconductor, gives the sum of the theoretical maximum voltage that can be derived under illumination (φ_{fb}) and the built-in potential (which is constant). This brings a great benefit exclusively for PEC regenerative cell that the cell efficiency can be optimized by choosing appropriate redox couples which provide as large a difference between redox potential $E°_{(O/Re)}$ and the conduction band energy E_c (strictly speaking, the electron affinity) as possible.[69]

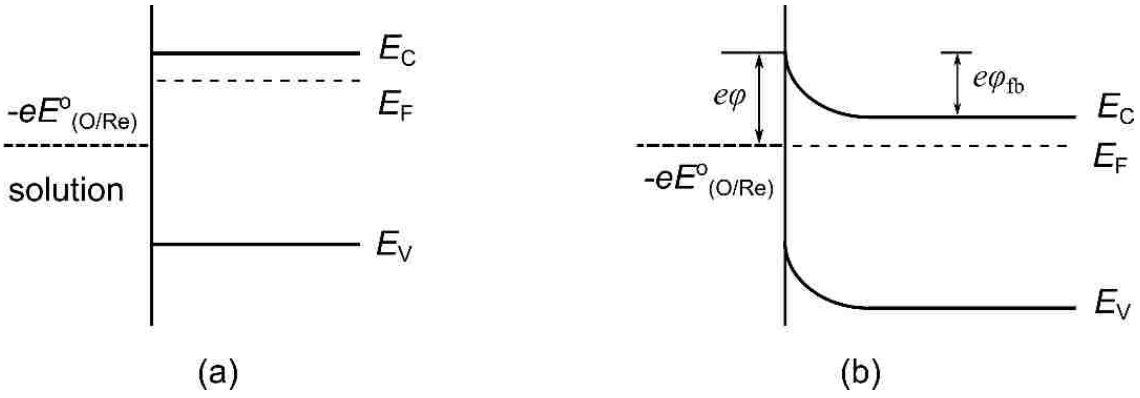

Figure 1.3. Energy diagrams of solution/n-type semiconductor contact (a) before and (b) after equilibrium

Limitations also apply to the PEC regenerative cells based on semiconductor/liquid contacts. In some occasion, the semiconductor surface is not capable to provide enough

catalytic effect for the redox reaction, which limits the overall charge transfer rate. Furthermore, some active semiconductor surfaces (e.g., Si) are not stable in the solution containing chemical redox couple, especially in aqueous solution. In such situation a catalytic layer deposited onto the semiconductor surfaces is used to improve the charge-transfer process and to prevent the semiconductor from being oxidized or corroded by the chemical species in the solution. A Schottky barrier could be introduced and serves as a PEC active junction if the catalyst is metallic. The formation process of Schottky contact, also known as metal-semiconductor contact, is similar to the semiconductor/solution contact mentioned above, as shown in Figure 1.4. When a high work function metal is brought in contact with a n-type semiconductor, charge (electrons) will flow from the semiconductor to the metal and thermal equilibrium is established to achieve a matched Fermi level (strictly speaking, to achieve an equal chemical potential of electrons on both sides at equilibrium). A band bending analogous to the solution situation is formed and a depletion region is created on the semiconductor side with a depletion width of W_D at equilibrium:

$$W_D = \sqrt{\frac{2\varepsilon_s}{eN_D}(\varphi_{fb} - \frac{kT}{e})} \tag{12}$$

where, ε_s is the permittivity of the semiconductor, e is the elementary charge and equals to 1.602×10^{-19} C, N_D is the carrier density, φ_{fb} is the flat band potential, k is the Boltzmann constant and T is the absolute temperature. The barrier height φ in an ideal Schottky contact is the difference between the metal work function φ_M and the electron affinity χ of the semiconductor.[83]

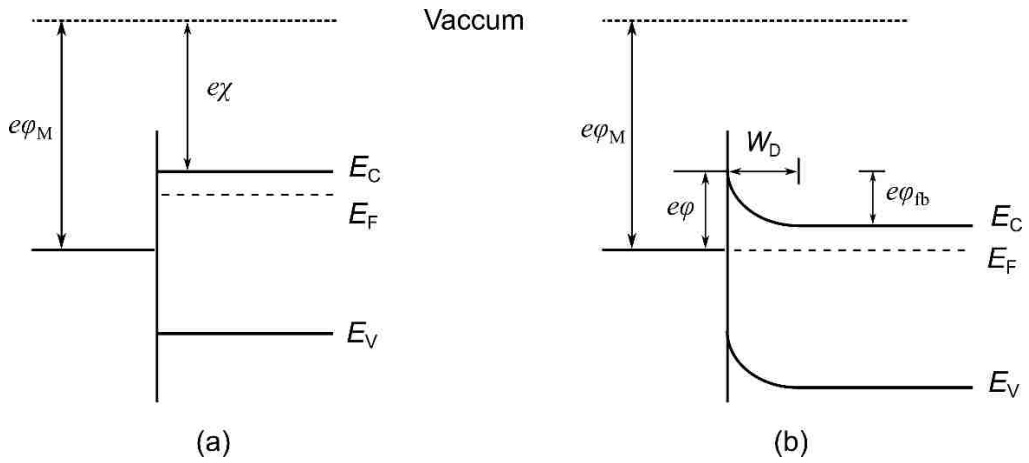

Figure 1.4. Energy diagrams of metal-semiconductor contact (a) before and (b) after equilibrium

The Schottky junction presents similar rectifying properties as a p-n junction. When a reverse bias is applied to the semiconductor, band bending further develops, causing a higher barrier height and an inhibited current flow. If a forward bias is applied to the semiconductor, the band bending in the semiconductor is reduced. The bias voltage required for the semiconductor bands to flatten is called the flat band voltage φ_{fb} as mentioned in Equation (12), sometimes referred as built-in voltage. Under a forward bias, the current flow obeys the diode equation:

$$J = J_s\left(\mathrm{e}^{eV/nkT} - 1\right) \tag{13}$$

where V is the voltage, n is the diode quality factor, J is the measured current density and J_s is the dark saturation current density. In this case, the barrier height can be determined directly from the dark saturation current:

$$\varphi = \frac{kT}{e}\ln\left(\frac{A^*T^2}{J_s}\right) \tag{14}$$

where A^* is the effective Richardson's constant of the semiconductor.

When a Schottky junction is under illumination, the electrons in the semiconductor are excited from the valence band to the conduction band, generating separated electrons and holes. In an open-circuit, the electrons and holes accumulate and a photovoltage is formed. When the device is connected to a closed circuit, photo-generated electrons in the depletion region will flow into the bulk of the semiconductor while holes flow to the junction interface, forming a photogenerated current I_{ph}. The current-voltage relationship under illumination can be described by Equation (15):

$$V = \frac{nkT}{e} \ln\left(\frac{J_{ph} + J_S - J}{J_S}\right) - R_S J \tag{15}$$

where V is the voltage, J_{ph} is the photogenerated current density, R_S is the series resistance of the circuit and J is the current density. It can be derived from the above equation that when the current (density) J equals 0, the solar device achieves its maximum voltage, usually called open circuit voltage V_{oc}, and when the voltage equals 0, the device reaches its maximum output current, called short circuit current (density) J_{sc}. It can also be derived that within the current density range from 0 to J_{sc}, a point with maximum power output can be acquired with a corresponding current density J_{mpp} and voltage V_{mpp}, the cell efficiency thus can be defined as following:

$$\text{efficiency} = \frac{J_{mpp} \times V_{mpp}}{P_{in}} \tag{16}$$

where P_{in} is the power input from the illumination. Note that the photogenerated current density J_{ph} is a function of the illumination light intensity, so the V_{oc} and J_{sc} of a certain cell will vary based on the illumination situation. By immersing this metal-semiconductor junction device into a solution containing redox couple, the photovoltage or

photogenerated current will drive the PEC reaction at the electrode surface. For a n-type semiconductor, the junction could serve as a photoanode where oxidation reaction occurs. Figure 1.5 shows a simplified PEC regenerative cell based on a Schottky junction photoanode. The reduced form of redox species receives holes generated by semiconductor under illumination and gets oxidized at the photoanode surface, and is then reduced back again at the cathode, receiving electrons. Thus, no net chemical change happens during the PEC process and electricity is generated. Sometimes, the PEC regenerative cell is designed as a flow cell to improve the mass transfer of the redox species, and the overall efficiency can also be enhanced.[84]

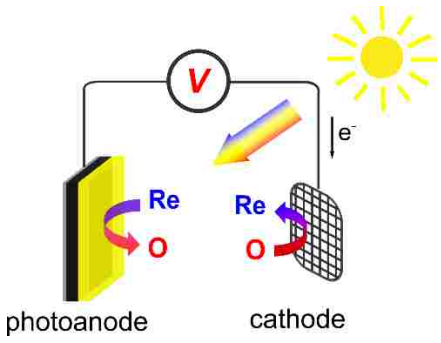

Figure 1.5. A simplified PEC regenerative cell based on a metal/n-type semiconductor junction

The above discussion, of course, is for ideal metal-semiconductor interface condition where the barrier height is determined only by the metal work function. In fact, the semiconductor interfacial behavior is almost always influenced also by the interface states. The interface trap density of the semiconductor, which generally comes from grain boundaries, defects and different chemical compounds formed at the surface of the material, plays an important role in the barrier height. When the trap density is large

enough, the barrier height would be determined mainly by the surface properties of the semiconductor. Therefore, a metal-insulator-semiconductor (MIS) junction device is applied in some situations to improve the interface properties and to enhance the barrier height.[78] The thin insulator layer, which is usually made of SiO_x, is thin enough to let the current tunnel through. The insulator layer minimizes the surface states so that the barrier height is determined more by the work function of the metal. In Paper I, the PEC regenerative cell using Au films deposited on n-Si as the photoanode and $Fe^{2+/3+}$ ions as the redox couple presents a maximum photocurrent of 11.9 $mA \cdot cm^{-2}$ with AM 1.5 light illumination of 100 $mW \cdot cm^{-2}$ intensity. The barrier height of the Au/Si junction was determined from 0.81 to 0.73 eV as the Au film thickness increased from 10% coverage to 11 nm. An interesting phenomenon also occurred when the photoanode underwent a stability test: the barrier height increased during the long-term chronoamperometry at short circuit status. Considering that the Si can be oxidized by the solution through the pinholes distributed in the Au film, these facts indicate that the photoanode probably experienced a transition from a Schottky junction to a MIS junction over time during the PEC process.

1.4. FLEXIBLE ELECTRONIC MATERIALS

It is usually assumed that "flexible electronics" is a rather recent concept. However, the early idea of making electronics, especially solar cells flexible was brought up in the 1960's, where flexible solar cell arrays were considered to bring advances to the design of satellite solar cells in the U. S. space program.[85] The principle of fabricating this kind of flexible electronics took advantages of a very simple physical phenomenon: Any material that is thin enough can be flexible, even for hard bulk materials (such as Si). Over time,

this concept has been developed and has evolved into many categories that are closely related to human daily life, such as flexible displays, wearable solar cells, flexible batteries and sensors.[86–91] Generally, a flexible electronic device is built up with four components: a substrate, backplane electronics, a frontplane, and encapsulation. All four components need to be flexible to a certain extent.[92] Due to different functionalities required for different components, all varieties of flexible materials with different physical and chemical properties have been developed and studied, including metal oxide films and thin glass,[93,94] nanowire arrays or meshes,[95–98] polymers[99–102] and metal thin films/foils.[103–107] In this introduction, the main focus will be on ultrathin metal foils for flexible materials.

Due to high electrical conductivity, outstanding optical property and high flexibility, ultrathin metal foils have been investigated as flexible electronic materials for a long time. In some cases, metal foils serve only as substrates for flexible electronic devices such as organic light emission displays (OLED). The most preferred metal for this application is stainless steel, as it can tolerate high process temperature, is dimensionally stable, presents a barrier against moisture and oxygen, can serve as a heat sink, and can provide electromagnetic shielding.[92,108] Recent research has also considered metal foils ideal alternatives of the conductive indium-tin oxide (ITO) film electrode, which can serve as a positive contact in an OLED device,[109] due to a rising cost of indium, brittleness of ITO, insufficient conductance for large-area devices, and the diffusion of indium atoms in the ITO electrode into the organic active layer, which causes degradation of the device performance.[103,104,106] In this case, coinage metals (Cu, Ag, and Au) are more often adopted. Typically, these metal foils are fabricated by sputtering, which brings some drawbacks such as island-like deposits controlled by Volmer-Weber growth mechanism.

The roughness caused by this process can be minimized by introducing heteroatoms and conducting co-deposition or by forming a seed layer.[106,110] However, these films are typically polycrystalline, and the high-angle grain boundaries in polycrystalline structures will influence the performance of the electronic devices further deposited onto the metal foils (e.g., OLED) as mentioned in the epitaxy section.

In Paper II, a novel approach is introduced to produce electrodeposited single-crystal like Au foils through a photooxidation lift-off process. This technique is capable of producing highly flexible and transparent wafer-size Au foils. It involves the epitaxial electrodeposition of Au on Si which follows the same procedure as introduced in section 1.1, followed by a PEC oxidation of Si in dilute H_2SO_4 solution. The Au foils can be peeled off from the Si substrate after photooxidation and can maintain the in-plane and out-of-plane order of the Au epitaxial films. A minimum thickness of 7 nm can be acquired for the Au foils with a transmittance up to 85%, and a bending test determines that the sheet resistance of the Au foils increases minimally after 4000 bending cycles. A flexed and light emitting OLED spin-coated on the Au foil demonstrates the flexibility and the transmittance of Au foils. More importantly, a Cu_2O deposited onto the Au foil exhibited a diode quality factor of 1.6 compared with a value of 3.1 for polycrystalline deposits, showing a great advantage of the epitaxy of those Au foils fabricated through this approach.

PAPER

I. PHOTOELECTROCHEMISTRY OF ULTRATHIN, SEMITRANSPARENT, AND CATALYTIC GOLD FILMS ELECTRODEPOSITED EPITAXIALLY ONTO N-SILICON(111)

*Qingzhi Chen and Jay A. Switzer**

Missouri University of Science and Technology, Department of Chemistry and Graduate Center for Materials Research, Rolla, MO 65409-1170, USA

ABSTRACT

Films An ultrathin, epitaxial Au layer was electrochemically deposited on n-Si(111) to form a Schottky junction that was used as the photoanode in a regenerative photoelectrochemical cell. The Au serves as a semitransparent contact that both stabilizes the n-Si against photo-passivation and catalyzes the oxidation of Fe^{2+} to Fe^{3+}. In this cell, Fe^{2+} was oxidized at the n-Si(111)/Au(111) photoanode, and Fe^{3+} was reduced at the Au cathode, leading to conversion of solar energy into electrical energy with no net chemical reaction. The photocurrent was limited to 11.9 $mA \cdot cm^{-2}$ due to absorption of light by the $Fe^{2+/3+}$ redox couple. When a transparent solution of sulfite ion was oxidized at the photoanode, photocurrent densities as high as 28.5 $mA \cdot cm^{-2}$ were observed with AM 1.5 light of 100 $mW \cdot cm^{-2}$ intensity. One goal of the work was to determine the effect of the Au layer on the interfacial energetics as a function of the Au coverage. There was a decrease in the barrier height from 0.81 to 0.73 eV as the gold coverage was increased from

island growth with 10% coverage to a dense Au film with a thickness of 11 nm. In all cases, the bandbending in the n-Si was induced by the n-Si/Au Schottky junction instead of the energetic mismatch between the Fermi level of the n-Si and the redox couple. The dense Au film gave the greatest stability. Although the photocurrent of the n-Si/Au photoanode with 10.2% island coverage dropped nearly to zero within 2 hours, the photocurrent of the photoanode with a dense 11 nm thick Au film only decreased to 92% of its initial value after irradiation at open circuit with AM 1.5 light for 16 hrs. A 2.1 nm thick layer of SiO_x formed between the Au film and the n-Si. With further irradiation the fill factor decreased due to the increase of series resistance as the SiO_x layer thickness exceeded tunneling dimensions.

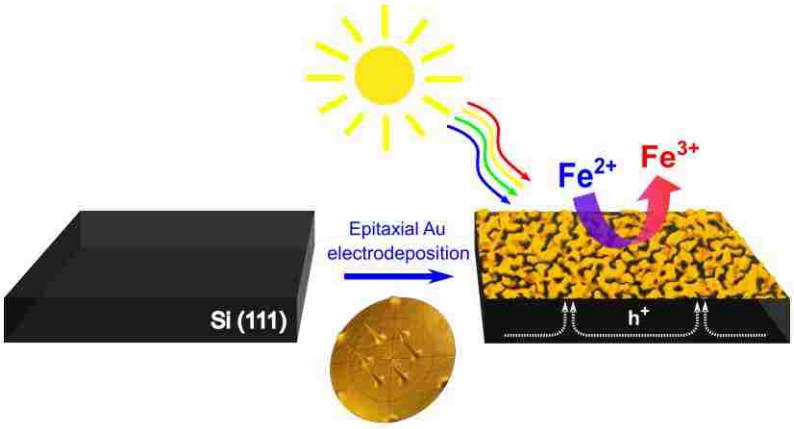

Keywords: electrodeposition, epitaxy, thin films, gold, photoelectrochemistry, silicon, catalytic.

1. INTRODUCTION

The photoelectrochemical conversion of solar energy into fuels or electricity requires a semiconductor to absorb light and generate electron-hole pairs, and a catalyst to enhance the kinetics of electron transfer between the semiconductor and solution.[1,2] The catalyst can serve both to improve charge separation by passivating surface states and to improve the charge transfer process across the semiconductor-solution interface.[3-8] In photoelectrochemical cells containing reactive semiconductors such as Si, the catalyst can also serve to protect the semiconductor from passivation caused by the formation of a thick SiO_x interfacial layer. The catalyst can either be directly deposited onto the semiconductor,[9-11] or onto a thin insulator of tunneling dimensions to produce a metal-insulator-semiconductor (MIS) photoelectrode.[12-14] Here, we explore the use of thin epitaxial gold films that are electrodeposited directly on n-Si(111) as a semitransparent catalyst to produce a photoanode in a regenerative photoelectrochemical cell using Fe^{2+}/Fe^{3+} as the redox couple. We use the method developed by Allongue and co-workers to electrodeposit the epitaxial Au.[15] Although the epitaxy will not necessarily enhance the performance of the photoanode, the deposition method produces ultrathin, dense layers of Au that can be transparent to light. We have previously used this method to produce large area Au films which serve as a proxy for Au single crystals[16] and we have shown that the method can also produce free-standing single-crystal Au foils for flexible electronics.[17]

We also determine the effect of the catalyst on the band-bending, and photovoltage, of the photoanode. That is, we determine whether the band-bending in the semiconductor depletion region is produced by the mismatch between the Fermi level of the

semiconductor and the solution potential, or by the formation of a metal/semiconductor Schottky barrier. In addition to determining the effect of the Au coverage on the interfacial energetics, we determine its effect on the stability of the n-Si in the aqueous solution. The Fe^{3+}/Fe^{2+} potential is positive enough (+0.77 V vs. NHE) that the Si oxidizes easily in such an electrochemical environment (the potential for the SiO_2/Si couple is -0.909 V vs. NHE).[18] We further show that the photocurrent can be markedly improved by reducing the light absorption using a colorless SO_3^{2-}/SO_4^{2-} redox couple.

2. RESULT AND DISCUSSION

The Au deposits initially as islands on the n-Si(111), which then grow two-dimensionally to produce a dense film as additional Au is deposited. The morphology of the Au deposits as a function of deposition time is shown by scanning electron microscopy (SEM) in Figure 1. The SEM image of the Au deposited for 10 s and 1 min on Si shows uniform nucleation of Au as nanometer-scale islands. The coverage after 10 s was 10.2% (measured by image analysis), and the coverage after 1 min was 39.2%. After 5 min the deposit develops a “worm-like” fractal pattern, and after 10 minutes the Au has coalesced into a dense film with some pinholes remaining. The thickness of the films deposited for 5 and 10 minutes can be determined by X-ray diffraction (XRD) from Laue oscillations.[16] The thickness of a 5 min deposit of Au is 7 nm and the thickness of a 10 min deposit is 11 nm, as shown in our previous work.[16]

X-ray diffraction was also conducted to measure the out-of-plane and in-plane orientation of the Au films relative to the Si(111) substrate. As shown in Figure S1

(Supporting Information), the symmetric XRD 2-Theta scan shows that the Au on Si(111) grows with a [111] out-of-plane orientation. Si(220) and Au(220) pole figures were run to

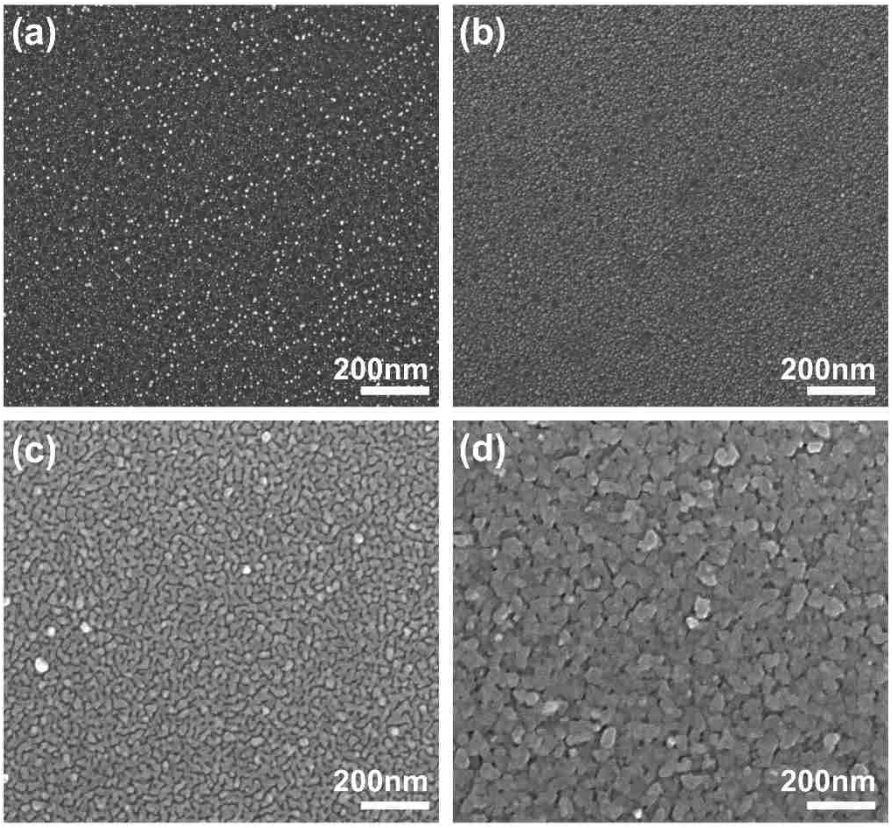

Figure 6. SEM plan-view images of Au thin films of different thicknesses on n-Si(111). (a) 10 s, (b) 1 min, (c) 5 min and (d) 10 min. The coverage of 10 s Au on Si is 10.2% and 1 min Au on Si is 39.2%

determine the in-plane orientation of the Au relative to the Si. The Si (220) pole figure in Fig. 2(a) shows three spots separated 120º azimuthally at a tilt angle (ψ) of 35.5º, which agrees with the calculated stereographic projection for single-crystal Si(111) shown in Figure S2 in Supporting Information. The Au(220) pole figures of 10 s and 1 min Au on Si do not show spots in the pole figures [Figure 2 (b) and (c)] due to the low Au coverage.

The pole figures of 5 min and 10 min Au on Si both show six spots at ψ of 35.5º due to parallel and antiparallel domains of Au. Epitaxial relationships consistent with these pole figures are Si(111)[10$\bar{1}$]||Au(111)[10$\bar{1}$] and Si(111)[10$\bar{1}$]||Au(111)[$\bar{1}$01].

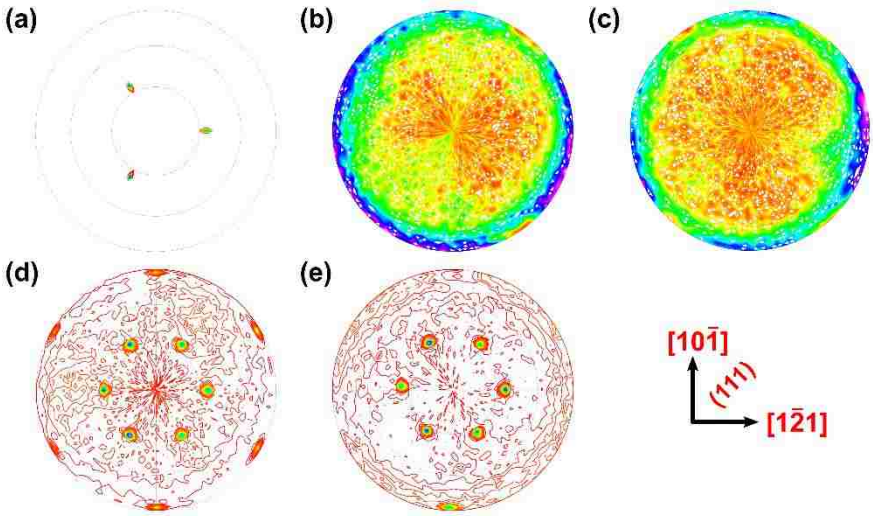

Figure 7. Determination of the in-plane orientation of the Au(111) relative to the Si(111) substrate. XRD pole figures of Si(111) substrate (a) and Au(111) thin films of different thicknesses (b-e) showing in-plane orientations. The Au deposition times are (b) 10s, (c) 1 min, (d) 5 min and (e) 10 min

In order to harvest as much light as possible, the catalyst layer must be thin enough to not appreciably attenuate the incident light. The absolute specular reflectance spectra of the Si substrate and bulk Au are shown in Fig. 3a, and the spectra of the Au films on Si are shown in Fig. 3b. The reflectance of bare Si is 30.7% at 1600 nm and increases to 46% at 400 nm, as expected based on the n and k values for Si. The reflectance of 10 s, 1 min, 5 min and 10 min Au on Si increases successively to 31.2%, 31.7%, 36.7% and 44.7% at 1600 nm. As seen in the spectra, the 10 s and 1 min Au on Si shows similar features as bare Si, while more metal-like gold features begin to emerge on the 10 min Au on Si at larger

wavelengths. Hence, there is minimal absorption or reflection of light by the thinner Au samples, but up to 10-20% of the light is reflected for the thicker Au films. There is also

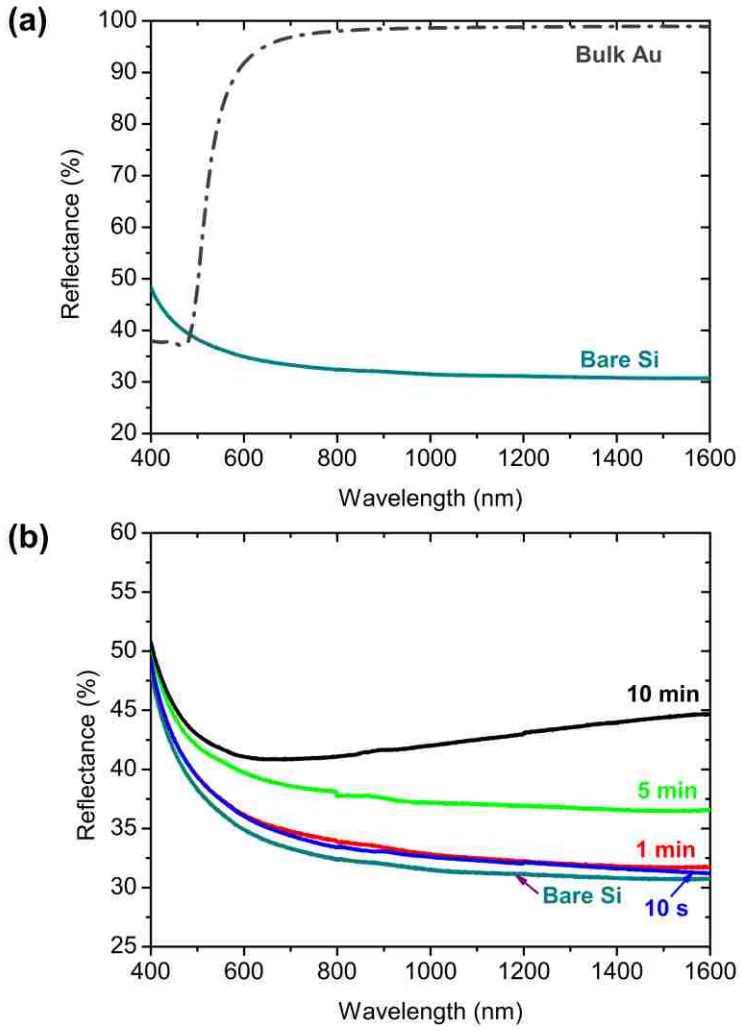

Figure 8. Absolute specular reflectance spectra of the Au films. (a) bare Si (measured) and bulk Au (calculated from n and k), (b) gold thin films on n-Si(111) for different gold deposition times.

no evidence of light trapping by surface plasmons by the ultrathin Au layers. This agrees with earlier work by Maaroof et al. in which nanoporous gold films produced by sputtering did not show strong surface plasmon absorption.[19]

Gold is known to be catalytic for a wide range of redox reactions, including the $Fe^{2+/3+}$ couple. The exchange current density for this couple on Au was reported to be 18 $A \cdot cm^{-2}$. [20] The catalytic nature of the Au on Si is shown by cyclic voltammetry (CV) in Figure 4 by comparing the CVs of the $Fe^{2+/3+}$ couple on Au on glass, Au on degenerate Si, and bare degenerate Si. Degenerate Si was used to avoid the rectifying nature of n-Si/Au Schottky junction which is blocking to anodic current. The bare Si electrode exhibits negligible current throughout the entire potential range from 0 to 0.8 V vs. Ag/AgCl, which indicates that it is catalytically inert for the $Fe^{2+/3+}$ reaction. The Au on Si shows a quasi-reversible CV curve with a peak separation of 133 mV at a scan rate of 20 mVs^{-1}. It has about the same peak currents as a Au on glass electrode, which gives a peak separation of

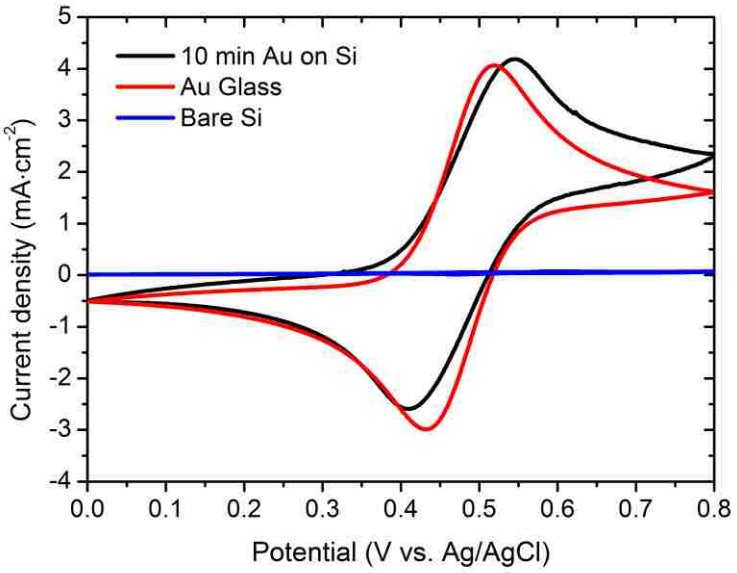

Figure 9. Enhancing the catalytic activity of the Si surface. Cyclic voltammetry measurements of 10 min deposited Au thin film on degenerate Si (black curve), Au coated glass electrode (red curve), and bare degenerate Si electrode (blue curve) in 50 mM $FeSO_4$ solution. The peak separation of the Au on glass electrode is 83 mV and that of the 10 min Au on Si is 133 mV, showing that the Au deposited on Si has similar catalytic activity for the $Fe^{2+/3+}$ redox reaction as a Au electrode. Note that the bare Si is catalytically inert for the reaction. The scan rate was 20 mVs^{-1}.

83 mV at the same scan rate. Hence, the redox reaction is chemically reversible and electrochemically quasi-reversible on the Si/Au electrode.

The n-Si(111)/Au(111) photoanodes were tested as a function of Au coverage in a regenerative photoelectrochemical cell using a solution of 1 M Fe^{2+} and 0.1 M Fe^{3+} with a Au counter electrode. The photocurrent density vs. photovoltage curves for the photoanodes are shown in Figure 5 using an AM 1.5 light source with an irradiance of 100 $mW \cdot cm^{-2}$ (1 sun). The highest short-circuit current density of 11.9 $mA \cdot cm^{-2}$ and open-circuit photovoltage of 0.34 V are observed for the photoanode produced by depositing Au on Si for 10 s. At longer deposition times of 1 min, 5 min and 10 min, the open-circuit photovoltage decreases to 0.33, 0.26, and 0.25 V. The 10 min Au on Si photoanode also gives the lowest photocurrent density of 8.9 $mA \cdot cm^{-2}$, and fill factor of 0.40, with an efficiency of 0.90%. The photovoltaic parameters for all of the cells are presented in Table S1 (Supporting Information). Notice in Figure 5 that there is a decrease in photovoltage for the thicker Au films that have coalesced. This is consistent with a decrease in the barrier height in the n-Si depletion region for those photoanodes, as shown below.

The photocurrents and efficiencies for the n-Si(111)/Au(111) photoanode are not very competitive compared to other photoelectrochemical cells in the literature that are based on Si. [21,22] The main reason for this lower performance is that the $Fe^{2+/3+}$ solution is highly colored, leading to a significant attenuation of the incident light. The path length in the cell is 1 cm, so the light intensity has been attenuated by about 53% before it arrives at the photoanode (see Supporting Information and Figs. S3 and S4 for details). This problem can be circumvented by using a less absorbing redox couple (see results with SO_3^{2-} below), or by designing a short pathlength flow cell.

Although the photoelectrochemical cell using the $Fe^{2+/3+}$ redox couple does not give high performance due to significant light absorption, it does allow us to probe the interfacial energetics in the photoanode. That is, we can determine the effect of the Au

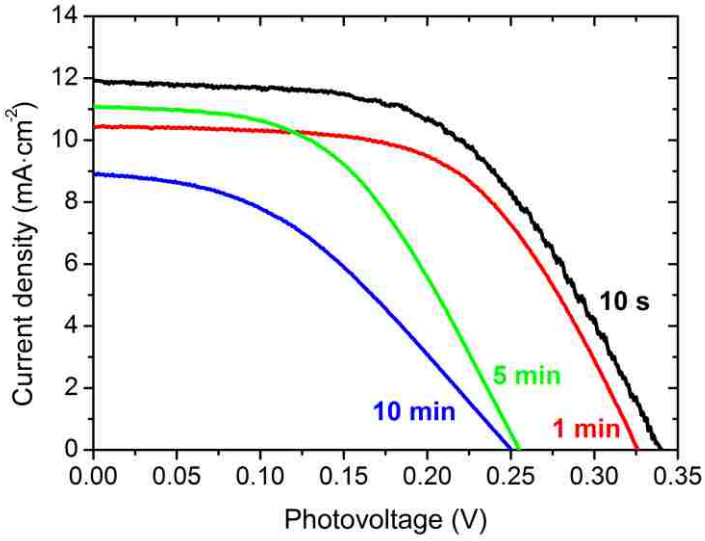

Figure 10. Photoelectrochemical performance of n-Si/Au photoanodes in a regenerative cell using the $Fe^{2+/3+}$ redox couple. Photocurrent density versus photovoltage of Au thin films on n-Si of different Au thicknesses in the $Fe^{2+/3+}$ solution under 1 sun illumination

catalyst on the band bending in the n-Si. The barrier heights (φ) and diode quality factors (n) were determined dynamically as a function of Au coverage by measuring the photocurrent-photovoltage response curves at a series of different light intensities and applying Equations (1) and (2),[21]

$$\varphi = \frac{kT}{e} \ln\left(\frac{A^{*}T^{2}}{J_{S}}\right) \tag{1}$$

$$V_{OC} \approx \frac{nkT}{e} \ln\left(\frac{J_{L}}{J_{S}}\right) \tag{2}$$

where k is Boltzmann's constant (1.38×10^{-23} J·K^{-1}), T is the temperature (294 K), e is the charge of an electron (1.60×10^{-19} C), A^* is the effective Richardson's constant (120 A·cm^{-2}K^{-2} for n type Si),[23] J_S is the dark saturation current density(A·cm^{-2}), V_{OC} is the open-circuit voltage, n is the diode quality factor (n=1 for an ideal diode), and J_L is the limiting current density (A·cm^{-2}). Figure 6 (a) shows a typical set of photocurrent-photovoltage response curves at a series of light intensities for a photoanode produced by depositing Au on n-Si for 5 min. The J_S and n for each photoanode was determined from plots of ln(J_{SC}) vs. V_{OC}, as shown in Figs. 6(b-e). The barrier heights of the photoanodes with 10 s, 1 min, 5 min and 10 min Au on Si are 0.81, 0.82, 0.75, and 0.73 eV, respectively (see Supporting Information, Table S2). The measured barrier heights are similar to the recognized barrier height of a n-Si/Au Schottky junction (0.83 eV),[23] which suggests that the photovoltage of the photoanode is dominated by the n-Si/Au junction rather than the n-Si/solution junction. The diode quality factor of the photoanodes with 10 s, 1 min, 5 min and 10 min Au on n-Si are 1.16, 1.08, 1.11, and 1.24, respectively (see Supporting Information, Table S2). These values are close to the ideal value of n=1, showing that electron-hole recombination is not dominant in these photoanodes.[23]

We also measured the barrier height of a solid-state diode produced by depositing Au for 5 min on n-Si. The diode curve is shown in Figure 7. The dark saturation current density measured at forward bias for this diode is 2.88 x 10^{-7} Acm^{-2}, which corresponds to a barrier height of 0.79 eV. The diode quality factor is 1.17. The barrier height for the solid-state diode is close to that measured in solution, again consistent with our assumption that the barrier heights in our photoanodes are dominated by the n-Si/Au junction rather than the n-Si/solution junction. We were not able to produce solid-state diodes with low

coverages of Au to see if the barrier height varies with coverage because of shorting that occurs when making front contacts to the incontinuous films.

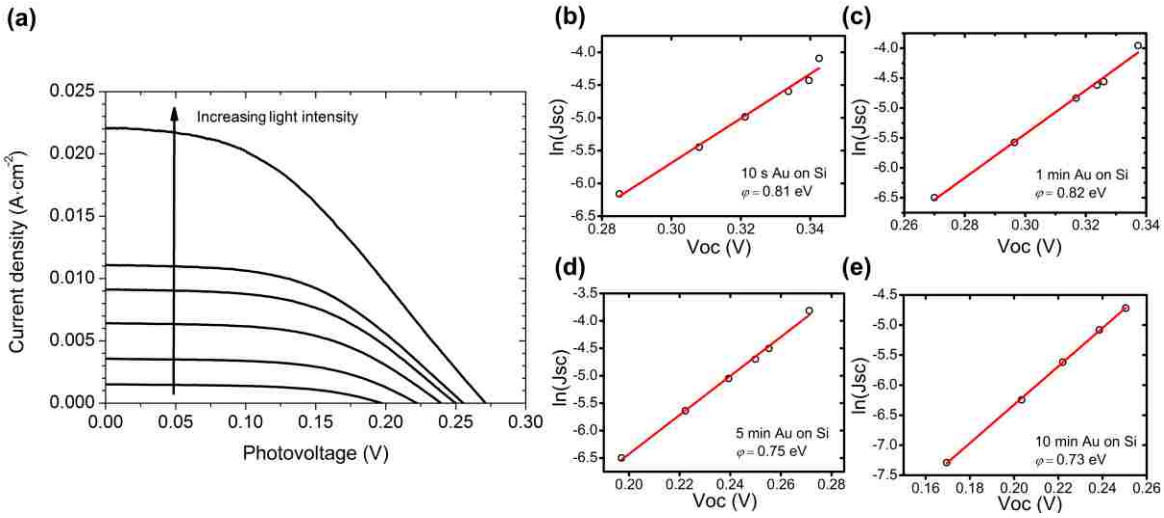

Figure 11. Measurement of the barrier height for n-Si photoanodes in a photoelectron-chemical cell with the $Fe^{2+/3+}$ as a function of the Au thickness. (a) Photocurrent curves of 5 min Au on Si in $Fe^{2+/3+}$ solution at different light intensities. Plots of $\ln(J_{SC})$ vs. V_{OC} of (b) 10 s, (c) 1 min, (d) 5 min, (e) 10 min Au on n-Si, with the measured barrier heights of 0.81, 0.82, 0.75, and 0.73 eV. The diode quality factors are 1.16, 1.08, 1.11, and 1.24, respectively

The fact that barrier heights for the junctions with low coverage of Au are higher than those with coalesced films in the photoelectrochemical cell is consistent with previous work that showed that inhomogeneous Schottky barriers can give a larger barrier height than Schottky barriers produced with continuous metal films.[21,24-26] It is also possible that for the low coverage films a tunnel junction of SiO_x rapidly forms under the Au islands to produce a metal-insulator-semiconductor (MIS) junction with decreased surface states and

increased barrier heights.[27] Although we cannot completely rule out the possibility that the solution potential has an effect on the barrier height for the low coverage deposits, earlier work by other researchers suggests that the spacing between islands in our low coverage

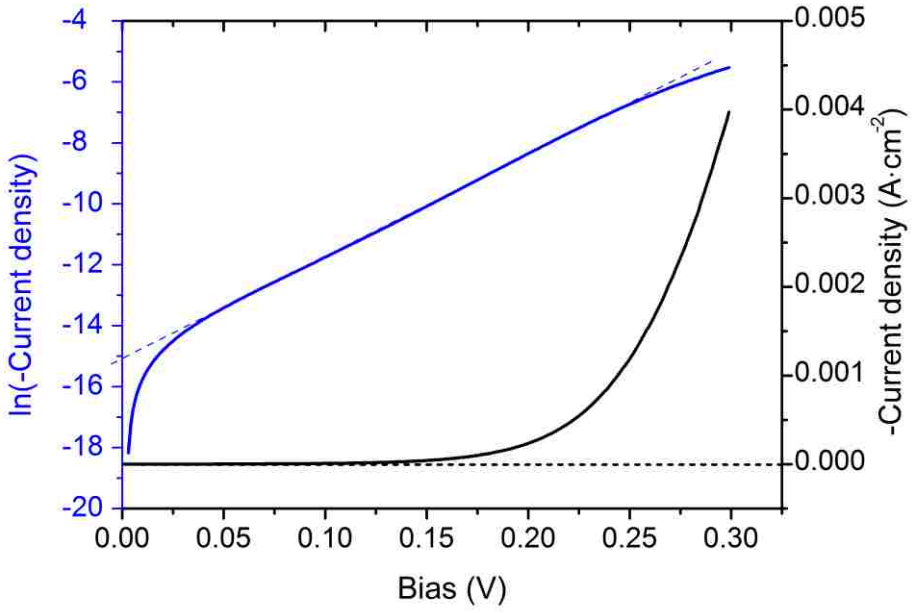

Figure 12. Determination of the barrier height of a solid state Schottky diode produced by electrodepositing epitaxial Au for 5 min on n-Si(111). The black curve is the current density versus forward bias and the blue curve is the natural log of the current density versus forward bias. The y intercept of the blue curve gives a dark saturation current of 2.88×10^{-7} Acm^{-2}, which corresponds to a barrier height of 0.79 eV. The slope gives a diode quality factor of 1.17

deposits may be small enough that the solution does not have an effect on the bandbending in the n-Si.[18,19] By contrast, Nakato et al. observed solution-dependent-photovoltages as high as 0.685 V for Pt nanoislands on n-Si if the spacing between the Pt islands was large enough.[18]

One goal of this work was to determine the ability of Au layer to prevent the Si surface from being passivated by SiO_x in the aqueous environment. The stability test of the

cell was measured by setting the potential at $E = 0$ V vs. $E^0(Fe^{2+/3+})$, where the cell reaches short-circuit current, and recording the anodic current density as a function of time at a light intensity equivalent to 1 sun. Figure 8 (a) shows the photocurrent of 10 s, 1 min, 5 min and 10 min Au on n-Si vs. time for irradiations up to 16 hours. The photocurrent for 10 s Au on n-Si dropped to nearly zero within two hours, which shows that the Au deposited for 10 s is not thick enough to protect the silicon from being oxidized. The photocurrents of 1 min, 5 min and 10 min Au on n-Si remained relatively stable for 16 hours, and the current after 16 hours (compared to the initial current) for each of the above is 86.4%, 91.4% and 92.2% respectively. Figure 8(b) shows the photocurrent- photovoltage relations of a 10 min Au on n-Si photoanode before the stability test and after 18 hours, 40 hours and 62 hours of irradiation at short circuit. As shown in the plot, the short-circuit current and fill factor keep decreasing while the open-circuit photovoltage increases slightly (see the zoom-in details of open-circuit photovoltage in Fig. S5 of Supporting Information). This is an indication that the dark saturation current density J_S decreased and the barrier height increased after time. The decrease in fill factor is due to an increase in the series resistance (R_S). The series resistance was calculated by the method of Araujo et al. based on the single-diode model (see Eq. 3 and Figs. S6 and S7 of Supporting Information for more details). The initial series resistance was 11.3 $\Omega \cdot cm^2$, but it increased to 12.7 $\Omega \cdot cm^2$ after 18 hours, 18.6 $\Omega \cdot cm^2$ after 40 hours, and 35.2 $\Omega \cdot cm^2$ after 62 hours. We attribute the increase in series resistance to an increase in thickness of SiO_x that forms between the n-Si(111) and the Au(111). As the SiO_x thickness increases beyond tunneling dimensions (about 2 nm), the series resistance should increase.

The SiO_x layer between the n-Si and Au was directly observed by HRTEM. Figure 9(a) is a TEM cross-sectional image of the as-deposited Au-Si interface. The lattice fringes

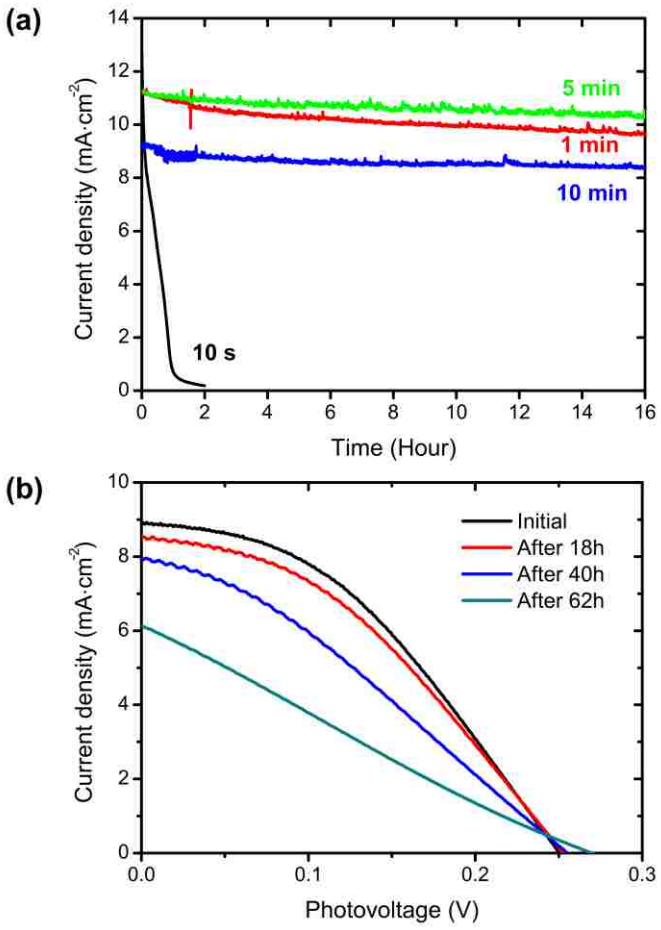

Figure 13. The stability of Au on n-Si(111) of different thicknesses in the $Fe^{2+/3+}$ solution. (a) chronoamperometry curves of Au on Si of different thickness in the $FeSO_4/Fe_2(SO_4)_3$ solution at fixed potential E = 0 V vs. $Fe^{2+/3+}$. (b) The initial photocurrent-photovoltage response for 10 min Au on n-Si(111), and the response after the 18, 40, and 62 hour stability tests

suggest the epitaxial growth of Au on Si with a [111] orientation, and no SiO_x layer is found between the Au and Si. Figure 9(b) shows a TEM image of the 10 min Au on Si after 16 hours of irradiation at short circuit in the $Fe^{2+/3+}$ solution. An amorphous SiO_x layer of

about 2.1 nm is observed between the Au and Si, while the Au maintains the [111] orientation. The lateral undergrowth of SiO_x is assumed to occur because of the pinholes in the film.[17] The 2.1 nm SiO_x layer is thin enough to allow quantum mechanical tunneling. As the SiO_x thickness exceeds this value, the series resistance of the photoanode should increase, as discussed above.[23,27]

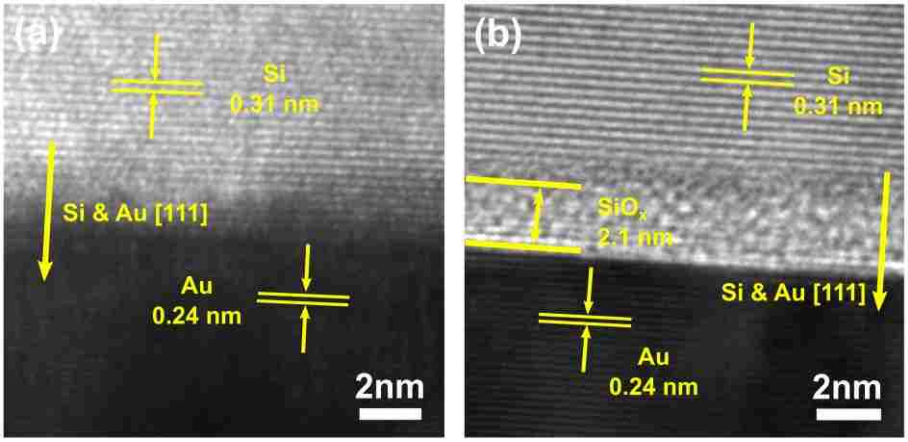

Figure 14. Evidence for lateral undergrowth of an SiO_x layer after irradiation. (a) HRTEM cross-section image of as-deposited Si(111)/Au(111) interface. (b) HRTEM cross-section image of 10 min Au on n-Si after 16 hours of stability test in $Fe^{2+/3+}$ showing a 2.1 nm thick SiO_x layer between the Au(111) and n-Si(111)

It is constructive to discuss at this point how the efficiency could be improved for the n-Si(111)/Au(111) photoanode. One possibility would be to deposit the Au onto a buried n-Si/p^{++}-Si junction. This would raise the photovoltage from the 0.3-0.4 V range observed for the n-Si/Au Schottky junction up to the 0.60-0.65 V range that is observed for n/p^+ junctions.[28] Another possibility would be to increase the photocurrent by addressing the absorption of light by the redox couple. As shown above, the absorption of incident

light by the solution causes more than half of the light to be lost before it reaches the photoanode. One approach would be to improve the cell design to minimize the solution path length, such as using a flow cell with an ultrathin pathlength. Another approach would be to use a transparent redox couple. We tested this idea by using the SO_3^{2-}/SO_4^{2-} redox couple. A phosphate buffered 1 M sodium sulfite solution was used to conduct this experiment. Figure 10 (a) shows the LSV scans of the 10 s, 1 min, 5 min and 10 min Au deposited on n-Si in the sulfite solution under 1 sun illumination. The 1 min, 5 min and 10 min Au on n-Si show saturation photocurrents of 28.5, 27.2, and 21.8 $mA \cdot cm^{-2}$ respectively. These values are comparable to the 26.6 $mA \cdot cm^{-2}$ photocurrent density that is observed with AM 1.5 radiation for a solid-state p-n junction silicon solar cell without an antireflection coating.[29] This experiment also sheds additional light on the mechanism of band-bending in the photoanode. Figure 10 (b) shows the photocurrent-photovoltage relations of Au on Si samples derived by subtracting the LSV curves of a Au on glass electrode from that of the Au on n-Si electrodes. The symbols are the measured data and the curves are fitted using the diode-equation (see Eq. 3) using the barrier height and diode quality factor data measured from the $Fe^{2+/3+}$ solution. Although the $Fe^{2+/3+}$ and SO_3^{2-}/SO_4^{2-} redox couples have very different standard reduction potentials (0.77 V compared with 0.17 V vs. NHE) the fitted curves using the barrier heights from the $Fe^{2+/3+}$ fit the experimental data for the SO_3^{2-}/SO_4^{2-} well, again suggesting that the Au layer and not the solution potential controls the bandbending in the n-Si.

$$V = \frac{nkT}{e} \ln\left(\frac{J_{ph} + J_S - J}{J_S}\right) - R_S J \tag{3}$$

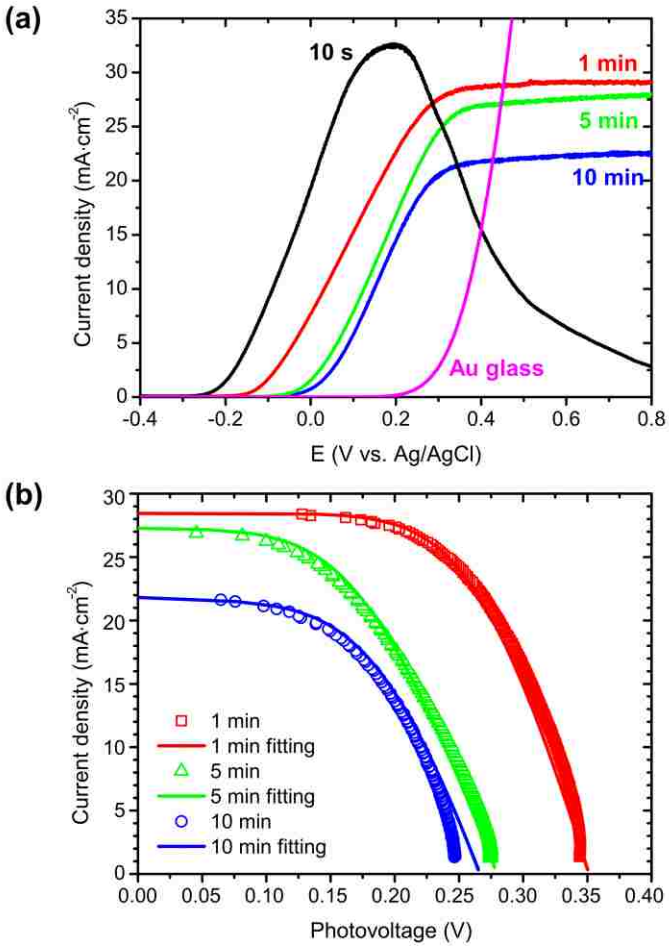

Figure 15. Photoelectrochemistry of the n-Si(111)/Au(111) photoanodes with different thicknesses of Au in the sulfite solution. (a) Linear sweep voltammograms (LSV) of the Au on n-Si electrodes in buffered 1 M Na_2SO_3 solution under 1 sun illumination compared with a Au-coated glass electrode in the same solution. Note that the photoanode with 10 min. of Au is not stable in the solution. (b) Photocurrent-photovoltage relationships of Au thin films on Si electrodes in Na_2SO_3 solution derived from LSV curves by subtracting the LSV curves of Au on Si from that of Au-coated glass electrode. The smooth curves were fitted with Eq. 3 using the barrier dark saturation current and diode quality factors determined in Fig. 6 in the Fe^{2+}/Fe^{3+} solution.

3. CONCLUSIONS

Epitaxial, ultrathin Au layers were deposited on n-type Si to form a Schottky junction. It was used as a photoanode to build a photoelectrochemical regenerative cell

with the $Fe^{2+/3+}$ redox couple. The ultrathin Au layer protects the n-Si from photopassivation. After a 16 hr. irradiation at short circuit, a 2.1 nm thick layer of SiO_x forms between the n-Si and Au. This SiO_x layer is thin enough to allow quantum-mechanical tunneling. Although the Au is semitransparent, the solution is highly absorbing. Because of the high absorption of light by the redox couple, the photocurrents were limited to 11.9 $mA \cdot cm^{-2}$. When the transparent SO_3^{2-}/SO_4^{2-} redox couple was used with the same photoanode, photocurrents as high as 28.5 $mA \cdot cm^{-2}$ were observed with AM 1.5 light with an irradiance of 100 $mW \cdot cm^{-2}$. In addition to being a good redox catalyst and semitransparent to light, the ultrathin gold layers serve to induce bandbending in the n-Si. The barrier height in the n-Si is determined by the n-Si/Au interface rather than the n-Si/solution interface. The barrier height was a function of Au coverage. It decreased from 0.81 to 0.73 eV as the gold coverage was increased from island growth with 10% coverage to a dense Au film with a thickness of 11 nm. The photoanode was also shown to have minimal electron-hole recombination due to its nearly ideal diode quality factor.

4. MATERIALS AND METHODS

4.1. Si WAFER ETCHING PROCESS AND Au DEPOSITION

N-type Si(111) with a miscut angle 0.2º towards [11-2] and resistivity of 1.15 Ω·cm was used to produce photoanodes. The wafers were purchased from Virginia Semiconductor Inc. and were hydrogen-terminated before using. Wafers were etched in 5% HF acid for 3 minutes to remove the native oxide layer, and then soaked in 90 ºC DI water for 15 min to form a SiO_x layer, then etched again with 5% HF acid for 30 s. Indium-

gallium eutectic was applied to the back of the Si wafers to form an ohmic contact, followed by silver wire and silver print II (GC electronics) as a back contact. Silicone paste or melted Apiezon Type W wax was used to insulate the back of the Si substrates.

The gold layer was directly electrodeposited onto the Si substrate using a prepolarized bias applied before the immersion of sample into the solution to prevent the oxidation of Si in aqueous environment[24]. The plating solution was 0.1 mM $HAuCl_4$, 1 mM KCl, 1 mM H_2SO_4 and 0.1 M K_2SO_4. A potential of -1.9 V vs. Ag/AgCl electrode was used for Au deposition and prepolarization. The Au films were deposited for times of 10 s, 1 min, 5 min and 10 min and used for photoelectrochemistry measurements**.** An EG&G Model 273A or Autolab 30 potentiostat was used for all deposition and measurements above.

4.2. CYCLIC VOLTAMMETRY (CV) AND PHOTOELECTROCHEMISTRY MEASUREMENTS

The CV measurements were measured in a solution containing 0.05 M $FeSO_4$ and 0.5 M H_2SO_4. The scan rate was 20 mVs^{-1}. The $Fe^{2+/3+}$ redox couple and the sulfite SO_3^{2-} ion was used as the electrolyte in photoelectrochemical cell. The $Fe^{2+/3+}$ solution contains 1 M $FeSO_4$, 0.05 M $Fe_2(SO_4)_3$ and 0.5 M H_2SO_4 and the sulfite solution is made of 1 M Na_2SO_3 in 1 M phosphate buffer with the pH adjusted to 7.0. The photocurrent-photovoltage curves were collected by linear scan voltammetry at a 10 mVs^{-1} scan rate with 200 rpm stirring. The light source was an Oriel LCS-100 lamp, 100W xenon ozone-free with an AM 1.5 filter. The Pt wire was used as reference and a gold coil with a large surface area was used as counter electrode in the 3-electrode photoelectrochemical cell. The solid

state diode measurement of Au on Si sample was conducted by doing an LSV scan at a 10 mVs^{-1} scan rate with a silver paste/silver wire top contact to the Au surface. Either an Autolab 30 potentiostat or a PARSTAT 2273 potentiostat was used for the measurements above.

4.3. REFLECTANCE AND TRANSMITTANCE SPECTRAL MEASUREMENTS

The specular reflectance spectra of Au on Si samples and the transmittance spectra of the SO_3^{2-} and $Fe^{2+/3+}$ solutions were measured using a Varian Cary 5 UV-Vis-NIR dual-beam spectrophotometer, using a 2 nm slit bandwidth and a scan rate of 100 nm/min.

4.4. X-RAY DIFFRACTION MEASUREMENTS

The XRD measurements were done using a Philips X'Pert Materials Research diffractometer with Cu Kα_1 radiation source. A crossed slit collimator with 2 mm divergence slit and 2 mm mask with a Ni filter and a 0.27° parallel plate collimator were used for X-ray pole figure measurements.

4.5. SEM AND TEM MEASUREMENTS

SEM images were obtained using a FEI Helios Nanolab Dualbeam microscope with accelerating voltages ranging from 5 to 15 kV. Focused ion beam lift-off of samples for TEM cross-sectional analysis was done using an FEI Scios dualbeam microscope. A thin carbon layer was sputtered on the sample to protect the Au films from being damaged by the ion beam during cross-sectioning. High resolution TEM images and electron diffraction patterns were obtained with an FEI Tecnai F30 transmission electron microscope

SUPPORTING INFORMATION

PHOTOELECTROCHEMISTRY OF ULTRATHIN, SEMITRANSPARENT, AND CATALYTIC GOLD FILMS ELECTRODEPOSITED EPITAXIALLY ONTO N-SILICON(111)

*Qingzhi Chen and Jay A. Switzer**

Missouri University of Science & Technology, Department of Chemistry and Graduate Center for Materials Research, Rolla, MO 65409-1170, USA.

correspondence to: jswitzer@mst.edu

1. Photoelectrochemical efficiency calculations. The fill factor (FF) is calculated from Equation 1:

$$\mathrm{FF} = \frac{J_{\mathrm{M}} \times V_{\mathrm{M}}}{J_{\mathrm{SC}} \times V_{\mathrm{OC}}} \quad (1)$$

where J_{M} is the current density at the maximum power point, V_{M} is the voltage at the maximum power point, V_{OC} is the open circuit voltage, and J_{SC} is the short-circuit current density. The efficiency is calculated from Equation 2:

$$\text{efficiency} = \frac{J_{\mathrm{M}} \times V_{\mathrm{M}}}{P_{\mathrm{input}}} \quad (2)$$

where P_{input} is the power input, which is 100 $\mathrm{mWcm^{-2}}$ in our studies.

2. X-ray diffraction. The symmetric XRD 2-Theta scan showing that the Au on Si(111) grows with a [111] out-of-plane orientation is shown in Fig. S1, and the calculated stereographic projection for single-crystal Si(111) is shown in Fig. S2.

3. Light absorption of the electrolyte solution. A Varian Cary 5 UV-Vis-NIR dual-beam spectrophotometer was used for determining the absorption of the light in the $Fe^{2+/3+}$ electrolyte to estimate the light loss through the solution. The wavelength range was from 200 to 1000 nm and the measured spectrum is shown in Fig. S3. The absorption spectrum of the sulfite solution is shown in Fig. S4.

4. The stability of Au on n-Si(111) of different thicknesses in the $Fe^{2+/3+}$ solution. The zoom-in details of photocurrent-open circuit photovoltage relationship is shown in Fig. S5 for a photoanode after various irradiation times.

5. Series resistance calculation. The series resistance of the 10 min Au on Si photoanode after different hours of stability test was determined using the method developed by Araujo et al. based on the single-diode model.[1,2] The series resistance R_S of the photoanode can be obtained by measuring the area A under the I-V curve, and can be written as:

$$R_S = 2 \cdot \left(\frac{V_{OC}}{J_{SC}} - \frac{A}{J_{SC}^2} - \frac{kT}{e} \frac{n}{J_{SC}} \right) \tag{3}$$

Figure S6 shows the initial photovoltage-photocurrent curve of the 10 min Au on Si photoanode. The area A is marked as the red region and is calculated to be 0.0015 $V \cdot A/cm^2$. Hence, the R_S is 11.3 $\Omega \cdot cm^2$. Likewise, the R_S of the photoanode after 18h, 40h and 62h of stability test can be also determined to be 12.7 $\Omega \cdot cm^2$, 18.6 $\Omega \cdot cm^2$ and 35.2 $\Omega \cdot cm^2$.

6. One-diode model fitting. One-diode model fitting of the photocurrent vs. photovoltage curves are shown in Fig. S7 using the measured series resistances from the previous section.

SUPPLEMENTARY TABLES

Table S1. Photovoltaic parameters (J_{sc}, V_{oc}, fill factor and efficiency) as function of Au coverage for $Fe^{2+/3+}$ photoelectrochemical cell

Au deposition time	J_{SC} ($mA \cdot cm^{-2}$)	V_{OC} (V)	Fill factor (%)	Efficiency (%)
10 s	11.9	0.34	55	2.21
1 min	10.4	0.33	57	1.96
5 min	11.1	0.26	49	1.39
10 min	8.9	0.25	40	0.90

Table S2. Dark saturation current density, barrier height and diode quality factor as a function of Au coverage for $Fe^{2+/3+}$ photoelectrochemical cell

Au deposition time	J_S ($\times 10^{-7}$ $A \cdot cm^{-2}$)	Barrier height (eV)	Diode quality factor
10 s	1.26	0.81	1.16
1 min	0.75	0.82	1.08
5 min	13.2	0.75	1.11
10 min	30.2	0.73	1.24

SUPPLEMENTARY FIGURES

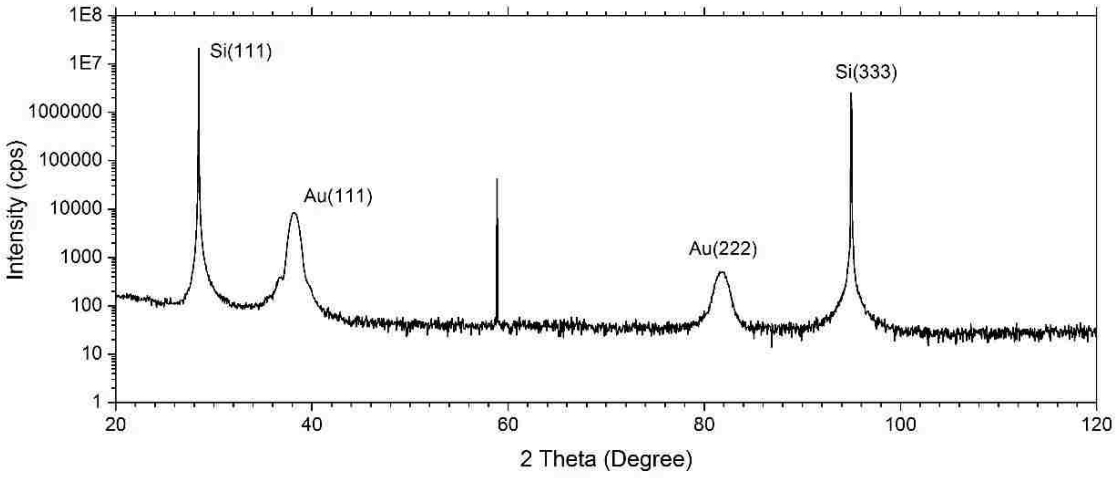

Figure S1. Symmetrical 2theta XRD scan of 5 min Au on n-Si(111), showing a [111] out-of-plane orientation for Au.

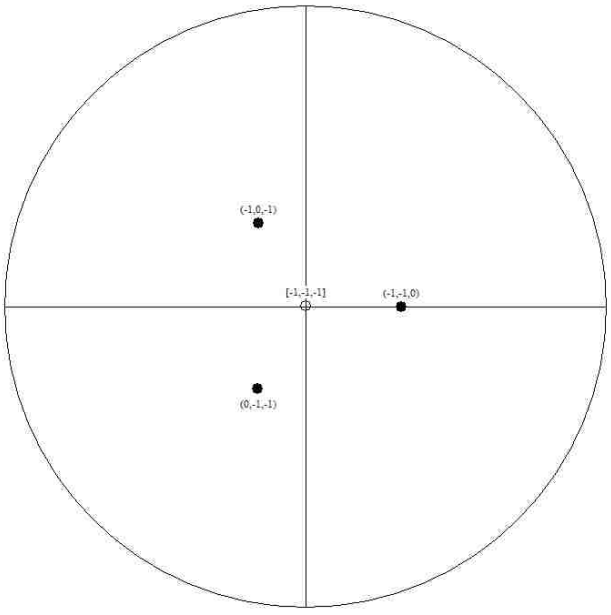

Figure S2. Calculated stereographic projection the of Si(220) pole figure for a [111]-oriented Si single crystal. The spots occur at a tilt angle of 35.3º, corresponding to the angle between the [111] and [110] directions.

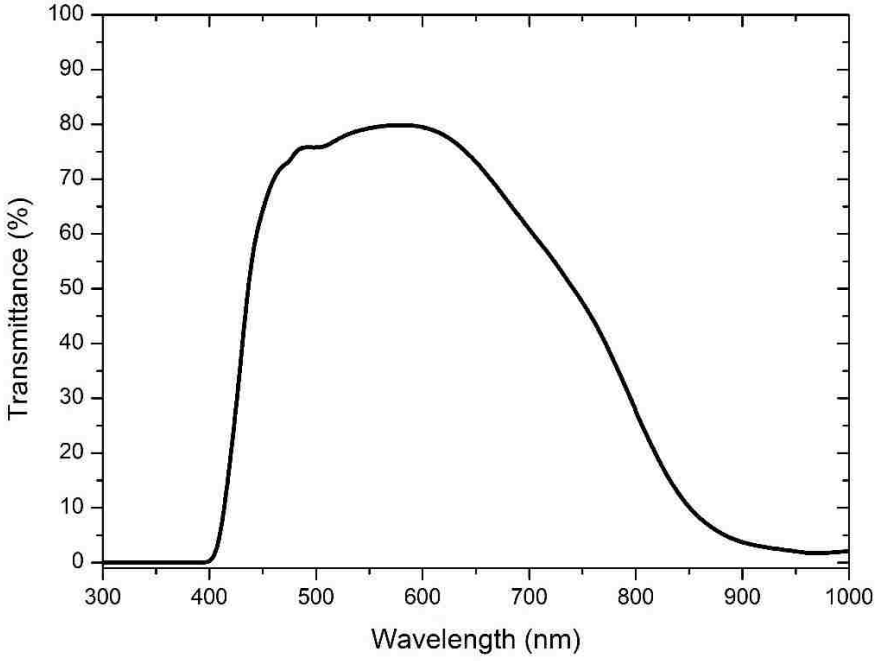

Figure S3. UV-vis absorption spectrum of the $Fe^{2+/3+}$ electrolyte solution.

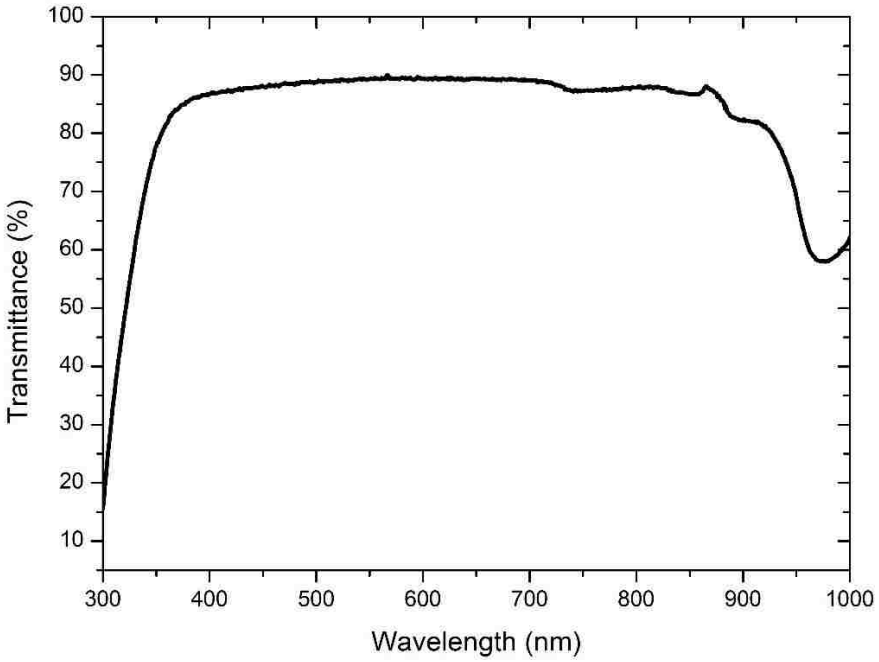

Figure S4. UV-vis absorption spectrum of the sulfite electrolyte solution

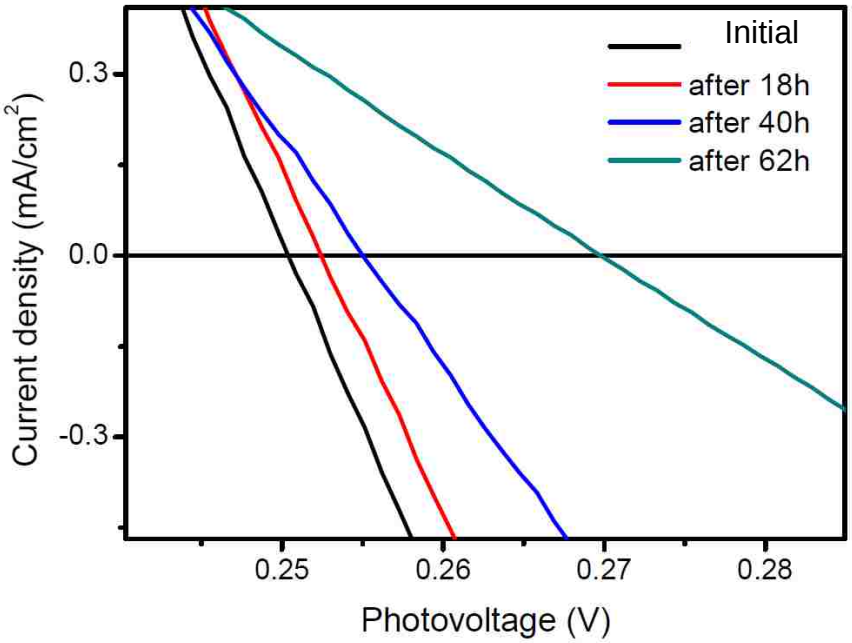

Figure S5. Zoom-in details for photocurrent-photovoltage relations showing the open-circuit photovoltage change of the 10 min Au on n-Si after 0, 18, 40, and 62 hr. of irradiation with AM 1.5 light at one sun.

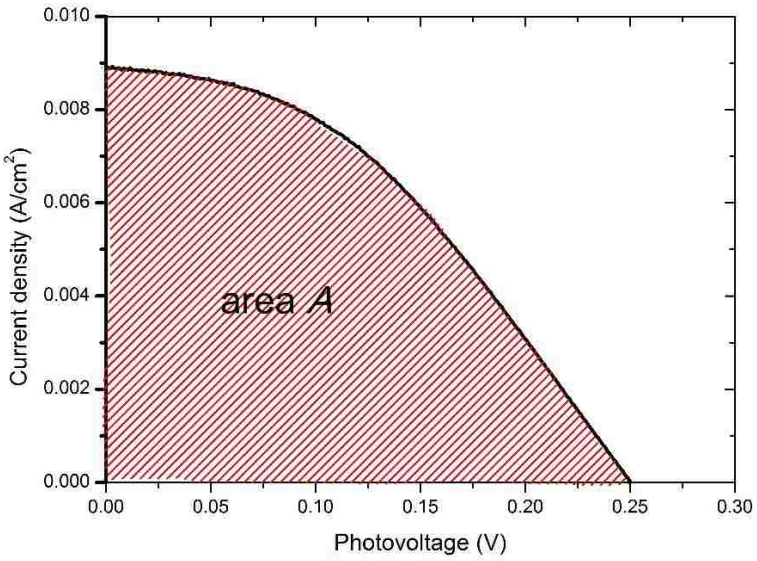

Figure S6. Photocurrent-photovoltage curve of the 10 min Au on Si photoanode. The red region is the area A for R_S determination.

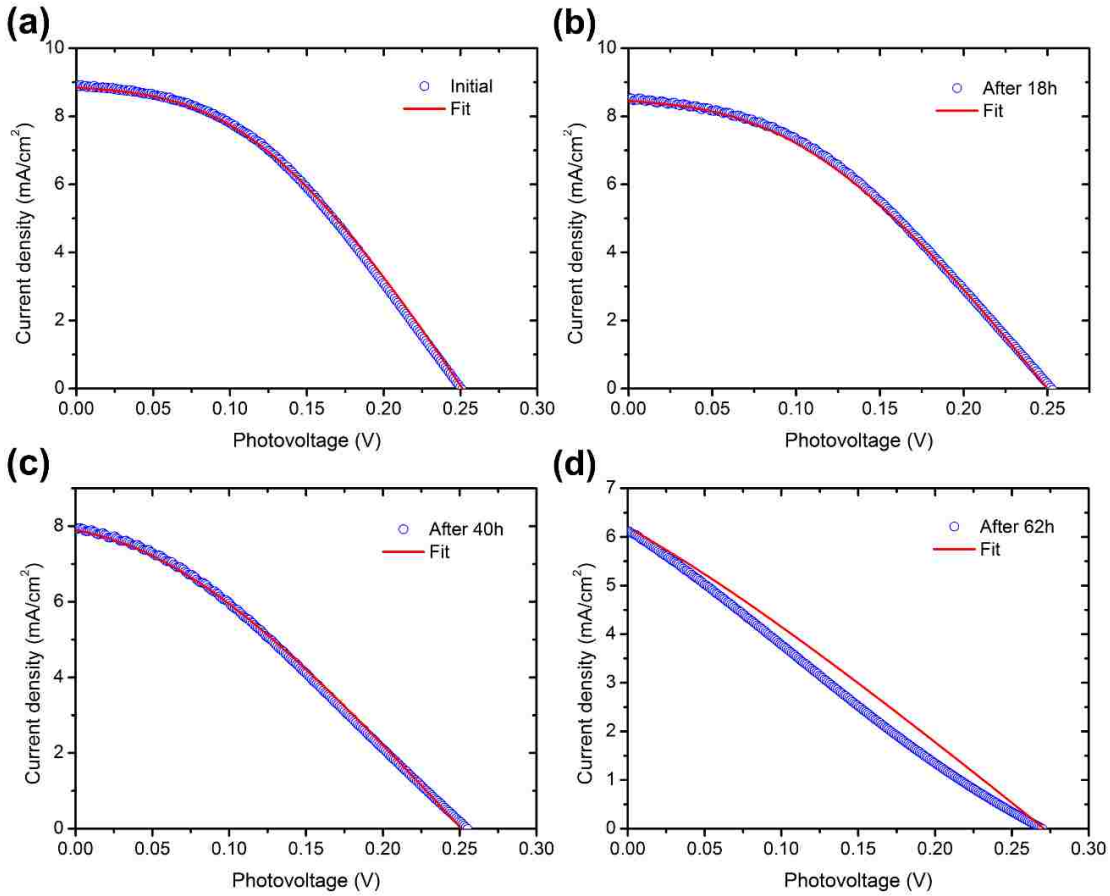

Figure. S7. One-diode model fitting of the photocurrent vs. photovoltage curves for a) initial 10 min Au on n-Si and b) after 18 h, c) 40 h and d) 62 h of stability test in $Fe^{2+/3+}$ using the calculated series resistance R_S. The initial series resistance was 11.3 Ω·cm^2, but it increased to 12.7 Ω·cm^2 after 18 hours, 18.6 Ω·cm^2 after 40 hours, and 35.2 Ω·cm^2 after 62 hours. The fitted curves are represented as red lines and the original photocurrent curves as blue circles. The J_S used for fitting was the original measured value of 3.02×10^{-6} Acm^{-2} for a) and b), 2.8×10^{-6} Acm^{-2} for c) and 1.37×10^{-6} Acm^{-2} for d) to fit the actual V_{OC}, which also indicates that the barrier heights increased over time.

REFERENCES

(1) Araujo, G. L.; Sanchez, E. A New Method for Experimental Determination of the Series Resistance of a Solar Cell. *IEEE Trans. Electron Devices* **1982**, *ED-29*, 1511–1513.

(2) Pysch, D.; Mette, A.; Glunz, S. W. A Review and Comparison of Different Methods to Determine the Series Resistance of Solar Cells. *Sol. Energy Mater. Sol. Cells* **2007**, *91*, 1698–1706.

AUTHOR INFORMATION

Corresponding Author

*E-mail: jswitzer@mst.edu

Author Contributions

The manuscript was written through contributions of both authors. The authors have given approval to the final version of the manuscript.

Notes

The authors declare no competing financial interest.

Supporting Information

UV-Vis absorption spectrum of the $Fe^{2+/3+}$ electrolyte solution and the sulfite electrolyte solution, series resistance calculation, tables of photovoltaic parameters of Au on Si for $Fe^{2+/3+}$ cell, symmetrical 2theta XRD scan of Au on Si, calculated stereographic projection of the Si(220) pole figure and one-diode model fitting of the photocurrent vs. photovoltage curves after Au on Si stability tests(file type, PDF).

This material is available free of charge via the Internet at http://pubs.acs.org.

ACKNOWLEDGEMENT

The material is based on work supported by the U.S. Department of Energy, Office of Basic Energy Sciences, under Grant No. DE-FG02-08ER46518.

REFERENCES

(1) Lewis, N. S. Research Opportunities to Advance Solar Energy Utilization. *Science* **2016**, *351* (6271), aad1920.

(2) Miller, E. L. Photoelectrochemical Water Splitting. *Energy Environ. Sci.* **2015**, *8*, 2809–2810.

(3) Kang, D.; Kim, T. W.; Kubota, S. R.; Cardiel, A. C.; Cha, H. G.; Choi, K. S. Electrochemical Synthesis of Photoelectrodes and Catalysts for Use in Solar Water Splitting. *Chem. Rev.* **2015**, *115*, 12839–12887.

(4) Reece, S. Y.; Hamel, J. A.; Sung, K.; Jarvi, T. D.; Esswein, A. J.; Pijpers, J. J. H.; Nocera, D. G. Wireless Solar Water Splitting Using Silicon-Based Semiconductors and Earth-Abundant Catalysts. *Science* **2011**, *334* (6056), 645–648.

(5) Chemelewski, W. D.; Lee, H. C.; Lin, J. F.; Bard, A. J.; Mullins, C. B. Amorphous FeOOH Oxygen Evolution Reaction Catalyst for Photoelectrochemical Water Splitting. *J. Am. Chem. Soc.* **2014**, *136*, 2843–2850.

(6) Kim, T. W.; Choi, K.-S. Nanoporous $BiVO_4$ Photoanodes with Dual-Layer Oxygen Evolution Catalysts for Solar Water Splitting. *Science* **2014**, *343* (6174), 990–994.

(7) Ahmed, M. G.; Kretschmer, I. E.; Kandiel, T. A.; Ahmed, A. Y.; Rashwan, F. A.; Bahnemann, D. W. A Facile Surface Passivation of Hematite Photoanodes with TiO_2 Overlayers for Efficient Solar Water Splitting. *ACS Appl. Mater. Interfaces* **2015**, *7*, 24053–24062.

(8) Li, X.; Bassi, P. S.; Boix, P. P.; Fang, Y.; Wong, L. H. Revealing the Role of TiO_2 Surface Treatment of Hematite Nanorods Photoanodes for Solar Water Splitting. *ACS Appl. Mater. Interfaces* **2015**, *7*, 16960–16966.

(9) Switzer, J. A. The N-Silicon/Thallium(III) Oxide Heterojunction Photoelectrochemical Solar Cell. *J. Electrochem. Soc.* **1986**, *133*, 722–728.

(10) Sun, K.; Saadi, F. H.; Lichterman, M. F.; Hale, W. G.; Wang, H.-P.; Zhou, X.; Plymale, N. T.; Omelchenko, S. T.; He, J.-H.; Papadantonakis, K. M.; Brunschwig, B. S. and Lewis, N. S. Stable Solar-Driven Oxidation of Water by Semiconducting Photoanodes Protected by Transparent Catalytic Nickel Oxide Films. *Proc. Natl. Acad. Sci.* **2015**, 3612–3617.

(11) Hu, S.; Shaner, M. R.; Beardslee, J. A.; Lichterman, M.; Brunschwig, B. S.; Lewis, N. S. Amorphous TiO_2 Coatings Stabilize Si, GaAs, and GaP Photoanodes for Efficient Water Oxidation. *Science* **2014**, *344*, 1005–1009.

(12) Chen, Y. W.; Prange, J. D.; Dühnen, S.; Park, Y.; Gunji, M.; Chidsey, C. E. D.; McIntyre, P. C. Atomic Layer-Deposited Tunnel Oxide Stabilizes Silicon Photoanodes for Water Oxidation. *Nat. Mater.* **2011**, *10*, 539–544.

(13) Ji, L.; Hsu, H. Y.; Li, X.; Huang, K.; Zhang, Y.; Lee, J. C.; Bard, A. J.; Yu, E. T. Localized Dielectric Breakdown and Antireflection Coating in Metal-Oxide-Semiconductor Photoelectrodes. *Nat. Mater.* **2017**, *16*, 127–131.

(14) Kenney, M. J.; Gong, M.; Li, Y.; Wu, J. Z.; Feng, J.; Lanza, M.; Dai, H. High-Performance Silicon Photoanodes. *Science* **2013**, *342*, 836–840.

(15) Prod'Homme, P.; Maroun, F.; Cortès, R.; Allongue, P. Electrochemical Growth of Ultraflat Au(111) Epitaxial Buffer Layers on H-Si(111). *Appl. Phys. Lett.* **2008**, *93*, 171901.

(16) Switzer, J. A.; Hill, J. C.; Mahenderkar, N. K.; Liu, Y. C. Nanometer-Thick Gold on Silicon as a Proxy for Single-Crystal Gold for the Electrodeposition of Epitaxial Cuprous Oxide Thin Films. *ACS Appl. Mater. Interfaces* **2016**, *8*, 15828–15837.

(17) Mahenderkar, N. K.; Chen, Q.; Liu, Y.-C.; Duchild, A. R.; Hofheins, S.; Chason, E.; Switzer, J. A. Epitaxial Lift-off of Electrodeposited Single-Crystal Gold Foils for Flexible Electronics. *Science* **2017**, *355*, 1203–1206.

(18) Bard, A. J.; Parsons, R.; Jordan, J. *Standard Potentials in Aqueous Solutions*, 1st ed.; M. Dekker: New York, 1985.

(19) Maaroof, A. I.; Gentle, A.; Smith, G. B.; Cortie, M. B. Bulk and Surface Plasmons in Highly Nanoporous Gold Films. *J. Phys. D. Appl. Phys.* **2007**, *40*, 5675–5682.

(20) Bochmann, H. G.; Vielstich, W. On the Reaction Rate of the Fe^{2+}/Fe^{3+} Redox Couple in Sulfate Solution. *Electrochim. Acta* **1988**, *33*, 805–809.

(21) Hill, J. C.; Landers, A. T.; Switzer, J. A. An Electrodeposited Inhomogeneous Metal-Insulator-Semiconductor Junction for Efficient Photoelectrochemical Water Oxidation. *Nat. Mater.* **2015**, *14*, 1150–1155.

(22) Li, Z.; Luo, W.; Zhang, M.; Feng, J.; Zou, Z. Photoelectrochemical Cells for Solar Hydrogen Production: Current State of Promising Photoelectrodes, Methods to Improve Their Properties, and Outlook. *Energy Environ. Sci.* **2013**, *6*, 347–370.

(23) Sze, S. M. *Physics of Semiconductor Devices*, 3rd Ed.; Wiley-Interscience, Inc.: New York, 2007.

(24) Tung, R. T. Electron Transport at Metal-Semiconductor Interfaces: General Theory. *Phys. Rev. B* **1992**, *45*, 13509–13523.

(25) Nakato, Y.; Ueda, K.; Yano, H.; Tsubomura, H. Effect of Microscopic Discontinuity of Metal Overlayers on the Photovoltages in Metal-Coated Semiconductor-Liquid Junction Photoelectrochemical Cells for Efficient Solar Energy Conversion. *J. Phys. Chem.* **1988**, *92*, 2316–2324.

(26) Rossi, R. C.; Lewis, N. S. Investigation of the Size-Scaling Behavior of Spatially Nonuniform Barrier Height Contacts to Semiconductor Surfaces Using Ordered Nanometer-Scale Nickel Arrays on Silicon Electrodes. *J. Phys. Chem. B* **2001**, *105*, 12303–12318.

(27) Card, H. C.; Rhoderick, E. H. Studies of Tunnel MOS Diodes I. Interface Effects in Silicon Schottky Diodes. *J. Phys. D. Appl. Phys.* **1971**, *4*, 1589–1601.

(28) Chen, L.; Yang, J.; Klaus, S.; Lee, L. J.; Woods-Robinson, R.; Ma, J.; Lum, Y.; Cooper, J. K.; Toma, F. M.; Wang, L. W.; Sharp, I. D.; Bell, A.T. and Ager, J. W. P-Type Transparent Conducting Oxide/n-Type Semiconductor Heterojunctions for Efficient and Stable Solar Water Oxidation. *J. Am. Chem. Soc.* **2015**, *137*, 9595–9603.

(29) Oh, J.; Yuan, H. C.; Branz, H. M. An 18.2%-Efficient Black-Silicon Solar Cell Achieved through Control of Carrier Recombination in Nanostructures. *Nat. Nanotechnol.* **2012**, *7*, 743–748.

II. EPITAXIAL LIFT-OFF OF ELECTRODEPOSITED SINGLE-CRYSTAL GOLD FOILS FOR FLEXIBLE ELECTRONICS

*Naveen K. Mahenderkar[1], Qingzhi Chen[2], Ying-Chau Liu[2], Alexander R. Duchild[2], Seth Hofheins[2], Eric Chason[3], and Jay A. Switzer[2,]**

[1]Department of Materials Science and Engineering and Graduate Center for Materials Research, Missouri University Science and Technology Rolla, Missouri, 65409.
[2]Department of Chemistry and Graduate Center for Materials Research, Missouri University Science and Technology Rolla, Missouri, 65409.
[3]School of Engineering, Brown University, Providence, Rhode Island, 02912

*Email: jswitzer@mst.edu

ABSTRACT

We introduce a simple and inexpensive procedure for epitaxial lift-off of wafer-size flexible and transparent foils of single-crystal gold using silicon as a template. Lateral electrochemical undergrowth of a sacrificial SiO_x layer was achieved by photoelectrochemically oxidizing silicon under light irradiation. A 28-nanometer-thick gold foil with a sheet resistance of 7 ohms per square showed only a 4% increase in resistance after 4000 bending cycles. A flexible organic light-emitting diode based on tris(bipyridyl)ruthenium(II) that was spin-coated on a foil exploited the transmittance and flexibility of the gold foil. Cuprous oxide as an inorganic semiconductor that was epitaxially electrodeposited onto the gold foils exhibited a diode quality factor n of 1.6 (where n = 1.0 for an ideal diode), compared with a value of 3.1 for a polycrystalline

deposit. Zinc oxide nanowires electrodeposited epitaxially on a gold foil also showed flexibility, with the nanowires intact up to 500 bending cycles.

1. INTRODUCTION

The Single-crystal silicon (Si) is the bedrock of semiconductor devices; its high crystalline perfection minimizes electron-hole recombination, and its dense SiOx native oxide minimizes surface states. There is interest in moving beyond the planar structure of conventional Si-based chips to produce flexible electronic devices such as wearable solar cells, sensors, and flexible displays.[1-5] Flexible devices and beautiful architectures have been produced using ultrathin foils of Si.[6-8] Conductive polymers,[9] carbon nanotubes,[10] graphene,[11] and metal nanostructures[12,13] have been used as transparent and flexible substrates for flexible electronics. Ultrathin (5 to 30 nm) metal films[14,15] have relatively high optical transmittance, flexibility, improved device efficiency, and low sheet resistance. However, they usually are grown by vacuum evaporation or sputtering, which gives a polycrystalline or textured deposit. Polycrystalline electronic materials suffer from electron-hole recombination at grain boundaries.[16] To expand the palette of electronic materials beyond planar Si, an inexpensive source of highly ordered material is needed that can serve as an inert substrate for the epitaxial growth of grain boundary-free semiconductors, optical materials, and superconductors.

We show that wafer-size transparent and flexible single-crystal foils of gold (Au) can be produced by a simple and inexpensive lift-off procedure using single-crystal Si as the template for electrochemical epitaxial growth. The transparency of these single-crystal

Au foils is exploited to fabricate a flexible organic light-emitting diode (OLED) based on tris(bipyridyl)ruthenium(II). The single-crystal nature of the Au is used to produce an inorganic diode based on epitaxial cuprous oxide (Cu_2O) that has more ideal diode characteristics than a diode based on polycrystalline Cu_2O.

2. RESULTS AND DISCUSSION

Epitaxial lift-off of films on single-crystal substrates by dissolving a sacrificial adhesion layer can produce free-standing single-crystal foils.[17] The epitaxial lift-off procedure for ultrathin single-crystal foils of Au electrodeposited onto Si(111) substrate is shown in Figure 1. Electrodeposition of epitaxial Au on a Si(111) substrate was carried out using the method developed by Allongue and co-workers.[18,19] Previously, we showed that epitaxial electrodeposition of Au on Si(111), Si(100), and Si(110) substrates can serve as a proxy for bulk single-crystal Au.[20] Single-crystal Si(111) with a 0.2 miscut toward $[11\bar{2}]$ and a resistivity of 1.15 Ω·cm was used as the substrate to grow the Au foils (Figure 1A). The deposition was performed at room temperature in a solution containing 0.1 mM $HAuCl_4$, 1 mM KCl, 1 mM H_2SO_4, and 0.1 M K_2SO_4 with a Si electrode that was prepolarized at -1.9 V versus Ag/AgCl before inserting it in the solution (Figure 1B). Prepolarizing the electrode inhibited the formation of an amorphous native oxide layer on the surface of Si and enabled epitaxial growth of Au.

After the epitaxial growth of Au, lateral undergrowth of a sacrificial SiO_x layer was achieved by photoelectrochemically oxidizing Si under irradiation of light at +0.75 V versus Ag/AgCl in 0.5M H_2SO_4 solution (Figure 1C). Au/n-Si forms a Schottky

(rectifying) junction, so irradiation of light is required to generate holes at the Au/n-Si interface to oxidize the Si. The epitaxy of the Au foil was maintained during the lateral undergrowth of SiO_x, analogous to the epitaxial lateral overgrowth process in silicon-on-insulator technology.[21] A polymer adhesive (tape or hot glue) was applied to the Au surface as a support and facilitator for foil separation (Figure 1D). The SiO_x layer was etched using dilute (5%) hydrofluoric acid to detach the Au foil from the Si substrate (Figure 1E); this enabled an effortless separation of the foil (Figure 1F). Both the tape and hot glue have high optical transmittance in the visible range (400 to 800 nm) and are resistant to chemical etching procedures. After the foil separation, the Si substrate was etched using a 0.6 M KI and 0.1 M I_2 solution to dissolve any residual Au and then reused. Because only a 2-to 3-nm-thick layer of SiO_x is removed during each fabrication cycle without extensive roughening, the Si should be reusable thousands of times.

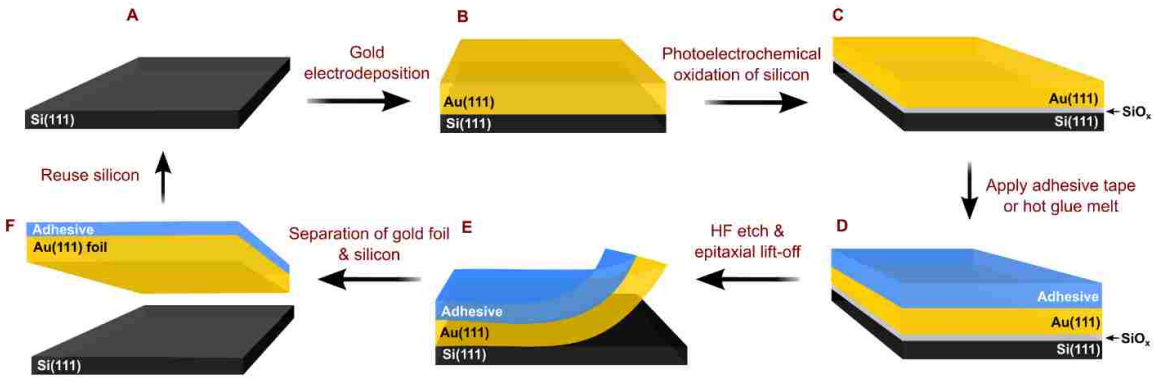

Figure 1. Schematic for epitaxial lift-off of single-crystal Au foil. (A) Miscut n-type Si(111) wafer without the native oxide layer. (B) Epitaxial electrodeposition of Au on Si(111) from a 0.1 mM $HAuCl_4$ solution at -1.9 V versus Ag/AgCl with prepolarized electrode. (C) Photoelectrochemical oxidation of Si under irradiation of light in 0.5 M H_2SO_4 solution at 0.75 V versus Ag/AgCl. (D) A polymer adhesive (tape/hot glue) is applied to the surface of Au to aid the foil separation. (E) Sacrificial SiO_x interlayer is etched using dilute (5%) hydrofluoric acid to separate the foil from Si substrate. (F) Completely detached single-crystal Au foil from Si surface.

High-resolution transmission electron microscopy (HRTEM) was used to study the interfacial changes during photoelectrochemical oxidation of Si. The as-deposited 30-min film (i.e., 30 min of deposition time) did not show an interfacial SiO_x layer between the Si(111) and Au(111), as seen by the abrupt transition at the interface in Figure 2A. Electron diffraction patterns for the as-deposited layers of Au on Si showed a spot pattern with in-plane and out-of-plane order (Figure S1). After the photoelectrochemical oxidation of Si, an amorphous SiO_x interface with a thickness of 2.45 nm was evident in Figure 2B. Native oxide formation on the Si surface in ambient air is limited to 0.5 to 1 nm because of the dense pinhole-free oxide layer that protects the Si from further oxidation. However, during photoelectrochemical oxidation of Si, tunneling of electrons through the insulating oxide layer caused the SiO_x layer to grow thicker. The tunneling of electrons completely ceased when the oxide layer reached a thickness of 2.0 to 2.5 nm and the photocurrent dropped nearly to zero (Figure S2). The electron diffraction pattern of Au on Si with an interfacial oxide layer showed a similar spot pattern, indicating that the epitaxy was maintained after the lateral undergrowth of SiO_x (Figure S3). Both micrographs (Figure 2, A and B) are viewed along the $[11\bar{2}]$ zone axis, and the measured d-spacings for Au and Si are consistent with bulk values.

Scanning electron microscopy (SEM) was performed to study the surface morphology and the initial nucleation and growth of Au foils. All of the foils for SEM were separated with an adhesive tape as the support layer. Figure 2C shows a Au foil formed after 5 min with a fractal morphology that had been reported for evaporated ultrathin films of Au.[22,23] We attribute these fractal features to the diffusion-limited aggregation of Au on the surface of Si during the initial nucleation period. This Au foil has a coverage of 56%

and appears to be at the percolation threshold thickness (5 to 6 nm), in agreement with the results of Hövel *et al.*[24] Beyond the percolation threshold, the fractal features are interconnected in a large network mesh with electrical connectivity across the entire foil. Fig. 2D shows Au foils deposited for 10 min with 70% coverage and Fig 2F and 2G show Au foils deposited for 20 min and 30 min, respectively, are shown in Figure 2, E and F.

The applicability of Au foils as a substrate was shown by depositing and characterizing inorganic semiconductor thin film and nanowires. Cu_2O was electrodeposited on a 30 min Au foil (Fig. 2G) and is used to study the diode characteristics. Zinc oxide (ZnO) nanowires were electrodeposited on a 10-min Au foil (Fig. 2H) and are subjected to 500 bending cycles with the radius of curvature of 3 mm. The ZnO remained intact after the bending cycles, which can be attributed to its nanowire morphology and the

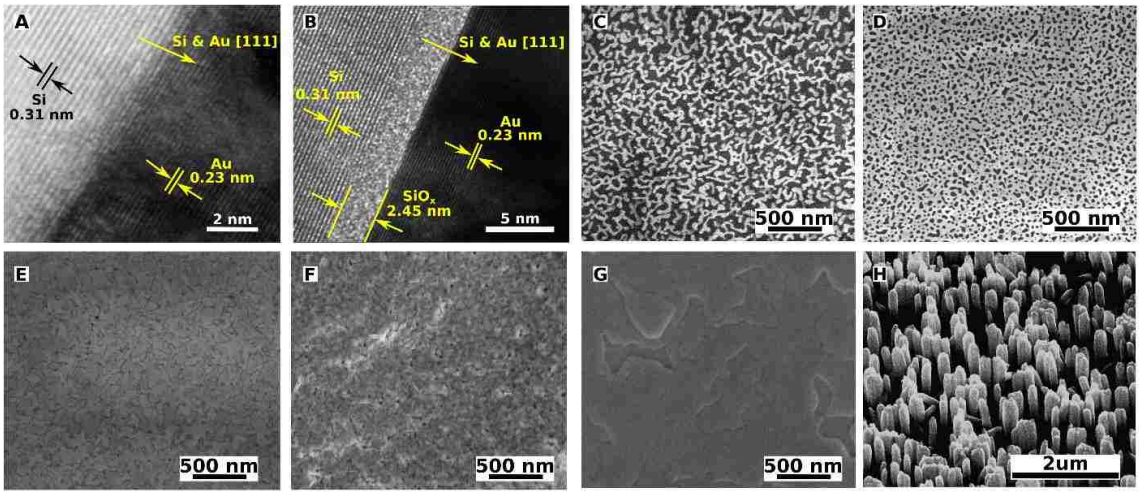

Figure 2. Electron microscopy of the single-crystal Au, epitaxial Cu_2O, and epitaxial ZnO. High-resolution TEM cross-section of epitaxial Au on Si (A) without SiO_x interlayer for the as-deposited film and (B) with the SiO_x layer after photoelectrochemical oxidation of Si. Surface morphology of the Au foils deposited for (C) 5 min (7 nm), (D) 10 min (11 nm), (E) 20 min (21 nm), and (F) 30 min (28 nm). (G) Electrodeposited epitaxial Cu_2O on a 30 min Au foil and (H) Electrodeposited ZnO nanowires on a 10 min Au foil subjected to 500 bending cycles.

flexibility of Au foil. Although the 5- and 10- min Au foils appear porous, foils beyond the percolation threshold thickness (5 to 6 nm) enable electrical contact over the entire sample area and make electrodeposition feasible.

We probed epitaxial Au on Si and free-standing Au foils using x-rays to study the out-of-plane and in-plane orientations. Figure 3A shows the x-ray diffraction (XRD) pattern of a 30-min Au deposition on Si, where Au follows the [111] orientation of Si, indicating a high out-of-plane order. The Au thickness on Si was measured from the interference fringes in the XRD pattern (Figure 3B). Satellite peaks (Laue oscillations) around a Bragg peak caused by constructive and destructive interference of x-rays reflected from Si-Au and Au-air interfaces were used to precisely measure the Au thickness.[19] Figure 3B shows Laue oscillations around the Au(111) peak for Au films on Si as a function of deposition time. The film thickness was determined from the satellite peak positions according to

$$t = \left(\frac{(L_1 - L_2)\lambda}{2(\sin\theta_1 - \sin\theta_2)} \right) \quad (1)$$

where t is the film thickness, L is the satellite peak order (numbering of peaks in Fig. 3B), λ is the x-ray wavelength (0.15418 nm), and θ is the satellite peak angle. The calculated thicknesses from the Laue oscillations for the corresponding deposition times are listed in Figure 3B. A linear dependence of thickness with time was observed (Figure S4). Figure 3C shows the XRD pattern of a segment of Au foil and electrodeposited Cu_2O and ZnO on Au foil. Both the Au foil and the electrodeposited Cu_2O had a strong [111] out-of-plane orientation. The thickness of a 10-min deposition of Au on Si agreed closely with that of Au foil measured using Laue oscillations (Figure S5). The ZnO also grew epitaxially on

Au foil but showed a strong [0001] out-of-plane orientation because of its hexagonal crystal structure.

The in-plane orientation and the epitaxial relation of the Au on Si, Au foil, Cu_2O, and ZnO was determined with x-ray pole figures. In a pole figure, planes other than those parallel to the substrate surface are probed while tilting and rotating the sample through a series of tilt and azimuthal angles (Figure S6). Figure 3D shows a (220) pole figure of Si(111), with three spots separated azimuthally by 120° at a tilt angle of 35.5°, corresponding to the three-fold symmetry of the (111) plane. A (220) pole figure of Au(111) on Si(111) is shown in Figure S7 with three spots expected at a tilt angle of 35.5°; however, there are also an additional three spots separated azimuthally by 60°. The two sets of spots on the (220) pole figure of Au correspond to the 180° in-plane rotation of parallel and antiparallel domains. Figure 3E shows a (220) pole figure of Au(111) foil, with the six spots at a tilt angle of 35.5° separated azimuthally by 60°. This pattern shows that the Au maintained its high in-plane and out-of-plane order after the foil separation. Figure 3F shows a (220) pole figure of Cu_2O(111) electrodeposited on Au(111) foil with the expected six spots at a tilt angle of 35.5°. Figure 3G shows a (102) pole figure of ZnO(002) with six spots at a tilt angle of 42.77^o separated azimuthally by 60^o. The six spots for ZnO are expected from the six-fold symmetry of the (0002) basal plane of the hexagonal crystal structure.

To understand the epitaxial relation, it is crucial to look at the lattice mismatch of the film and the substrate. The lattice mismatch can be defined as $((d_{film}-d_{substrate})/d_{substrate})$, where d is the lattice spacing of the plane parallel to the substrate. Au on Si has lattice mismatch of -24.9%, which is too high to produce epitaxial deposits. Therefore, the epitaxy in the Au-

Si system can be explained by the formation of coincidence site lattices (CSLs), in which four unit meshes of Au coincide with three unit meshes of Si.[20] These CSLs lower the mismatch from -24.9% for a single unit cell to +0.13% for the CSL (Fig. S8). Similarly, the lattice mismatch for ZnO on Au was minimized from +12.7% to +0.16% for the CSL (Fig. S9). The lattice mismatch for Cu_2O on Au is +4.7%, which is low enough to produce cube-on-cube epitaxial films with reasonable in-plane and out-of-plane strain in the material (Fig. S10).

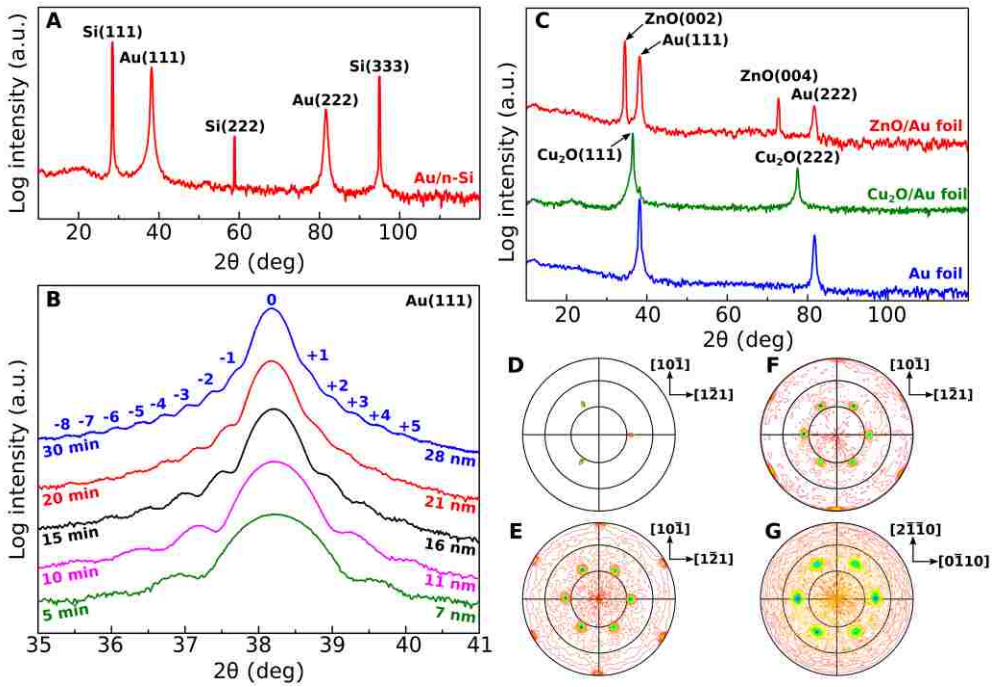

Figure 3. X-ray diffraction and pole figures to study the in-plane and out-of-plane orientation. (A) Out-of-plane orientation of electrodeposited Au(111) on Si(111). (B) Out-of-plane X-ray diffraction showing satellite peaks (Laue oscillations) caused by the constructive and destructive interference. (C) Out-of-plane orientation of a Au(111) foil, electrodeposited Cu_2O on 30 min Au foil and electrodeposited ZnO on a 10 min Au foil. In-plane orientation was determined using (D) (220) pole figure of Si(111), (E) (220) pole figure of Au(111) foil, (F) (220) pole figure of Cu_2O(111) on Au(111) foil and (G) (102) pole figure of ZnO(002) on Au(111) foil. The radial lines in the pole figure correspond to 30° increments of the tilt angle.

High optical transmittance and low sheet resistance are imperative for Au foils to be used as flexible and transparent substrates. Fig. 4A shows the photograph of a wafer-size Au foil with a diameter of 50.8 mm. Fig. 4B shows the optical transmittance of Au foils as a function of thickness. All of the foils showed a maximum in transmittance around 500 nm and the peaks slightly red-shifted with a decrease in thickness. The sheet resistance, interms of ohms per square, for all of the foils (measured with a four-point probe) increased along with transmittance as the Au foil thickness decreased. A 7-nm-thick Au foil showed the highest transmittance of 85%, and the 28-nm-thick foil showed the lowest at 25%. The maximum transmittance (~500 nm) as a function of thickness is in close agreement with previous studies on evaporated gold thin films.[25] The endurance of the Au foils as a function of sheet resistance was measured by subjecting the foils to as many as 4000 bending cycles (Fig 4C). Bending cycles for all of the foils were performed with a steel rod as a guide with a radius of curvature of 3 mm. The sheet resistance of 28 nm, 16 nm and 11 nm thick, Au foil increased by 4%, 6.3%, and 34%, respectively, after 4000 cycles of bending.

To evaluate the flexibility and transmittance of Au foils for light emission, we spincoated an OLED based on tris(bipyridyl)ruthenium(II).[26,27] The complex showed strong photoluminescence with an excitation wavelength of 455 nm and an emission of bright red-orange color around 660 nm.[26] The complex was dissolved in a 3% (w/v) polyvinyl alcohol solution, spin-coated onto a 28-nm-thick Au foil, and dried in air. An indium/gallium (InGa) eutectic was used as a back contact as a low-work function metal, whereas the Au foil acted as a high-work function contact. Figure 4D shows the current-voltage response of Au foil/$Ru^{II}(bpy)_3$/InGa junction with a diode (rectifying) behavior.

The inset in Figure 4D shows a flexible Au foil with electrogenerated chemiluminescence from the OLED at an applied forward bias of 6 V.

To study the single-crystal nature of Au foils, we prepared an inorganic diode by using electrodeposited Cu_2O on Au foil. InGa eutectic was used to make a rectifying contact to the p-Cu_2O and the Au foil substrate served as the ohmic contact. Polycrystalline Cu_2O was electrodeposited on a stainless-steel substrate from the same deposition solution at low overpotentials to produce a sample with a random orientation. Cu_2O on both the Au foil and the stainless steel were deposited for a constant charge density to maintain similar thickness. The XRD pattern of Cu_2O on stainless steel with a polycrystalline powder pattern is shown in Fig. S11. Defects or grain boundaries in a material increase the probability of electron-hole recombination and lower the overall efficiency of the diode or solar cell. In a single crystal, the diode quality factor (n) of 1 indicates diffusion-controlled currents with no electron-hole recombination in the material, but in polycrystalline materials, n varies from 2 to 7.[28,29] The n value for polycrystalline Si also increases with decreasing grain size.[29] Fig. 4E shows current-voltage responses for Cu_2O diode on a Au foil and a stainless steel. The epitaxial Cu_2O had an n of 1.6, whereas the polycrystalline Cu_2O had an n of 3.1 (Fig. 4F). The higher value of n for polycrystalline Cu_2O is consistent with previous results for films of Cu/Cu_2O Schottky diode solar cells.[30]

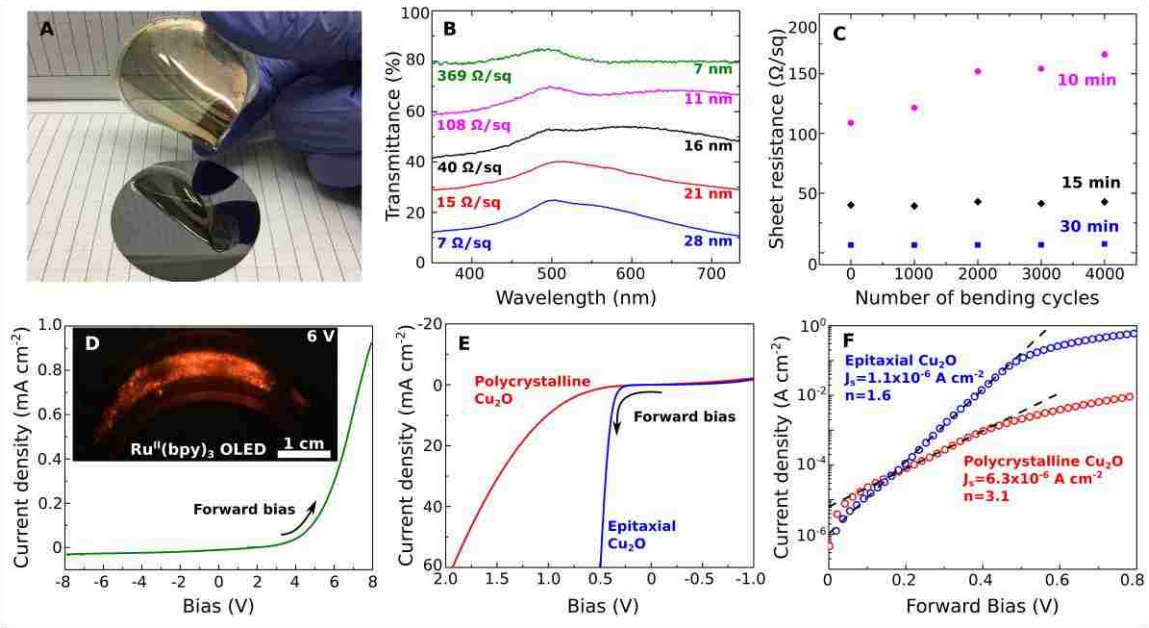

Figure 4. Transmittance, sheet resistance, and flexibility of Au foils with diode and OLED fabrication. (A) Wafer-size Au foil with a diameter of 50.8 mm, (B) Transmittance and sheet resistance of Au foils as a function of thickness. (C) Sheet resistance of Au foils as a function of bending cycles with bending curvature of 3 mm. (D) Current-voltage response of Au foil/$Ru^{II}(bpy)_3$/InGa junction showing rectifying behavior and inset shows the red-orange electrogenerated chemiluminescence of $Ru^{II}(bpy)_3BF_4$ OLED on a flexible 28 nm thick Au foil. (E) Current-voltage response of a Cu_2O diode on Au foil (epitaxial) and stainless steel (polycrystalline) substrates. (F) Dark saturation current density (J_s) and diode quality factor (n) of epitaxial and polycrystalline Cu_2O diodes measured using log(J) versus V at forward bias.

3. CONCLUSIONS

Single-crystal Au foils offer the order of traditional semiconductors such as Si wafers without the constraint of a rigid substrate. The foils are flexible and optically transparent, and show promise for producing flexible and wearable displays, solar cells, and sensors. The epitaxial growth of Cu_2O and ZnO that we have demonstrated can be applied to a wide range of inorganic semiconductors such as CdSe, CdTe, and ZnSe for

use in flexible solar cells. Because ZnO is both a wide-bandgap semiconductor and a piezoelectric material, it should be possible to produce pressure-sensitive electronic skin and LEDs based on the ZnO/Au system.[31,32] Also, Au is hypoallergenic and could serve as a platform for wearable sweat sensors for continuous health monitoring.[5] Although this work focused on the production of ordered substrates for flexible electronics, the processing method can be used to provide an inexpensive source of large metallic single crystals. These could serve as ordered substrates for photovoltaics, high-temperature superconductors, stress-free microelectromechanical systems (MEMS), catalysts, underpotential deposition, self-assembled monolayers, and molecular electronics.

SUPPORTING INFORMATION

EPITAXIAL LIFT-OFF OF ELECTRODEPOSITED SINGLE CRYSTAL GOLD FOILS FOR FLEXIBLE ELECTRONICS

*Naveen K. Mahenderkar, Qingzhi Chen, Ying-Chau Liu, Alexander R. Duchild, Seth Hofheins, Eric Chason and Jay A. Switzer**

Correspondence to: jswitzer@mst.edu

1. MATERIALS AND METHODS

1.1. Si WAFER AND ETCHING PROCEDURE

Phosphorous doped single-side polished n-Si(111) was miscut 0.2 degrees towards [11 $\bar{2}$] with resistivity of 1.15 ohm-cm. The wafer was obtained from Virginia Semiconductor Inc. Aluminum was sputtered on the back of Si wafer to form an ohmic contact and silver wire with silver paste (GC electronics, silver print II) was used to make the back contact. Silicone paste and/or nail polish was used as an insulating and inert layer on the back of Si to prevent contact in the electrolyte during electrodeposition. Si wafers prior to use were etched in 5% hydrofluoric acid (HF) solution for 30 seconds to dissolve the native oxide, then soaked in hot DI water (ca. 80-90^{o}C) for 15 minutes to passivate the surface with SiO_x layer and then etched again with 5% HF for 30 seconds and buffered hydrofluoric acid for 30 seconds to make a H-terminated surface. Ethanol was used to clean any organic residue and rinsed with DI water prior to deposition. All depositions were immediately followed by the etching process to avoid any surface passivation. After photoelectrochemical oxidation of Si, SiO_x was etched using 5% HF to separate the Au foil.

1.2. ELECTRODEPOSITION OF Au AND Au FOIL FABRICATION

Au was electrodeposited from a plating solution containing 0.1 mM $HAuCl_4$, 1 mM KCl, 1 mM H_2SO_4, and 100 mM K_2SO_4 in deionized (DI) water (*16*). The solution was prepared by adding 10 mL of a stock solution containing 1 mM $HAuCl_4$, 10 mM KCl, and 10 mM H_2SO_4 to 90 mL of DI water. Lastly, 100 mM K_2SO_4 was added as a supporting

electrolyte with a pH of ~3. All depositions used an Ag/AgCl reference electrode and a Pt coil as a high surface area counter electrode. A -1.9 V versus Ag/AgCl pre-polarized bias was applied before inserting the Si electrode into the solution and the deposition was carried out for various deposition times at room temperature with 200 rpm stirring. The key step during deposition was the pre-polarized dip of Si in the electrolyte to avoid native oxide formation and to prevent electroless deposition of Au on Si. After the deposition, films were rinsed with DI water and dried in air. Au on Si films showed no native oxide passivation at the Si interface and were stable in lab atmosphere for more than a year. As deposited Au on Si deposits were photoelectrochemically oxidized under light irradiation at an applied potential of 0.75 V versus Ag/AgCl in 0.5 M H_2SO_4 solution at room temperature. All the Au on Si samples were photoxidized for 30 minutes. A polymer adhesive or tape is applied to the Au film while on Si and then SiO_x is etched using 5% HF to detach the Au foil. All the foils after etching separated effortlessly enabling a crack-free Au foil.

1.3. ELECTRODEPOSITION OF Cu_2O And ZnO

Cu_2O was electrodeposited from a plating solution containing 0.2 M $CuSO_4.5H_2O$, 0.2 M $C_4H_6O_6$ (L-tartaric acid), and 3 M NaOH (*29, 30*). A solution of $CuSO_4$ and L-tartaric acid was prepared separately and was slowly added to the solution of 3 M NaOH. A dark blue yet translucent solution is obtained. The solution was stored at 0^oC and all the deposition were performed at 30^oC. Prolonged usage of solution at temperatures more than 30^oC causes formation of copper hydroxide and the solution color turn into opaque dark blue and eventually precipitates out. A cathodic current density of 1.0 mA/cm^2 was passed for a constant charge density of 1.8 C/cm^2 at a temperature of 30 °C and a stir rate of 200

rpm. All the deposits were rinsed with DI water and dried in air and used as deposited without any post-processing. Electrodeposition of ZnO (*31*, *32*) was performed from a solution containing 0.1 mM $Zn(NO_3)_2$ and 0.1 M KCl at an applied potential of -1.1 V versus Ag/AgCl at 70^oC and 200 rpm stirring. Electrodeposition of Au, Cu_2O and ZnO films was done using either an EG&G Model 273A or an Autolab 30 potentiostat/ galvanostat.

1.4. X-RAY DIFFRACTION MEASUREMENTS AND INTERFACE MODELS

All XRD measurements were made with a Philips X-Pert Panalytical (Materials Research Diffractometer) with Cu Kα radiation source (λ=1.54056 Å). All 2theta-omega (out-of-plane orientation) and Laue oscillation scans were done using a hybrid 2-bounce with 2xGe 220 Asym. monochromator and Ni 0.125 mm automatic beam attenuator and a 0.18^o parallel plate collimator diffracted optics. Pole figures were measured using a crossed slit collimator with 2 mm divergence slit and 2 mm mask with a Ni filter and a 0.27^o parallel plate collimator. Lattice constants for interface models and X-Ray measurements of Si were referred from JCPDS card no. 027-1402, Au from 004-0784, Cu_2O from 005-0667 and ZnO from 036-1451. All the interface models for Au on Si, Cu_2O on Au foil and ZnO on Au foil were made using VESTA (visualization for electronic and structural analysis) software ver. 3.3.2.

1.5. SEM AND TEM MEASUREMENTS

High resolution cross-section TEM images for Au on Si before and after photoelectrochemical oxidation were measured using Technai F20. SEM of Au foil, Cu_2O

and ZnO were determined using Helios Nanolab Dual beam. Focused ion-beam milling for TEM sample preparation was done using Helios Nanolab dual beam. Prior to focused ion-beam milling, the films were sputtered with a thin carbon layer using a denton sputtering system to protect the Au film during milling process and to provide a contrast difference to determine the thickness of films accurately.

1.6. TRANSMITTANCE AND SHEET RESISTANCE MEASUREMENTS

Transmittance for all the Au foils were measured using a Varian Cary 5 UV-Vis-NIR Dual-beam spectrophotometer. All the Au foils for transmittance measurement were separated using scotch tape as the support layer, therefore a bare tape sample was used in the reference beam during measurement. A baseline scan was measured without any sample in both the beam paths prior to the Au foil. The sheet resistance measurements were performed using a C4S 44/5S four-probe measurement system from Cascade Microtech, Inc. The current was applied using a Keithley 220 programmable current source and the voltage was measured using a HP 3457A multimeter. A minimum of 3 measurements were performed on each sample and averaged to obtain the sheet resistance.

1.7. TRIS(BIPYRIDYL)RUTHENIUM (II) TERAFLUOROBORATE ($[Ru(Bpy)_3](BF_4)$) SYNTHESIS AND OLED FABRICATION

$RuCl_3.3H_2O$ was dehydrated by placing the powder in an oven at 100^oC over-night and slowly cooling it to room temperature. All the reactions were performed in a fume hood. 0.083 g of dried $RuCl_3$ was mixed with 8 ml of DI water in a 25 ml Erlenmeyer flask and heated to reflux while stirring. To the solution while heating, 0.188 g of 2,2'-bipyridine

and 440 µl of 6M NaH_2PO_2 was added. The solution has a dark blackish color before heating and after refluxing at 80^oC for about 30 minutes, the solution color changes to bright orange. The water level was marked and during refluxing, DI water was added as necessary to maintain the same volume. After refluxing, a 1.5 ml solution with 0.333 g of $NaBF_4$ was added to the refluxing orange solution and stirred for 5 minutes. The solution is cooled to room temperature and then placed in a refrigerator to further cool down to enable precipitation of the complex. The solution was filtered using a Buchner funnel filtration apparatus and the precipitate was dried at room temperature. The OLED was fabricated by spin-coating the solution of $[Ru(bpy)_3](BF_4)$ dissolved in a 3% (w/v) polyvinyl alcohol (PVA) solution. The PVA solution was prepared by slowly dissolving 0.15 g of PVA in 5 ml of boiling water until everything dissolved. 0.035 g of as prepared $[Ru(bpy)_3](BF_4)$ complex was dissolved in 3 ml of PVA solution and the mixture was spin-coated on Au foil at 500 rpm. The coating was dried at room temperature for 2-3 hours. Indium-gallium eutectic was applied on the OLED coating as a back contact.

1.8. MEASUREMENT OF INTERFACIAL ENERGETICS

All current voltage response curves were measured using a PARSTAT 2273 potentiostat/galvanostat with a Au coil in contact with InGa eutectic as a back contact and the Au foil or stainless steel as front contact.

X-ray rocking curves, azimuthal scans and pole figures are texture analysis tools for highly ordered crystalline materials. All of these scans require 2θ angle fixed at the peak of interest. For example, 2θ = 47.304° for probing the Si(220) plane(s). The sample stage is tilted or rotated in different directions and angles in order to determine the in-plane

and out-of-plane order of the sample. As shown in Figure S7, rocking the sample along the axis perpendicular to the source-sample-detector plane is known as the ω scan or rocking curve. Rocking curves determine the mosaic spread of the out-of-plane orientation. Rotation of the sample around the sample normal is the φ scan, or the azimuthal scan. Tilting the sample along the axis orthogonal to both the ω and the φ axes is the χ scan (or sometimes referred to as the ψ scan). Diffraction signals collected from the azimuthal scans (φ = 0° to 360°) at each tilt angle (χ = 0° to 90°) can be used to construct a pole figure.

2. SUPPLEMENTARY FIGURES

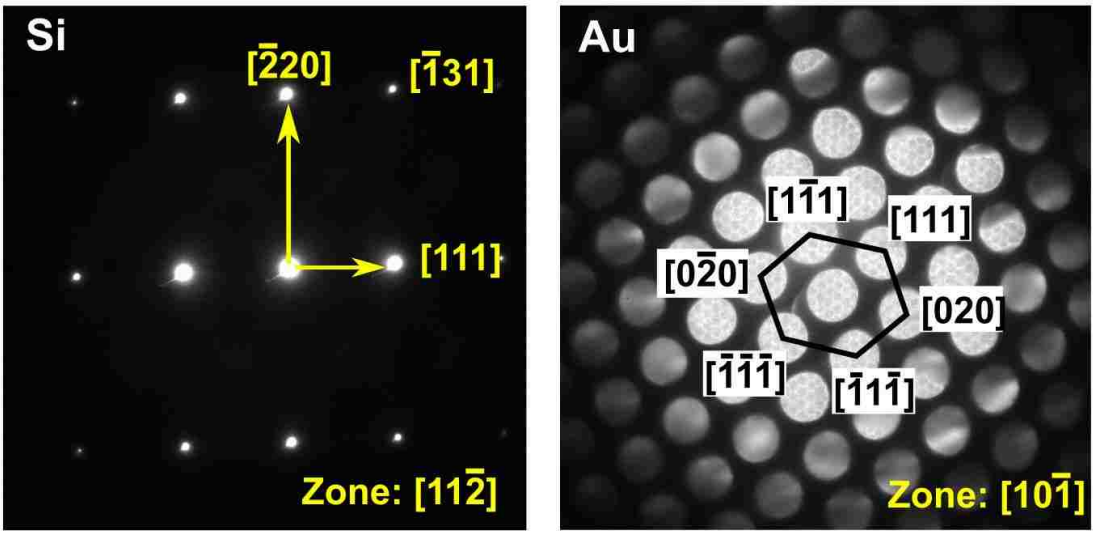

Figure S1. Electron diffraction pattern of as deposited Au on Si showing a spot pattern. Convergent beam diffraction on Au films because of lower thickness yields broader spots.

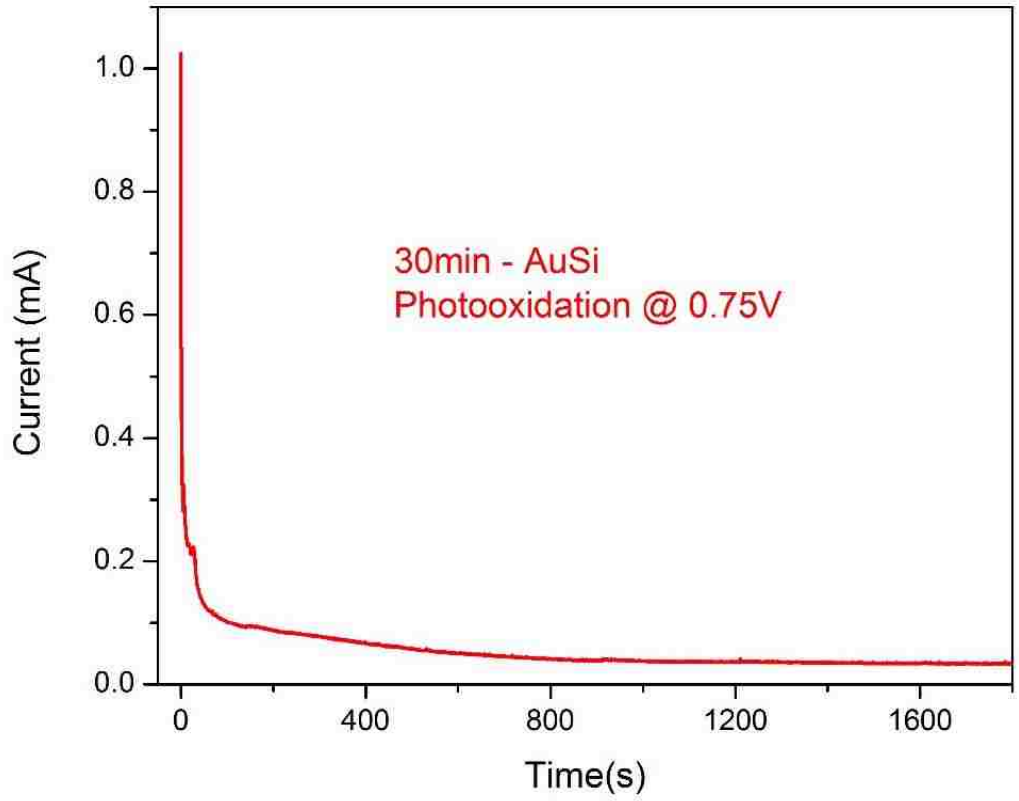

Figure S2. Photoelectrochemical oxidation of a 30 min Au on Si sample under irradiation of light at 0.75V versus Ag/AgCl in 0.5 M H_2SO_4 solution. The photocurrent gradually drops to near zero as the thickness of SiO_x increases and eventually flattens out around 1200-1600s.

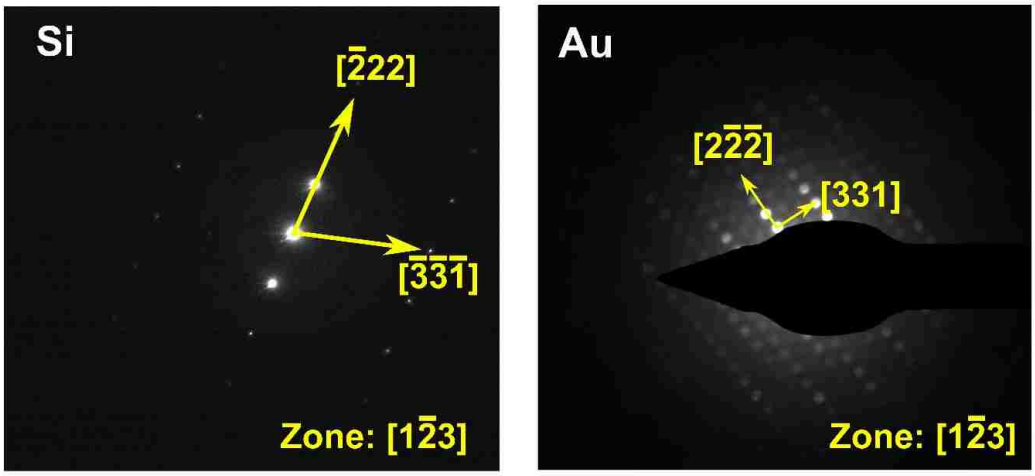

Figure S3. Electron diffraction pattern of Si and Au after photoelectrochemical oxidation at 0.75V in 0.5M H_2SO_4 solution for 30 min. A spot pattern shows that the Au is still epitaxial with Si. The rotation in directions are due to the difference in camera length used to capture the patterns.

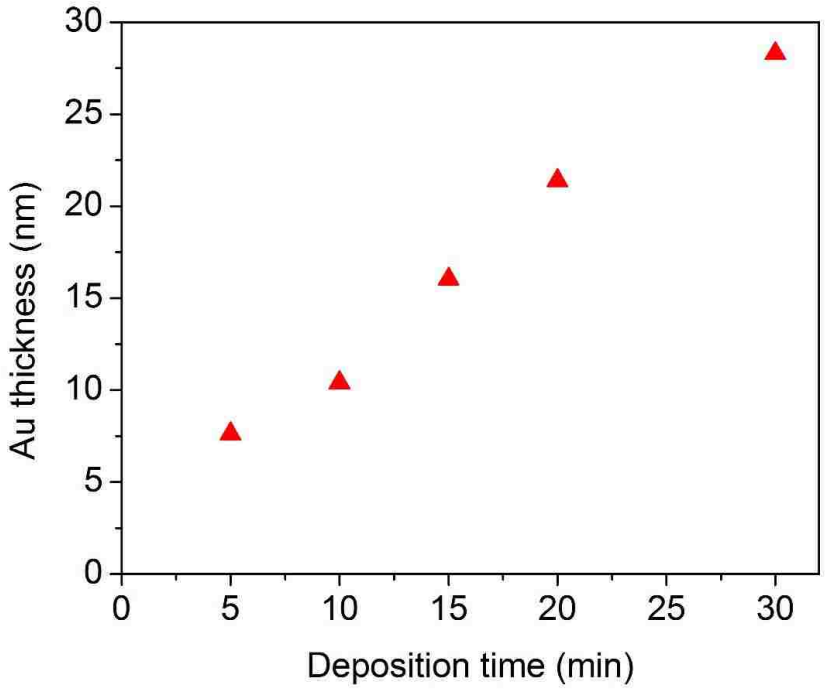

Figure S4. Thickness of Au on Si as a function of deposition time measured by Laue oscillations.

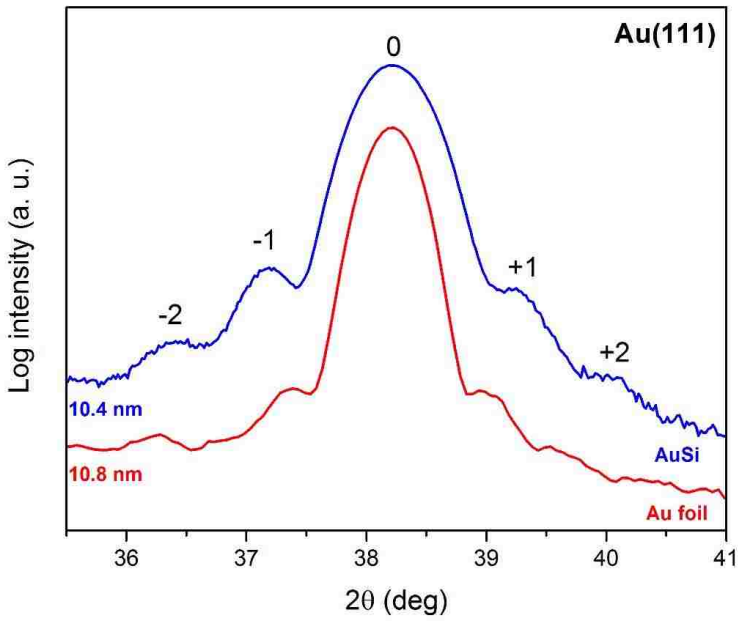

Figure S5. X-ray diffraction of a Au foil deposited for 10 min showing Laue oscillations around the (111) Brag peak. The calculated thickness using the satellite peaks is 11.8 nm, in close agreement with the thickness measured on an as deposited Au on Si sample (11 nm).

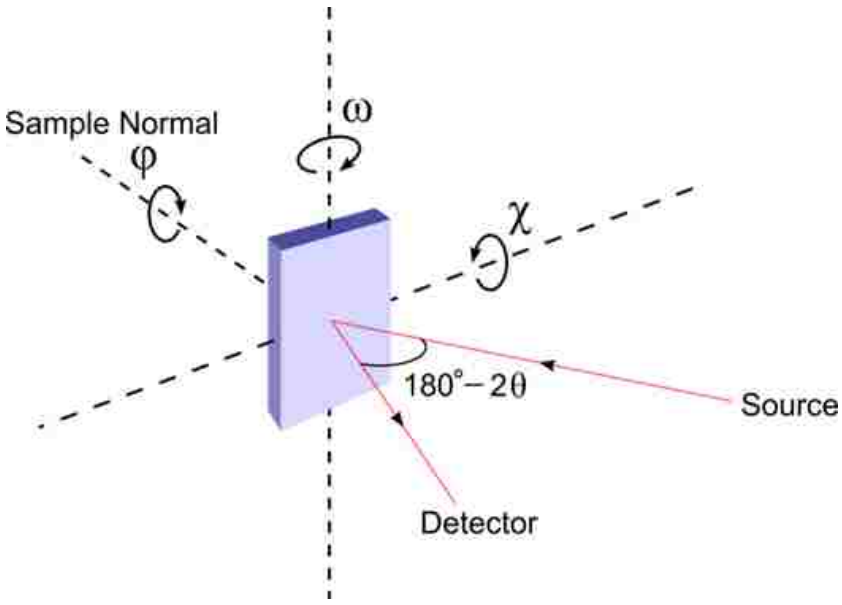

Figure S6. X-ray measurement geometry for pole figures.

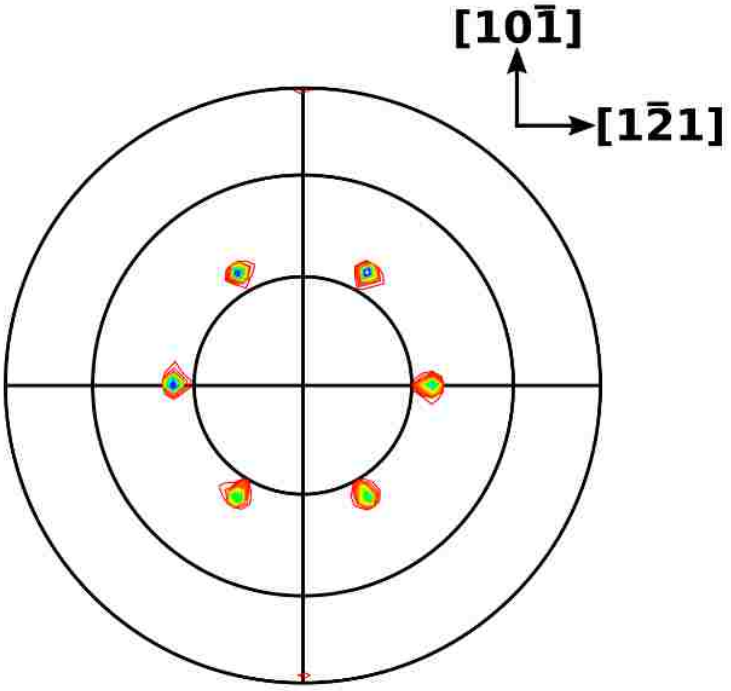

Figure S7. (220) pole figure of Au(111) on Si(111). Six spots corresponding to the parallel and anti-parallel domains at an expected tilt angle of 35.5^{o} rotated azimuthally by 60^{o}.

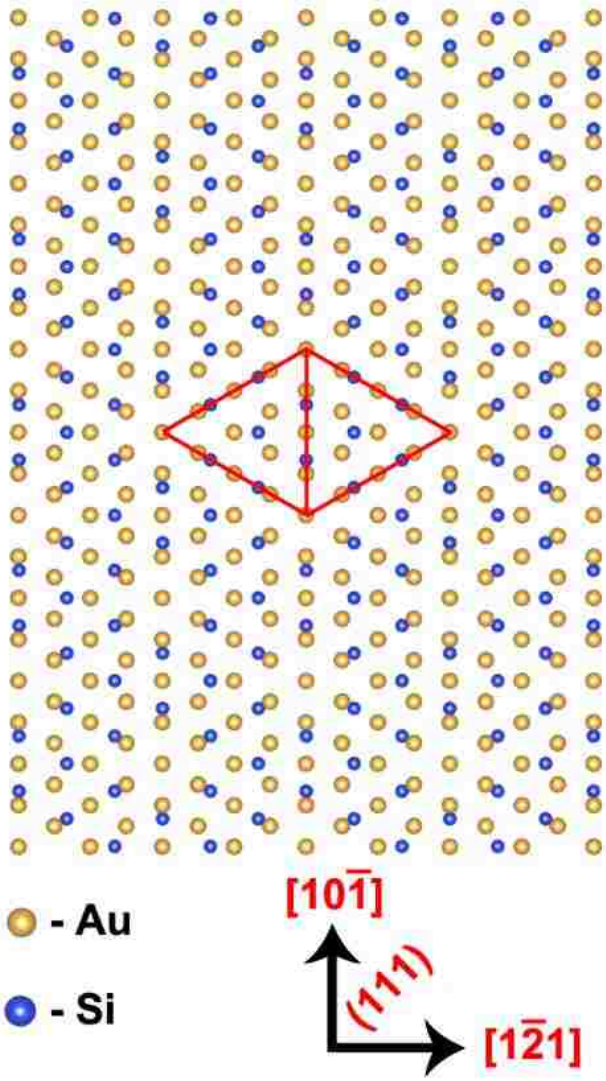

Figure S8. Interface model of Au(111) on Si(111) atoms. The coincidence lattice is shown in red lines forming two triangles rotated in-plane 180°. The lattice mismatch lowers from -24.9% for a $1d_{Au(hkl)}$ *x* $1d_{Si(hkl)}$ to +0.13% for the $4d_{Au(hkl)}$ *x* $3d_{Si(hkl)}$.

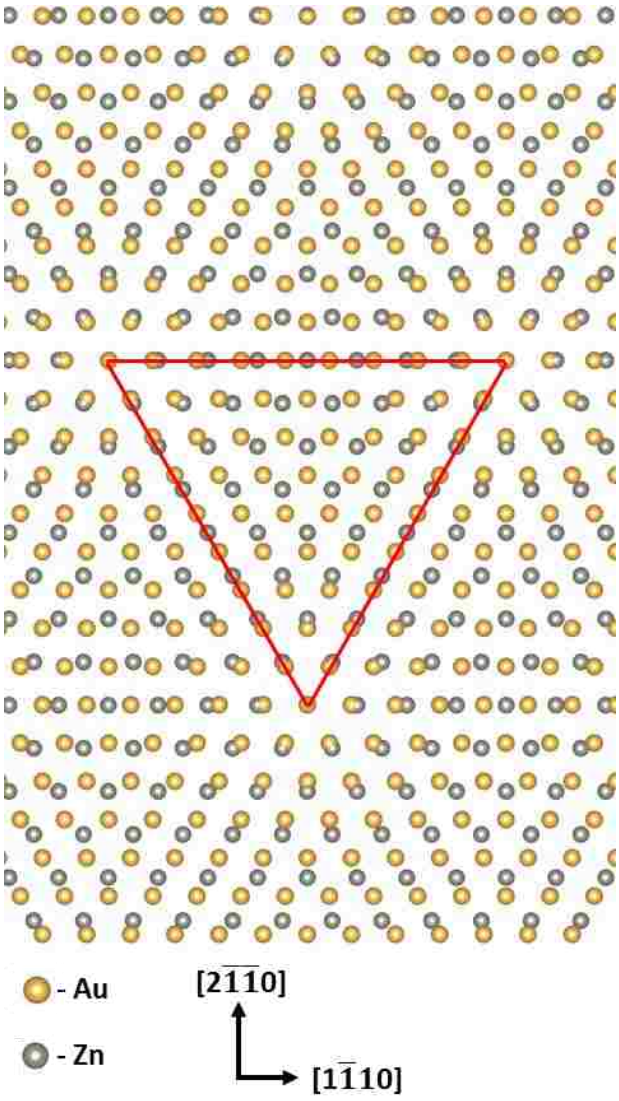

Figure S9. Interface model of ZnO(0002) on Au(111). The lattice mismatch lowers from +12.7% for a $1d_{Au(hkl)}$ x $1d_{Zn(hkl)}$ to +0.16% for the $9d_{Au(hkl)}$ x $8d_{Si(hkl)}$.

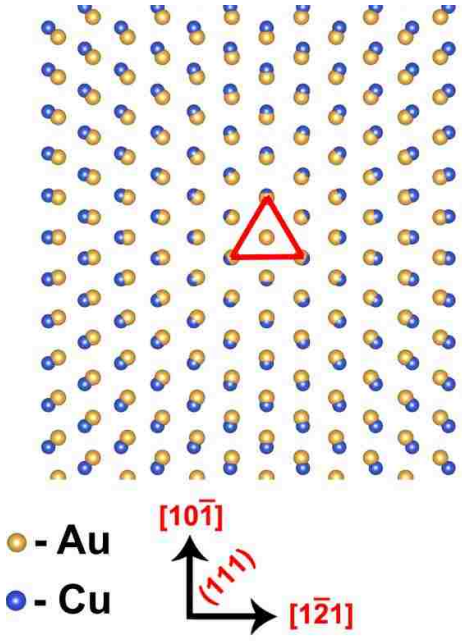

Figure S10. Interface model of $Cu_2O(111)$ on Au(111). The lattice mismatch for a $1d_{Au(hkl)} \times 1d_{Cu(hkl)}$ is +4.7%, which is low enough to form epitaxial deposits with moderate compressive in-plane strain and tensile out-of-plane strain.

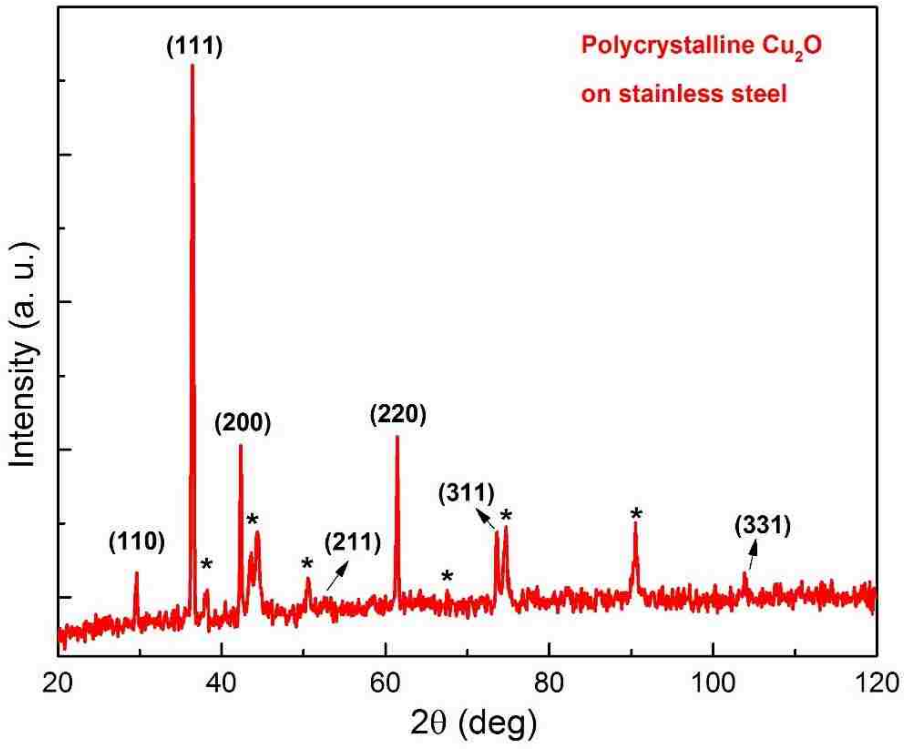

Figure S11. X-ray diffraction of pattern of polycrystalline Cu_2O electrodeposited on a stainless steel substrate for a charge density of 1.8 C/cm^2.

ACKNOWLEDGEMENT

The work was supported by the U.S. Department Of Energy, Office of Basic Sciences under Grant No. DE-FG02-08ER46518.

The authors thank Dr. Eric Bohannan for assistance in the XRD measurements.

AUTHOR INFORMATION

*Corresponding author. Tel.: +1 573 341 4383; E-mail address: jswitzer@mst.edu

REFERENCES

(1) Koza, 1. B. D. Gates, Flexible electronics. *Science* **2009**, 323, 1566-1567.

(2) J. C. Kenry, J. C. Yeo, C. T. Lim, Emerging flexible and wearable physical sensing platforms for healthcare and biomedical applications. *Microsyst. Nanoeng*. **2016**, 2, 16043.

(3) D. Akinwande, N. Petrone, J. Hone, Two-dimensional flexible nanoelectronics. *Nat. Commun.* **2014**, 5, 5678.

(4) J. A. Rogers, T. Someya, Y. Huang, Materials and mechanics for stretchable electronics. *Science* **2010**, 327, 1603-1607.

(5) W. Gao, S. Emaminejad, H. Y. Y. Nyein, S. Challa, K. Chen, A. Peck, H. M. Fahad, H. Ota, H. Shiraki, D. Kiriya, D.-H. Lien, G. A. Brooks, R.W. Davis, A. Javey, Fully integrated wearable sensor arrays for multiplexed in situ perspiration analysis. *Nature* **2016**, 529, 509-514.

(6) D. Shahrjerdi, S. W. Bedell, Extremely flexible nanoscale ultrathin body silicon integrated circuits on plastic. Nano Lett. 2013, 13, 315-320.

(7) J. Yoon, A. J. Baca, S.-I. Park, P. Elvikis, J. B. Geddes 3rd, L. Li, R. H. Kim, J. Xiao, S. Wang, T.-H. Kim, M. J. Motala, B. Y. Ahn, E. B. Duoss, J. A. Lewis, R. G. Nuzzo, P. M. Ferreira, Y. Huang, A. Rockett, J. A. Rogers, Ultrathin silicon solar microcells for semitransparent, mechanically flexible and microconcentrator module designs. Nat. Mater. 2008, 7, 907-915.

(8) S. Xu, Z. Yan, K.-I. Jang,W. Huang, H. Fu, J. Kim, Z.Wei, M. Flavin, J. McCracken, R. Wang, A. Badea, Y. Liu, D. Xiao, G. Zhou, J. Lee, H. U. Chung, H. Cheng, W. Ren, A. Banks, X. Li, U. Paik, R. G. Nuzzo, Y. Huang, Y. Zhang, J. A. Rogers, Assembly of micro/nanomaterials into complex, three-dimensional architectures by compressive buckling. Science 2015, 347, 154-159.

(9) T. Cheng, Y.-Z. Zhang, J.-D. Zhang, W.-Y. Lai, W. Huang, High-performance freestanding PEDOT:PSS electrodes for flexible and transparent all-solid-state supercapacitors. J. Mater. Chem. A 2016, 4, 10493-10499.

(10) D. M. Sun, M. Y. Timmermans, Y. Tian, A. G. Nasibulin, E. I. Kauppinen, S. Kishimoto, T. Mizutani, Y. Ohno, Flexible high-performance carbon nanotube integrated circuits. Nat. Nanotechnol. 2011, 6, 156-161.

(11) S. Bae, H. Kim, Y. Lee, X. Xu, J.-S. Park, Y. Zheng, J. Balakrishnan, T. Lei, H. R. Kim, Y. I. Song, Y.-J. Kim, K. S. Kim, B. Ozyilmaz, J.-H. Ahn, B. H. Hong, S. Iijima, Roll-to-roll production of 30-inch graphene films for transparent electrodes. Nat. Nanotechnol. 2010, 5, 574-578.

(12) W.-K. Kim, S. Lee, D. Hee Lee, I. Hee Park, J. Seong Bae, T. Woo Lee, J.-Y. Kim, J. Hun Park, Y. Chan Cho, C. Ryong Cho, S.-Y. Jeong, Cu mesh for flexible transparent conductive electrodes. Sci. Rep. 2015, 5, 10715.

(13) J. H. M. Maurer, L. Gonzalez-Garcia, B. Reiser, I. Kanelidis, T. Kraus, Templated self-assembly of ultrathin gold nanowires by nanoimprinting for transparent flexible electronics. Nano Lett. 2016, 16, 2921-2925.

(14) Y.-G. Bi, J. Feng, J.-H. Ji, Y. Chen, Y.-S. Liu, Y.-F. Li, Y.-F. Liu, X.-L. Zhang, H.-B. Sun, Ultrathin and ultrasmooth Au films as transparent electrodes in ITO-free organic light-emitting devices. Nanoscale 2016, 8, 10010-10015.

(15) B. O'Connor, C. Haughn, K.-H. An, K. P. Pipe, M. Shtein, Transparent and conductive electrodes based on unpatterned, thin metal films. Appl. Phys. Lett. 2008, 93, 223304.

(16) J. A. Koza, J. C. Hill, A. C. Demster, J. A. Switzer, Epitaxial electrodeposition of methylammonium lead iodide perovskites. Chem. Mater. 2016, 28, 399-405.

(17) J. W. Shin, A. Standley, E. Chason, Epitaxial electrodeposition of freestanding large area single crystal substrates. Appl. Phys. Lett. 2007, 90, 261909.

(18) S. Warren, P. Prod'homme, F. Maroun, P. Allongue, R. Cortes, C. Ferrero, T. L. Lee, B. C. C. Cowie, C. J. Walker, S. Ferrer, J. Zegenhagen, Electrochemical Au deposition on stepped Si(111)-H surfaces: 3D versus 2D growth studied by AFM and X-ray diffraction. Surf. Sci. 2009, 603, 1212-1220.

(19) P. Prod'homme, F. Maroun, R. Cortes, P. Allongue, Electrochemical growth of ultraflat Au(111) epitaxial buffer layers on H-Si(111). Appl. Phys. Lett. 2008, 93, 171901.

(20) J. A. Switzer, J. C. Hill, N. K. Mahenderkar, Y.-C. Liu, Nanometer-thick gold on silicon as a proxy for single-crystal gold for the electrodeposition of epitaxial cuprous oxide thin films. ACS Appl. Mater. Interfaces 2016, 8, 15828-15837.

(21) L. Jastrzebski, SOI by CVD: Epitaxial lateral overgrowth (ELO) process-review. J. Cryst. Growth 1983, 63, 493-526.

(22) G. B. Smith, G. A. Niklasson, J. S. E. M. Svensson, C. G. Granqvist, Noble-metalbased transparent infrared reflectors: Experiments and theoretical analyses for very thin gold films. J. Appl. Phys. 1986, 59, 571-581.

(23) D. N. Jarrett, L. Ward, Optical properties of discontinuous gold films. J. Phys. D 1976, 9, 1515-1527.

(24) M. Hövel, B. Gompf, M. Dressel, Dielectric properties of ultrathin metal films around the percolation threshold. Phys. Rev. B 2010, 81, 035402.

(25) O. S. Heavens, Optical properties of thin films. Rep. Prog. Phys. 1960, 23, 1.

(26) F. G. Gao, A. J. Bard, Solid-state organic light-emitting diodes based on tris(2,2"-bipyridine)ruthenium(II) complexes. J. Am. Chem. Soc. 2000, 122, 7426-7427.

(27) J. A. Broomhead, C. G. Young, P. Hood, Tris(2,2"-bipyridine)ruthenium(II) dichloride hexahydrate. Inorg. Synth. 2007, 28, 338-340.

(28) K. Sen, B. P. Tyagi, Diode quality factor in polycrystalline solar cells. J. Appl. Phys. 1984, 56, 1240-1241.

(29) S. Kumari, N. K. Arora, G. C. Jain, Grain size dependence of the photovoltaic properties of solar grade polysilicon. Sol. Energy Mater. 1981, 5, 383-390.

(30) R. J. Iwanowski, D. Trivich, Cu/Cu2O Schottky barrier solar cells prepared by multistep irradiation of a Cu2O substrate by H+ ions. Solar Cells 1985, 13, 253-264.

(31) W.Wu, X.Wen, Z. L.Wang, Taxel-addressable matrix of vertical-nanowire piezotronics transistors for active and adaptive tactile imaging. Science 2013, 340, 952-957.

(32) C. Wang, R. Bao, K. Zhao, T. Zhang, L. Dong, C. Pan, Enhanced emission intensity of vertical aligned flexible ZnO nanowire/p-polymer hybridized LED array by piezophototronic effect. Nano Energy 2015, 14, 364-371.

(33) P. Poizot, C.-J. Hung, M. P. Nikiforov, E. W. Bohannan, J. A. Switzer, An electrochemical method for CuO thin film deposition from aqueous solution. Electrochem. Solid-State Lett. 2003, 6, C21-C25.

(34) S. Yazdanparast, J. A. Koza, J. A. Switzer, Copper nanofilament formation during unipolar resistance switching of electrodeposited cuprous oxide. Chem. Mater. 2015, 27, 5974-5981.

(35) R. Liu, A. A. Vertegel, E. W. Bohannan, T. A. Sorenson, J. A. Switzer, Epitaxial electrodeposition of zinc oxide nanopillars on single-crystal gold. Chem. Mater. 2001, 13, 508-512.

(36) M. Skompska, K. Zarebska, Electrodeposition of ZnO nanorod arrays on transparent conducting substrates-a review. Electrochim. Acta 2014, 127, 467-488.

III. ELECTRODEPOSITION OF NANOMETER-THICK EPITAXIAL FILMS OF SILVER ONTO SINGLE-CRYSTAL SILICON WAFERS

*Qingzhi Chen and Jay A. Switzer**

Missouri University of Science and Technology, Department of Chemistry and Graduate Center for Materials Research, Rolla, MO 65409-1170, USA

ABSTRACT

Silver films were deposited epitaxially for the first time onto low-index, single-crystal silicon wafers through an electrochemical method in an aqueous silver acetate bath. A negative potential of -2.34 V vs. Hg/Hg_2SO_4 was used for both pre-polarization and during the deposition to avoid Si oxidation. The epitaxy of Ag films on Si(111), (110) and (100) was characterized by X-ray diffraction symmetric scans and pole figures. The Ag films showed [111], [110] and [100] out-of-plane orientations, respectively, with in-plane order determined by the Si substrates. Interface models consistent with the observed orientations invoke coincident site lattices (CSLs), in which four unit meshes of Ag coincide with three unit meshes of Si. These CSLs reduce the lattice mismatch from -24.9% to +0.13%. A thickness of about 10 nm was obtained for Ag deposited for ten minutes. A comparison of silver acetate electrolyte and cyanide electrolyte was also performed, showing advantages of the acetate bath over the cyanide bath for growth of epitaxial films of Ag on Si surfaces.

1. INTRODUCTION

Silver (Ag), a coinage metal possessing the highest electrical conductivity, has been one of the most important metals for the electronic industry for decades. Beyond that, its ability to from a Schottky barrier with n-type silicon qualifies it as a potential candidate for electrical or photovoltaic devices, and its excellent optical properties make it ideal for plasmonic devices and surface enhanced Raman spectroscopy (SERS) substrates [1–5]. However, the use of Ag deposited on other substrates taking advantages of its optical properties requires a major characteristic: epitaxy (or single crystallinity), since the grain boundaries in a polycrystalline Ag film cause extra scattering and absorption losses [2,5]. The frequently used techniques for Ag deposition such as vacuum evaporation and chemical vapor deposition (CVD) often give polycrystalline Ag [6,7]. Although there have been examples of epitaxial growth of Ag on Si through magnetron sputtering and molecular beam epitaxy (MBE) [8–13], these techniques require high vacuum and the MBE equipment is expensive, with limited access to most researchers. Inspired by Allongue's work in epitaxial electrodeposition of Au on Si [14], we herein introduce a method that directly electrodeposits Ag epitaxially on three different orientations of Si substrates using a simple aqueous electrolyte solution. We have previously shown that Au deposited on Si with different orientations can be used as a low-cost proxy for single-crystal Au, and as a photoanode for photoelectrochemical regenerative cells [15,16], we have also shown that Cu deposited on Si(100) could serve as a proxy for single-crystal Cu(100) as well[17]. Ag epitaxially deposited on Si could have a broader impact due to its lower cost than Au, and because Ag exhibits a wider range of applications from plasmonic devices, to surface

catalysts, to highly selective absorbers/emitters [18]. We also compare the morphology and epitaxy of films deposited from standard cyanide baths[18] with those deposited from the simple acetate bath.

2. EXPERIMENTAL

2.1. Si WAFER ETCHING PROCESS AND Ag DEPOSITION

N-type Si wafers with [111], [110] and [100] orientations were used as substrates for Ag deposition. The resistivity of the Si wafers was approximately 1 Ω·cm. The wafers were purchased from Virginia Semiconductor Inc. and were hydrogen-terminated before use. Wafers were etched in 5% HF acid for 3 minutes to remove the native oxide layer, and then soaked in 90 °C DI water for 15 min to form an SiO_x layer, then etched again with 5% HF acid for 30 s. Gallium-indium eutectic was applied to the back of the Si wafers to form an ohmic contact, followed by silver wire and silver print II (GC electronics) as a back contact. Silicone sealant or melted Apiezon Type W wax was used to insulate the back and edges of the Si substrates. The Ag films were directly electrodeposited onto the Si substrate using a "hot-wire" method. That is, a prepolarized potential was applied to the electrode before the immersion of the sample into the solution to prevent the oxidation of Si in the aqueous environment. The plating solution contained 0.1 mM AgOAc, 1 mM KOAc, 1 mM H_2SO_4 and 0.1 M K_2SO_4, where 90 ml DI water was added to 10 ml stock solution containing 1 mM AgOAc, 10 mM KOAc and 10 mM H_2SO_4. The pH of the solution was 3.6. The polarization curves of a Au electrode in the electroplating solution were obtained by performing linear sweep voltammetry (LSV) scans from the open circuit

potential (OCP) towards negative potentials at a scan rate of 10 $mV \cdot s^{-1}$. A potential of -2.34 V vs. Hg/Hg_2SO_4 electrode was used for Ag prepolarization and deposition at room temperature. The cyanide plating solution was made by dissolving 2.4 mM AgCl in a solution containing 8.5 mM KCN, followed by adding 0.1 M K_2CO_3 as a supporting electrolyte. The pH of the solution was 11. A prepolarized potential of -1.9 V vs. Ag/AgCl electrode was used for Ag deposition in the cyanide bath at room temperature. Note that the AgCl reference electrode was not used in the acetate bath to avoid precipitation of AgCl. Both EG&G Model 273A and Autolab 30 potentiostats were used for Ag deposition and measurements.

2.2. X-RAY DIFFRACTION MEASUREMENTS AND SEM MEASUREMENTS

The XRD measurements were done using a Philips X'Pert Materials Research diffractometer with a Cu Kα_1 radiation source. A crossed slit collimator with 2 mm divergence slit and 2 mm mask with a Ni filter and a 0.27° parallel plate collimator were used for X-ray pole figure measurements. The SEM images were obtained using a FEI Helios Nanolab Dualbeam microscope with accelerating voltages ranged from 5 to 15 kV.

3. RESULTS AND DISCUSSION

The LSV curve of a Au-coated glass electrode in the stirred AgOAc plating solution towards negative potentials shows mainly four regions, as shown in Figure 1. Region I is the Ag(I) reduction step, where Ag metal starts depositing at about -0.1 V vs. Hg/Hg_2SO_4, and reaches the limiting current of about 0.04 mA cm^{-2} due to the forced convection. The

second region is attributed to oxygen reduction reaction (ORR), and the regions III and IV correspond to proton reduction and water reduction reactions, respectively. The deposition of Ag on Si wafers was conducted by applying a static potential of -2.34 V, where a Faradic efficiency is estimated to be 0.22% by comparing the limiting current density at region I to the current observed at the deposition potential (-2.34 V). The large negative potential was used to avoid Si oxidation and to evolve hydrogen, which has been reported to contribute to a more uniform nucleation and more smooth growth for electrodeposited metals [14,20-21]. The applied potential corresponds to a 2.26 V overpotential for the reduction of Ag(I) to Ag, a 1.49 V overpotential for H_2 evolution, and a 0.62 V overpotential for the reduction of SiO_2 to Si.

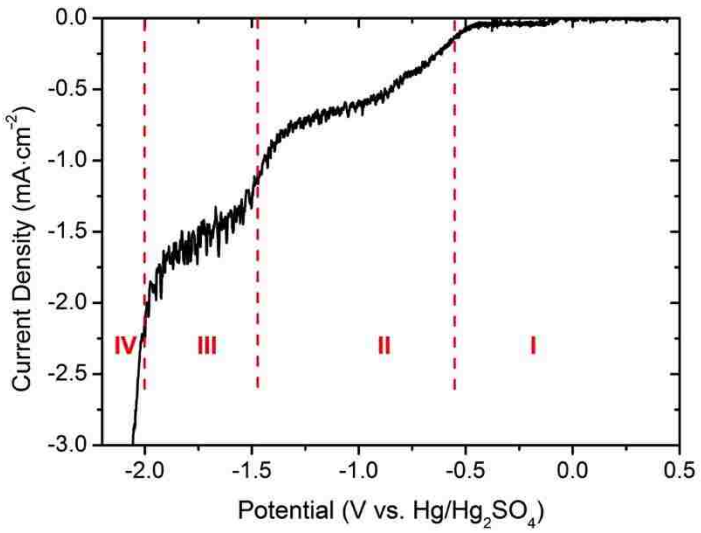

Figure 1. Linear sweep voltammogram of a Au electrode in the stirred acetate-based Ag plating solution at a scan rate of 10 mV s^{-1}.

The SEM images of Ag deposited on Si(111) at different deposition times offer a snapshot of the Ag growth progress. As shown in Figure 2 (a), Ag deposited for 1 min

exhibits 3D island growth. The 3D island growth is followed by 2D growth producing a fractal pattern (Figure 2B). After 10 minutes of deposition the Ag film has coalesced into a dense film (Figure 2C) covered with larger Ag islands with sizes ranging from 20 nm to several hundred nm. As can be seen in Figure 2, the films deposited for short times have a

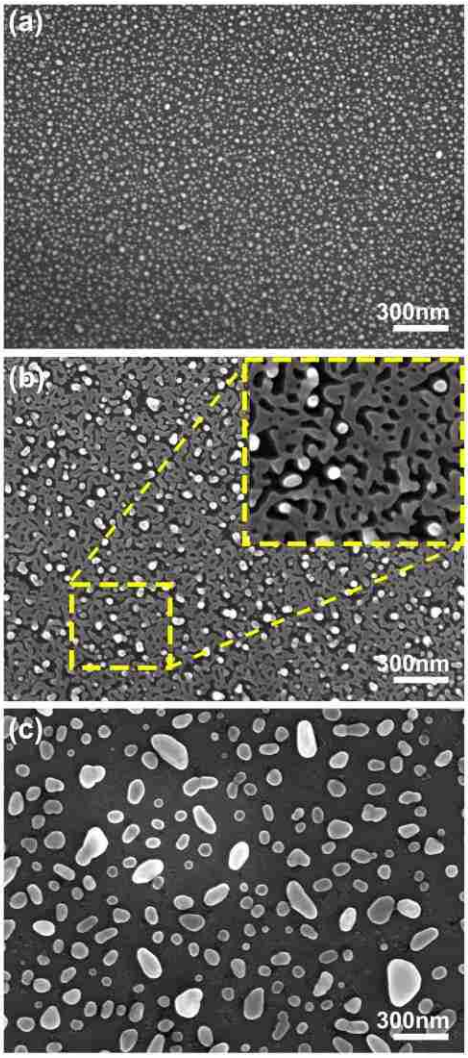

Figure 2. SEM plan-view images of silver thin films deposited from the acetate bath on Si(111) for different deposition times. (a) 1 min deposition, (b) 5 min deposition and (c) 10 min deposition. The higher magnification inset in (b) shows the fractal structure of the Ag.

larger density of islands than films deposited for longer times. This could be due to loss of islands due to poor Ag/Si adhesion, or to the merging of small islands to produce larger islands. More work is needed to determine the reason for the lower density of islands on the films deposited for longer times.

To determine the epitaxial relationships between the electrodeposited Ag and the Si substrate, XRD symmetric 2-theta scans and pole figure scans were obtained. Figure 3 (a) shows the 2-theta scan of Ag deposited for 10 min on Si (111). As shown in the plot, only Ag (111) and (222) peaks were observed. This indicates a strong out-of-plane orientation. A detailed slow-rate scan of the Ag (111) peak shows two satellite peaks (interference fringes) from Laue oscillations. A thickness of 10.1 nm was calculated from the position of the satellite peaks (see the supplementary information for details). The (222) d-spacing was 0.11783 nm, compared with 0.11774 nm for bulk Ag. Hence the Ag d-spacing is larger than expected out-of-plane, indicative of uniform in-plane compressive strain. The in-plane orientation of Ag on Si is revealed by X-ray pole figures. In Figure 3 (c), the Si (220) pole figure shows three spots separated azimuthally by 120°at a tilt angle of 35.5°, consistent with the (220) crystalline plane projection in a single crystalline Si(111). However, in Figure 3(d), the Ag (220) pole figure shows six spots separated azimuthally by 60° at a tilt angle of 35.5°. The additional three spots can be interpreted as coming from 180° rotational twins of Ag. This twinning phenomenon occurs also during the deposition of other fcc metals such as Au on Si [15]. The full width at half maximum (fwhm) in the azimuthal angle in the pole figure was 4.85º. The epitaxial relationships consistent with these pole figures are Ag(111)[10-1]||Si(111)[10-1] and Ag(111)[-101]||Si(111)[10-1].

Silver deposition on Si wafers with other orientations using the same electrolyte also produced epitaxial films. Figure 4 (a) shows the 2 theta scan of Ag deposited for 5 min on the Si(110) surface. Similar to the Ag film on Si(111), the silver deposited on Si (110)

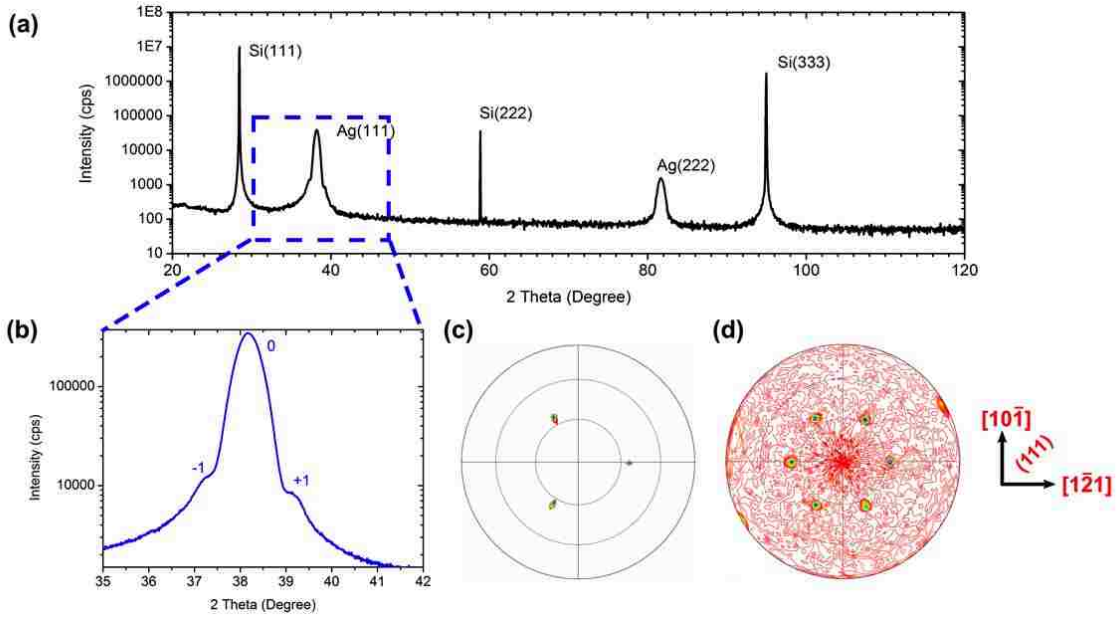

Figure 3. X-ray diffraction of Ag deposited on Si(111) from the acetate bath. (a) 2 theta gonio scan, showing {111} out-of-plane growth of the silver film, (b) detailed scan of silver (111) peak, showing ±1 orders of Laue oscillation peaks, (c) the Si (220) pole figure, and (d) Ag (220) pole figure showing in-plane orientations.

also shows a (220) peak only, which follows the out-of-plane orientation of the silicon substrate. The (220) d-spacing was 0.14445 nm, compared with 0.14420 nm for bulk Ag, consistent again with uniform in-plane compression. The Si (111) pole figure in Figure 4 (b) shows two spots separated azimuthally by 180° at a tilt angle of 35.0° as expected, while the silver (111) pole figure in Figure 5 (b) also shows two major spots at the same

tilt angle. However, there are four additional spots at a tilt angle of 57.0° and two more spots at 75.0°. These extra spots come from the (411) twins that were deposited simultaneously during the (110) growth of the Ag film. A detailed discussion about the twinning phenomenon on Si(110) can be found in the supplementary materials. The fwhm in the azimuthal angle in the pole figures was 7.34°. The deposition was also performed for 5 min on the Si(100) surface. The 2 theta scan in Figure 5 (a) of the Ag deposited on Si(100) only shows a minor (200) peak, indicating a slower growth rate under the experimental condition compared to that of the Si(110) surface. The (200) d-spacing was 0.20414 nm, compared with 0.20390 nm for bulk Ag, consistent again with uniform in-plane compressive strain. Although little material was obtained, the pole figures still show an in-plane ordered growth of silver on Si(100). Figure 5 (b) shows the Si (111) pole figure, presenting four spots separated evenly at a tilt angle of 54.7° consistent with the tilt angle between the [111] and [100] directions in the cubic crystal system. In Figure 5 (c), a Ag (111) pole figure also shows four spots at the same position as those in the Si (111) pole figure. The fwhm in the aximuthal angle in the pole figure is 7.67°. The epitaxial relationships with Ag on Si (110) and (100) are Ag(110)[1-10]||Si(110)[1-10] and Ag(100)[011]|| Si(100)[011].

Interface models can shed light on the Ag epitaxial growth on Si. The original $1d_{Ag}$ x $1d_{Si}$ lattice generates a mismatch of -24.9%, which is typically too high for epitaxial growth. However, the formation of coincident site lattices (CSL) reduces the Ag-Si mismatch to 0.13%. As shown in the interfacial models in Figure 6, the CSL is made up by 4 unit meshes of Ag lattice coinciding with 3 unit meshes of Si lattice, and is represented

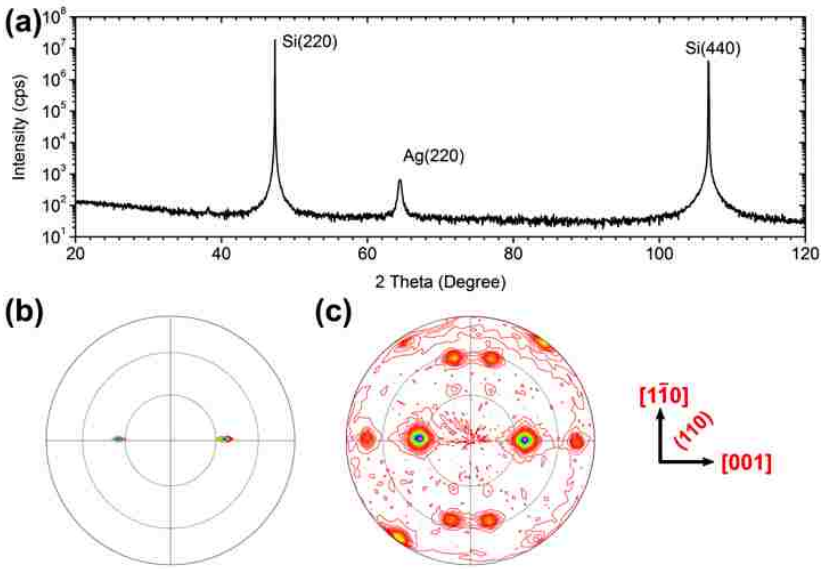

Figure 4. X-ray diffraction of Ag deposited on Si(110) from the acetate bath. (a) 2 theta gonio scan, showing only {110} out-of-plane growth of the Ag film, (b) Si (111) pole figure and, (c) the Ag (111) pole figure with in-plane orientations.

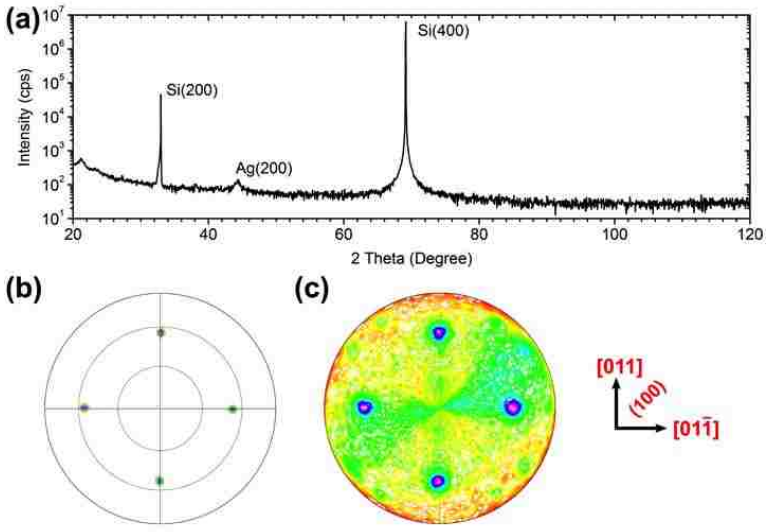

Figure 5. X-ray diffraction of Ag deposited on Si(100) from the acetate bath. (a) 2 theta gonio scan, showing a low-intensity (200) peak of the Ag film, (b) the Si (111) pole figure and, (c) the Ag (111) pole figure with the in-plane orientations.

by the red triangles/rectangles. These CSLs help reduce the strains so that the Ag film deposited on Si will not shrink, flake off or be forced to conduct an in-plane rotation to avoid the huge mismatch like Cu on Si [17,22-23]. Note that the same CSL was invoked to explain the epitaxial electrodeposition of Au on Si(111) by Munford *et al.*[24] and the electron beam evaporation of epitaxial Ag nanoclusters on Si by Li and Zuo [25] . Das and co-workers also developed this CSL using first principle simulations to reduce the effective strain [26]. Note that our X-ray results also showed that the films had slightly larger out-of-plane d-spacings than bulk Ag, consistent with the in-plane compressive stress predicted by the CSL.

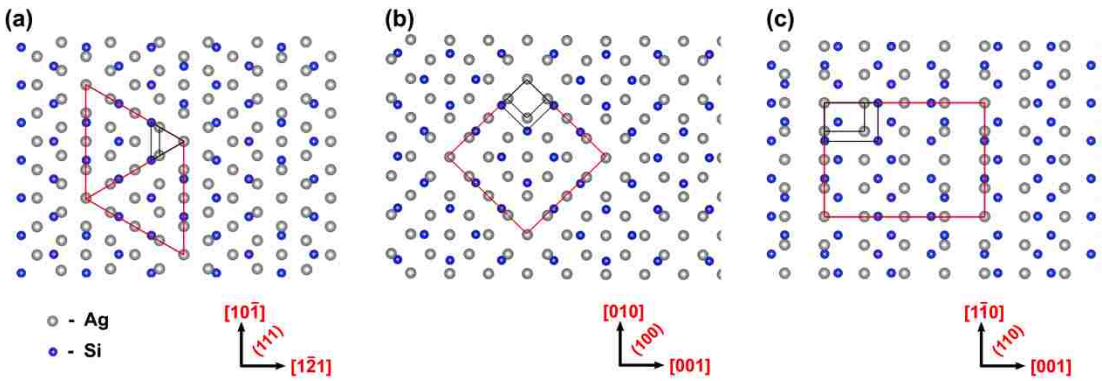

Figure 6. Interfacial models of Ag on Si showing the formation of the Ag-Si coincident site lattices (CSL) in which 4 unit meshes of Ag coincide with 3 unit meshes of Si. (a) Ag on Si(111), (b) Ag on Si(100) and (c) Ag on Si(110). The red triangles/rectangles represent to the CSLs and the black ones represent to the large-mismatch 1 x 1 lattices.

To compare the method above to the conventional cyanide bath plating method and as an attempt of acquiring smoother Ag deposits, a cyanide plating electrolyte was also made and Ag films were deposited on the three different orientations of Si. A LSV study

of a Au electrode in the cyanide bath was also conducted and is shown in Figure S1 in the supplementary materials. The LSV curve shows that the Ag starts to deposit at a potential of -0.4 V vs. Ag/AgCl. The deposition potential was chosen to be -1.9V, which 1.53 V negative of the silver-cyanide complex reduction potential, to avoid potential Si oxidation as well. The SEM was also used to characterize the surface morphology of the deposited silver films. In Figure 7 (a), the 10 s deposited Ag grows mainly as particles and has not achieved coalescence on the Si surface. It grows into a dense film after one minute, as shown in Figure 7(b). The increased growth rate compared to the silver films deposited from acetate bath could be attributed to the higher concentration (2.4 mM vs. 0.1 mM for the acetate bath). Also the grain size of the thicker silver film from the cyanide bath is more uniform compared to that from the acetate bath, which indicates that it is more likely to obtain compact and uniform films in the cyanide bath for thicker deposits. The X-ray diffraction shows that the Ag film deposited on Si(111) in the cyanide bath is epitaxial with the Si as well. As shown in Figure 7(c), the 2 theta scan gives only the {111} family of peaks for the silver deposit. Furthermore in Figure 7(d) and (e), the pole figures show the same patterns as those deposited in the acetate bath, giving an epitaxial relationships of Ag(111)[10-1]||Si(111)[10-1] and Ag(111)[-101]|| Si(111)[10-1]. The fwhm in the azimuthal angle in the pole figures was 7.70^{o}. However, the epitaxial growth of Ag on Si(110) and (100) surface using the cyanide bath was not successful. The 2 theta scans of silver deposits on these two silicon surfaces showed diffraction peaks from multiple crystalline orientations (see details in Figure S2 and S3 in the supplementary materials). This could limit the use of the cyanide bath for the epitaxial growth of Ag on Si (110) and (100).

Hence, the cyanide plating bath works well for the electrodeposition of epitaxial films of Ag on Si(111), but it produces polycrystalline films on Si(100) and Si(110). One possible explanation for the polycrystalline growth on Si(100) and Si(110) is the propensity of Ag to grow with a [111] orientation from the cyanide bath. The Ag will grow with a [111] fiber texture even on amorphous or polycrystalline substrates. This kinetically-controlled growth in the [111] direction is apparently stronger than the thermodynamically-controlled template effect of the substrates to grow epitaxial films. Figure S4 shows XRD

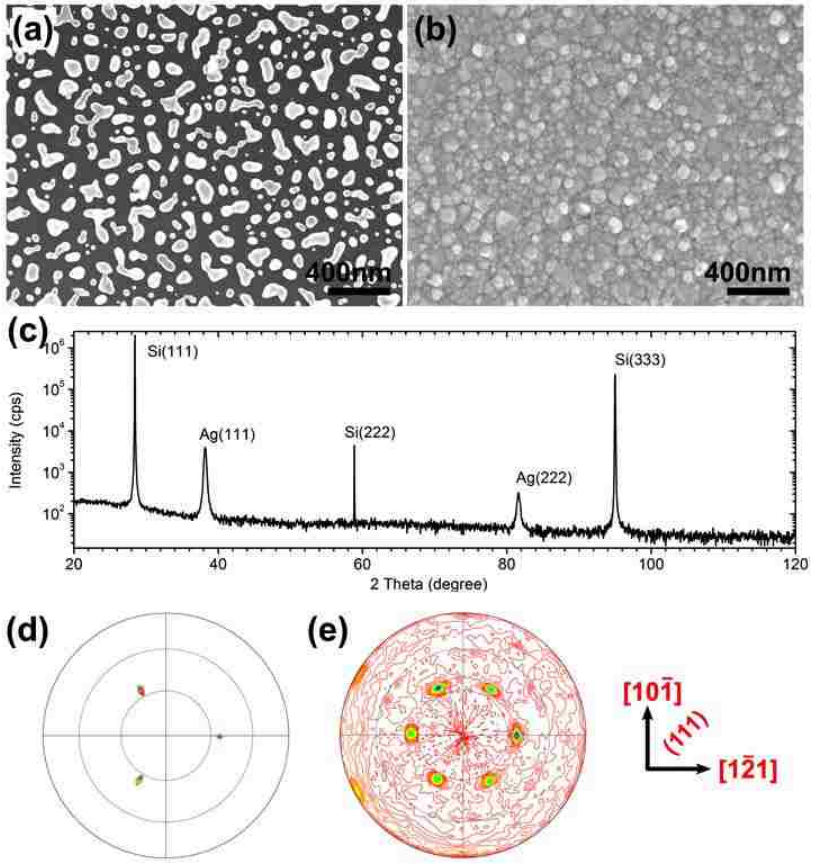

Figure 7. SEM images and the X-ray diffraction of Ag deposited Si(111) from the cyanide bath. (a) SEM image for 10 seconds silver deposition, (b) SEM image for 1 minute silver deposition, (c) the 2 theta gonio scan, showing only {111} out-of-plane growth of the silver film, (d) the Si (220) pole figure and (e) the Ag (220) pole figure with the in-plane orientations.

2 theta scans for thicker Ag films grown for 3 minutes on Si(100) and Si(110). In both cases, the Ag(111) peak is more intense than with the Ag(200) or Ag(220) peaks, suggesting kinetically-controlled fiber growth.

4. CONCLUSIONS

We show in this work that nm-thick Ag films can be electrochemically deposited epitaxially onto single-crystal Si. A key feature of the electrodeposition that allows for epitaxial growth is the use of a very negative pre-polarization and growth potential to prevent the oxidation of Si to amorphous SiO_x. Films deposited from the acetate bath follow the out-of-plane and in-plane orientation of Si(111), Si(110), and Si(100) wafers, whereas films deposited from the cyanide bath grow epitaxially on Si(111), but deposit as polycrystalline films on Si(100) and Si(110). This is attributed to the propensity of the Ag to grow with a [111] fiber texture from the cyanide bath. The large mismatch of -24.9% of the Ag/Si system is reduced to +0.13% by the formation of coincident site lattices (CSLs). In these CSLs, four unit meshes of Ag coincide with three unit meshes of Si. The compressive residual strain observed in the X-ray diffraction patterns is consistent with the CSL. The Ag films could serve as proxies for Ag single crystals for the epitaxial growth of other materials. They could also be used as catalysts to study the different activities of various crystal planes of Ag. Low coverage deposits have a fractal geometry, which may yield large plasmonic responses.

SUPPORTING INFORMATION

ELECTRODEPOSITION OF NANOMETER-THICK EPITAXIAL FILMS OF SILVER ONTO SINGLE-CRYSTAL SILICON WAFERS

*Qingzhi Chen and Jay A. Switzer**

Missouri University of Science & Technology, Department of Chemistry and Graduate Center for Materials Research, Rolla, MO 65409-1170, USA.

Correspondence to: jswitzer@mst.edu

1. Laue oscillation calculations for Ag on Si(111). The film thickness can be determined by the satellite peak positions from the Laue oscillation using the equation below:

$$t = \frac{(L_2 - L_1)\lambda}{2(\sin\theta_1 - \sin\theta_2)} \quad (1)$$

where t is the film thickness, L is the satellite peak order, λ is the X-ray wavelength, and θ is the satellite angle [1].

2. Twinning relationship analysis for Ag on Si(110). The (411) twin observed in the (110) silver on silicon could be described either as a 180° rotational twin along the [111] direction or a reflection twin. This could be written as the transformation: [1]

$$(PQR) = T_{(111)}(pqr) \quad (2)$$

where (*PQR*) is a column matrix for the lattice plane after the twinning, described by the twinning matrix $T_{(111)}$ which happens on the (111) slip plane. (*pqr*) is the original crystalline plan. For face-centered cubic (fcc) system such as Ag in this case, the twin matrix can be expressed as

$$T_{(111)} = \frac{1}{3}\begin{pmatrix} -1 & 2 & 2 \\ 2 & -1 & 2 \\ 2 & 2 & -1 \end{pmatrix} \tag{3}$$

Thus, by applying this matrix on (110) plane using Equation (2), the twinned plan is (114).

SUPPLEMENTARY FIGURES

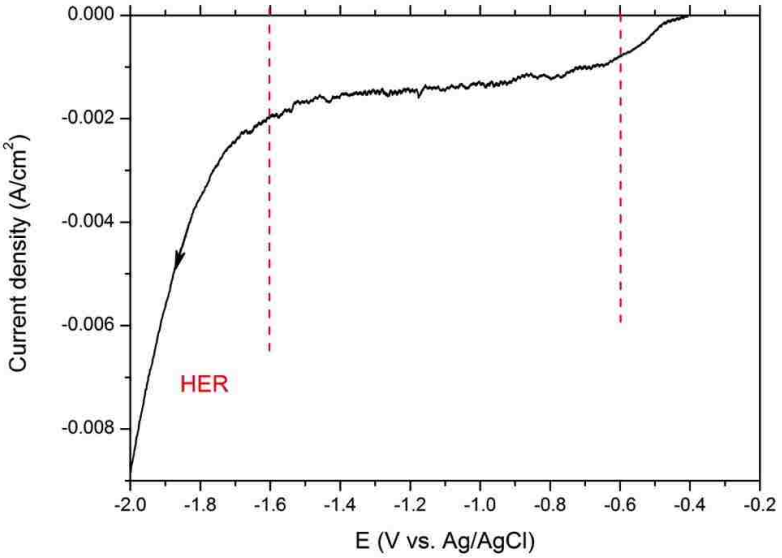

Figure S1. LSV curve of the Au electrode in the stirred cyanide bath showing the Ag deposition range and the hydrogen evolution range. The arrow in the plot indicates the scan direction. The scan rate was 10 mV s^{-1}.

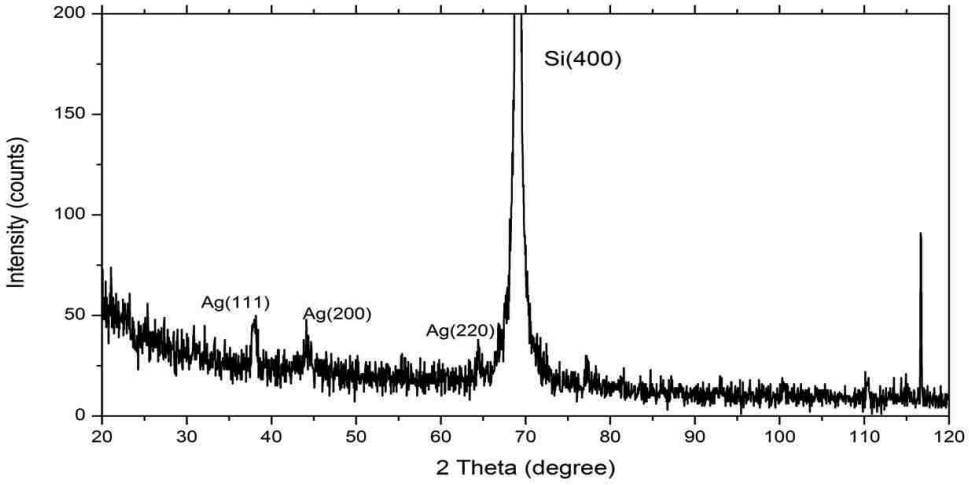

Figure S2. The 2 theta scan of the Ag film deposited for 1 min on Si(100) in the cyanide bath; showing Ag (111), (200) and (220) crystalline planes.

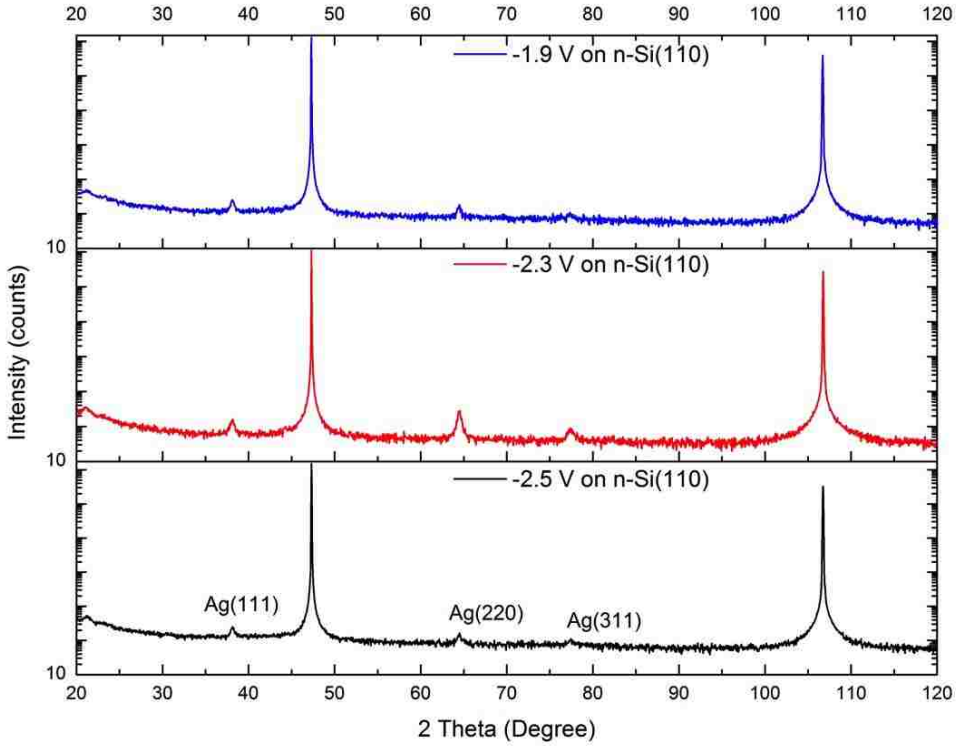

Figure S3. The 2 theta scan of the Ag film deposited for 1 min on Si(110) in the cyanide bath; showing Ag (111), (200) and (220) crystalline planes. Note that three different potentials were applied when depositing and that all three films are disoriented.

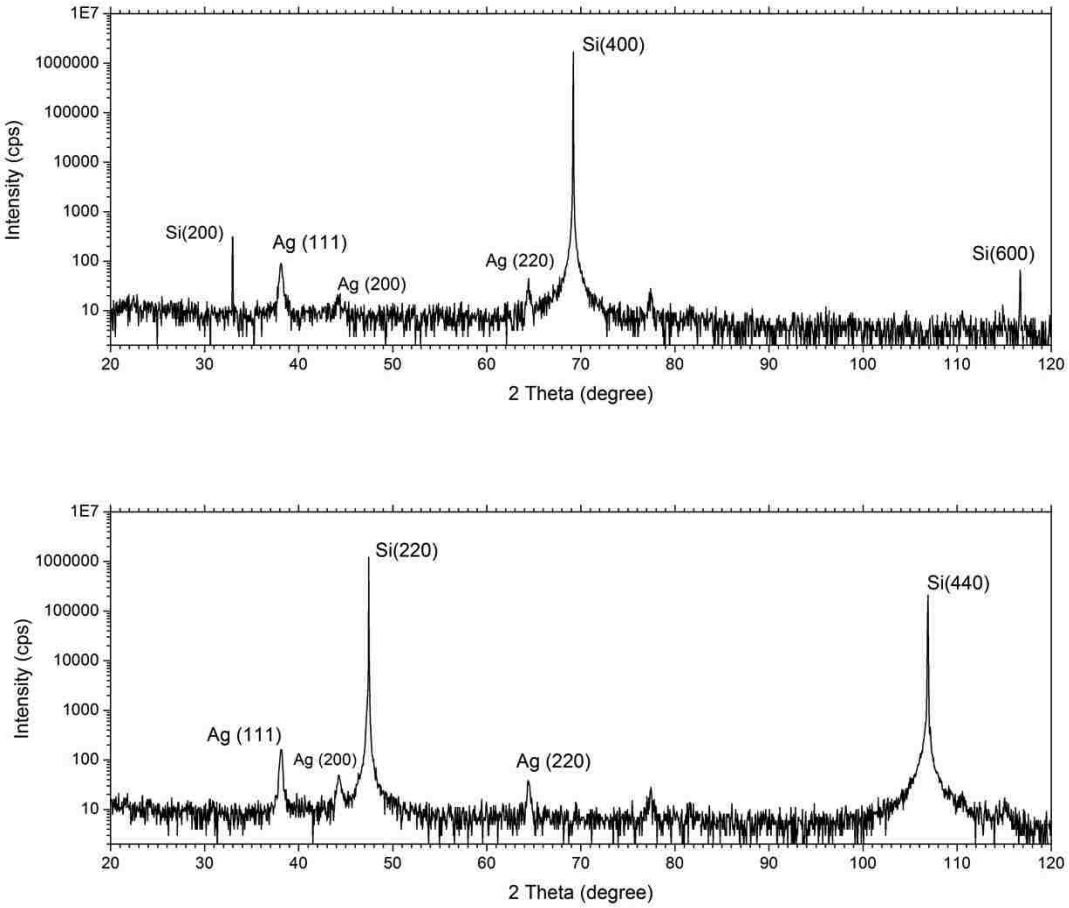

Figure S4. The 2 theta scan of the Ag film deposited for 3 min at -1.9 V vs. Ag/AgCl on Si(100) and Si(110) in the cyanide bath; showing increased intensity of Ag (111) peaks in both cases.

REFERENCES

(1) J. A. Switzer, J. C. Hill, N. K. Mahenderkar and Y. C. Liu, *ACS Appl. Mater. Interfaces*, 2016, **8**, 15828–15837

CONFLICT OF INTEREST

There are no conflicts to declare.

ACKNOWLEDGEMENTS

This material is based upon work supported by the U.S. Department of Energy, Office of Basic Energy Sciences, Division of Materials Sciences and Engineering, under Grant No. DE-FG02-08ER46518.

REFERENCES

(1) R. Balsano, A. Matsubayashi and V. P. Labella, *AIP Adv.*, 2013, **3**, 112110.

(2) L. Sun, C. Zhang, C. Y. Wang, P. H. Su, M. Zhang, S. Gwo, C. K. Shih, X. Li and Y. Wu, *Sci. Rep.*, 2017, **7**, 3–8.

(3) Y. J. Lu, J. Kim, H. Y. Chen, C. Wu, N. Dabidian, C. E. Sanders, C. Y. Wang, M. Y. Lu, B. H. Li, X. Qiu, W. H. Chang, L. J. Chen, G. Shvets, C. K. Shih and S. Gwo, *Science*, 2012, **337**, 450–453.

(4) R. Lu, Y. Wang, W. Wang, L. Gu and J. Sha, *Acta Mater.*, 2014, **79**, 241–247.

(5) Y. Wu, C. Zhang, N. M. Estakhri, Y. Zhao, J. Kim, M. Zhang, X. X. Liu, G. K. Pribil, A. Alù, C. K. Shih and X. Li, *Adv. Mater.*, 2014, **26**, 6106–6110.

(6) W. Lin, T. H. Warren, R. G. Nuzzo and G. S. Girolami, *J. Am. Chem. Soc.*, 1993, **115**, 11644–11645.

(7) A. Grodzicki, I. Łakomska, P. Piszczek, I. Szymańska and E. Szłyk, *Coord. Chem. Rev.*, 2005, **249**, 2232–2258.

(8) K.-H. Park, G. A. Smith, K. Rajan and G.-C. Wang, *Metall. Mater. Trans. A*, 1990, **21A**, 2323–2332.

(9) D. C. Mckenna, G. Wang and K. Rajan, *J. Electron. Mater.*, 1991, **20**, 1–6.

(10) T. B. Hur, H. K. Kim, D. Perello, M. Yun, A. Kulovits and J. Wiezorek, *J. Appl. Phys.*, 2008, **103**, 1–6.

(11) T. B. Hur, H. K. Kim and J. Blachere, *Phys. Rev. B - Condens. Matter Mater. Phys.*, 2007, **75**, 1–5.

(12) D. Kong, L. Jiang and J. Drucker, *J. Appl. Phys.*, 2015, **118**, 213103.

(13) A. Bhukta, P. Guha, A. Ghosh, P. Maiti and P. V. Satyam, *Appl. Phys. A Mater. Sci. Process.*, 2016, **122**, 1–8.

(14) P. Prod'Homme, F. Maroun, R. Cortès and P. Allongue, *Appl. Phys. Lett.*, 2008, **93**, 171901.

(15) J. A. Switzer, J. C. Hill, N. K. Mahenderkar and Y. C. Liu, *ACS Appl. Mater. Interfaces*, 2016, **8**, 15828–15837.

(16) Q. Chen and J. A. Switzer, *ACS Appl. Mater. Interfaces*, 2018, **10**, 21365–21371.

(17) C. M. Hull and J. A. Switzer, *ACS Appl. Mater. Interfaces*, 2018, **10**, 38596–38602.

(18) Y. Duan, S. Rani, Y. Zhang, C. Ni, J. T. Newberg and A. V. Teplyakov, *J. Phys. Chem. C*, 2017, **121**, 7240–7247.

(19) M. Schlesinger, in *Modern Electroplating*, Wiley-Blackwell, 5th edn., 2011, pp. 131–138.

(20) K. Leistner, K. Duschek, J. Zehner, M. Yang, A. Petr, K. Nielsch and K. L. Kavanagh, *J. Electrochem. Soc.*, 2018, **165**, H3076–H3079.

(21) P. Prodhomme, S. Warren, R. Cortès, H. F. Jurca, F. Maroun and P. Allongue, *ChemPhysChem*, 2010, **11**, 2992–3001.

(22) L. Chen, L. Andrea, Y. P. Timalsina, G. C. Wang and T. M. Lu, *Cryst. Growth Des.*, 2013, **13**, 2075–2080.

(23) C. A. Chang, J. C. Liu and J. Angilello, *Appl. Phys. Lett.*, 1990, **57**, 2239–2240.

(24) M. L. Munford, F. Maroun, R. Cortès, P. Allongue and A. A. Pasa, *Surf. Sci.*, 2003, **537**, 95–112.

(25) B. Q. Li and J. M. Zuo, *Surf. Sci.*, 2002, **520**, 7–17.

(26) A. H. M. Abdul Wasey, R. Batabyal, J. C. Mahato, B. N. Dev, Y. Kawazoe and G. P. Das, *Phys. Status Solidi Basic Res.*, 2013, **250**, 1313–1319.

SECTION

2. CONCLUSIONS

The electrodeposition of Au and Ag epitaxial metal films and some of their applications were studied in this work. Epitaxy refers to the growth of crystals on a crystalline substrate that determines their orientation, it can produce highly in-plane and out-of-plane oriented thin films and can elevate the overall efficiency of the device using epitaxial films. The epitaxy Au foils peeled off from the Si surface serve a great example in this case. This work also provides a path to harvest solar energy from the Au films deposited on n-Si surfaces which form a Schottky barrier and serve as photoelectrodes in a regenerative cell.

Paper I introduces the epitaxial electrodeposition of Au thin films on n-type Si using a $HAuCl_4$ bath. A photoelectrochemical regenerative cell is built using Au-Si junction as the photoanode and $Fe^{2+/3+}$ solution as the electrolyte. A maximum photo current density of 11.9 mA cm^{-2} is acquired under 100 mW cm^{-2} light intensity and the effect of the Au layer on the interfacial energetics as well as the stability of the photoelectrode as a function of the Au coverage/thickness is determined. A transparent sulfite solution is also introduced to avoid light absorption by the redox couple ions and bring the photo current density up to 28.5 mA cm^{-2}.

Paper II exhibits a technique for epitaxial lift-off of Au foils as semi-transparent, flexible and single crystal-like substrates for flexible electronics. A Au thin film is first deposited on Si and then photooxidation is performed to create an SiO_x layer in between

the Au and the Si substrate, followed by the lift-off process of the Au foil. The Au foils exhibit as low as 4% increase in resistance after 4000 bending cycles. A flexible OLED was spin-coated on a Au foil taking advantages of the transmittance and flexibility of the foil. An epitaxial diode made of Au/Cu_2O Schottky contact using the Au foils presents a diode quality factor *n* of only 1.6 compared to a polycrystalline diode of $n = 3.1$.

Paper III introduces the electrodeposition of epitaxial Ag thin films on three different orientations of Si surfaces from an acetate bath. A very negative potential of -2.34 V vs. Hg/Hg_2SO_4 is used for pre-polarization and deposition to avoid Si oxidation. A 10 nm thick Ag film is obtained for ten minutes deposition. An epitaxial Ag deposit is also acquired on n-Si(111) using a cyanide bath but the epitaxial deposition of Ag on Si surfaces with other orientation was not successful from the cyanide solution.

REFERENCES

(1) Jayakrishnan, D. S. 5 - Electrodeposition: The Versatile Technique for Nanomaterials. In *Corrosion Protection and Control Using Nanomaterials*; Saji, V. S., Cook, R., Eds.; Woodhead Publishing Series in Metals and Surface Engineering; Woodhead Publishing, 2012; pp 86–125.

(2) Erb, U.; Palumbo, G.; McCrea, J. L. 5 - The Processing of Bulk Nanocrystalline Metals and Alloys by Electrodeposition. In *Nanostructured Metals and Alloys*; Whang, S. H., Ed.; Woodhead Publishing Series in Metals and Surface Engineering; Woodhead Publishing, 2011; pp 118–151.

(3) Schlesinger, M. Electroless and Electrodeposition of Silver. In *Modern Electroplating*; Wiley-Blackwell, 2011; pp 131–138.

(4) Sahoo, P.; Das, S. K.; Davim, J. P. 3.3 Surface Finish Coatings. In *Comprehensive Materials Finishing*; Hashmi, M. S. J., Ed.; Elsevier: Oxford, 2017; pp 38–55.

(5) Poizot, P.; Hung, C.-J.; Nikiforov, M. P.; Bohannan, E. W.; Switzer, J. A. An Electrochemical Method for CuO Thin Film Deposition from Aqueous Solution. *Electrochem. Solid-State Lett.* **2003**, *6* (2), C21.

(6) Switzer, J. A. Galvanostatic Electrodeposition and Microstructure of Copper (I) Oxide Film. *Scr. Mater.* **1998**, *38* (May), 1731–1738.

(7) Liu, R.; Vertegel, A. A.; Bohannan, E. W.; Sorenson, T. A.; Switzer, J. A. Epitaxial Electrodeposition of Zinc Oxide Nanopillars on Single-Crystal Gold. *Chem. Mater.* **2001**, *13* (2), 508–512.

(8) Limmer, S. J.; Kulp, E. A.; Switzer, J. A. Epitaxial Electrodeposition of ZnO on Au(111) from Alkaline Solution: Exploiting Amphoterism in Zn(II). *Langmuir* **2006**, *22* (25), 10535–10539.

(9) Switzer, J. A. Electrochemical Architecture of Ceramic Nanocomposites. *Nanostructured Mater.* **1992**, *1* (1), 43–46.

(10) Switzer, J. A.; Kothari, H. M.; Bohannan, E. W. Thermodynamic to Kinetic Transition in Epitaxial Electrodeposition. *J. Phys. Chem. B* **2002**, *106* (16), 4027–4031.

(11) Liu, R.; Oba, F.; Bohannan, E. W.; Ernst, F.; Switzer, J. A. Shape Control in Epitaxial Electrodeposition: Cu_2O Nanocubes on InP(001). *Chem. Mater.* **2003**, *15* (26), 4882–4885.

(12) Rossnagel, S. M. Thin Film Deposition with Physical Vapor Deposition and Related Technologies. *J. Vac. Sci. Technol. A* **2003**, *21* (5), S74–S87.

(13) Makhlouf, A. S. H. 1 - Current and Advanced Coating Technologies for Industrial Applications. In *Nanocoatings and Ultra-Thin Films*; Makhlouf, A. S. H., Tiginyanu, I., Eds.; Woodhead Publishing Series in Metals and Surface Engineering; Woodhead Publishing, 2011; pp 3–23.

(14) Carlsson, J.-O.; Martin, P. M. Chapter 7 - Chemical Vapor Deposition. In *Handbook of Deposition Technologies for Films and Coatings (Third Edition)*; Martin, P. M., Ed.; William Andrew Publishing: Boston, 2010; pp 314–363.

(15) Shi, Y.; Hamsen, C.; Jia, X.; Kim, K. K.; Reina, A.; Hofmann, M.; Hsu, A. L.; Zhang, K.; Li, H.; Juang, Z. Y.; et al. Synthesis of Few-Layer Hexagonal Boron Nitride Thin Film by Chemical Vapor Deposition. *Nano Lett.* **2010**, *10* (10), 4134–4139.

(16) Franchi, S. Chapter 1 - Molecular Beam Epitaxy: Fundamentals, Historical Background and Future Prospects. In *Molecular Beam Epitaxy*; Henini, M., Ed.; Elsevier: Oxford, 2013; pp 1–46.

(17) Muthe, K. P.; Vyas, J. C.; Kothiyal, G. P.; Gandhi, D. P.; Debnath, A. K.; Gupta, S. K.; Sabharwal, S. C.; Gupta, M. K. Thin Film Deposition of BaO by Molecular Beam Epitaxy. *J. Cryst. Growth* **1992**, *118* (1–2), 213–217.

(18) Sajavaara, T.; Keinonen, J.; Leskelä, M.; Ritala, M.; Kukli, K.; Rahtu, A.; Räisänen, P. I. Atomic Layer Deposition of Oxide Thin Films with Metal Alkoxides as Oxygen Sources. *Science.* **2000**, *288* (5464), 319–321.

(19) Kim, Y.; Kim, M. S.; Yun, H. J.; Ryu, S. Y.; Choi, B. J. Effect of Growth Temperature on AlN Thin Films Fabricated by Atomic Layer Deposition. *Ceram. Int.* **2018**, *44* (14), 17447–17452.

(20) MANER, A.; HARSCH, S.; EHRFELD, W. Mass Production of Microdevices with Extreme Aspect Ratios by Electroforming. *Plat. Surf. Finish.* **1988**, *75* (3), 60–65.

(21) Maner, A.; Ehrfeld, W. Electroforming Techniques In The Liga Process For The Production Of Microdevices. *Mater. Manuf. Process* **1989**, *4*, 527–537.

(22) Chu, W.; Schattenburg, M. L.; Smith, H. I. Low-Stress Gold Electroplating for x-Ray Masks. *Microelectron. Eng.* **1992**, *17* (1–4), 223–226.

(23) Dauksher, W. J.; Resnick, D. J.; Johnson, W. A.; Yanof, A. W. A New Operating Regime for Electroplating the Gold Absorber on X-Ray Masks. *Microelectron. Eng.* **1994**, *23* (1–4), 235–238.

(24) Prod'Homme, P.; Maroun, F.; Cortès, R.; Allongue, P. Electrochemical Growth of Ultraflat Au(111) Epitaxial Buffer Layers on H-Si(111). *Appl. Phys. Lett.* **2008**, *93* (17), 171901.

(25) Switzer, J. A.; Hill, J. C.; Mahenderkar, N. K.; Liu, Y. C. Nanometer-Thick Gold on Silicon as a Proxy for Single-Crystal Gold for the Electrodeposition of Epitaxial Cuprous Oxide Thin Films. *ACS Appl. Mater. Interfaces* **2016**, *8* (24), 15828–15837.

(26) Hull, C. M.; Switzer, J. A. Electrodeposited Epitaxial Cu(100) on Si(100) and Lift-Off of Single Crystal-like Cu(100) Foils. *ACS Appl. Mater. Interfaces* **2018**, *10* (100), 38596–38602.

(27) Chen, Q.; Switzer, J. A. Electrodeposition of Nanometer-Thick Epitaxial Films of Silver onto Single-Crystal Silicon Wafers. *J. Mater. Chem. C* **2019**, *7*, 1720–1725.

(28) Svedberg, E. B.; Mallett, J. J.; Sayan, S.; Shapiro, A. J.; Egelhoff, W. F.; Moffat, T. Recrystallization Texture, Epitaxy, and Magnetic Properties of Electrodeposited FePt on Cu(001). *Appl. Phys. Lett.* **2004**, *85* (8), 1353–1355.

(29) Lay, M. D.; Stickney, J. L. Electrodeposition of Au-Cd Alloy Nanostructures on Au(111). *J. Am. Chem. Soc.* **2003**, *125* (5), 1352–1355.

(30) Saedi, A.; Ghorbani, M. Electrodeposition of Ni–Fe–Co Alloy Nanowire in Modified AAO Template. *Mater. Chem. Phys.* **2005**, *91* (2), 417–423.

(31) Switzer, J. Electrochemical Synthesis of Ceramic Films and Powders. *Am. Ceram. Soc. Bull.* **1987**, *66*, 1521–1525.

(32) Switzer, J. A. Electrodeposited Ceramic Single Crystals. *Science.* **1999**, *284* (5412), 293–296.

(33) Golden, T. D.; Shumsky, M. G.; Zhou, Y.; VanderWerf, R. A.; Van Leeuwen, R. A.; Switzer, J. A. Electrochemical Deposition of Copper(I) Oxide Films. *Chem. Mater.* **1996**, *8* (10), 2499–2504.

(34) Koza, J. A.; Hull, C. M.; Liu, Y. C.; Switzer, J. A. Deposition of β-$Co(OH)_2$ Films by Electrochemical Reduction of Tris(Ethylenediamine)Cobalt(III) in Alkaline Solution. *Chem. Mater.* **2013**, *25* (9), 1922–1926.

(35) Koza, J. A.; He, Z.; Miller, A. S.; Switzer, J. A. Electrodeposition of Crystalline Co3O4 - A Catalyst for the Oxygen Evolution Reaction. *Chem. Mater.* **2012**, *24* (18), 3567–3573.

(36) Sorenson, T. A.; Morton, S. A.; Waddill, G. D.; Switzer, J. A. Epitaxial Electrodeposition of Fe3O4thin Films on the Low-Index Planes of Gold. *J. Am. Chem. Soc.* **2002**, *124* (25), 7604–7609.

(37) McIntyre, J.D.E.; W.F.Peck, J. Electrodeposition of Gold Depolarization Effects Induced by Heavy Metal Ions. *J. Electrochem. Soc.* **1975**, *123* (12), 1800–1813.

(38) Cheh, H. Y. Electrodeposition of Gold by Pulsed Current. *J. Electrochem. Soc.* **1971**, *118* (4), 551–557.

(39) Escalona-Villalpando, R. A.; Gurrola, M. P.; Trejo, G.; Guerra-Balcázar, M.; Ledesma-García, J.; Arriaga, L. G. Electrodeposition of Gold on Oxidized and Reduced Graphite Surfaces and Its Influence on Glucose Oxidation. *J. Electroanal. Chem.* **2018**, *816* (November 2017), 92–98.

(40) Olson, T. S.; Atanassov, P.; Brevnov, D. A. Electrodeposition of Gold Particles on Aluminum Substrates Containing Copper. *J. Phys. Chem. B* **2005**, *109* (3), 1243–1250.

(41) Green, T. A. Gold Electrodeposition for Microelectronic, Optoelectronic and Microsystem Applications. *Gold Bull.* **2007**, *40* (2), 105–114.

(42) Chen, Q.; Switzer, J. A. Photoelectrochemistry of Ultrathin, Semitransparent, and Catalytic Gold Films Electrodeposited Epitaxially onto n-Silicon (111). *ACS Appl. Mater. Interfaces* **2018**, *10* (25), 21365–21371.

(43) Mahenderkar, N. K.; Chen, Q.; Liu, Y.-C.; Duchild, A. R.; Hofheins, S.; Chason, E.; Switzer, J. A. Epitaxial Lift-off of Electrodeposited Single-Crystal Gold Foils for Flexible Electronics. *Science.* **2017**, *355* (6330), 1203–1206.

(44) Wu, Y.; Zhang, C.; Estakhri, N. M.; Zhao, Y.; Kim, J.; Zhang, M.; Liu, X. X.; Pribil, G. K.; Alù, A.; Shih, C. K.; et al. Intrinsic Optical Properties and Enhanced Plasmonic Response of Epitaxial Silver. *Adv. Mater.* **2014**, *26* (35), 6106–6110.

(45) Lu, Y. J.; Kim, J.; Chen, H. Y.; Wu, C.; Dabidian, N.; Sanders, C. E.; Wang, C. Y.; Lu, M. Y.; Li, B. H.; Qiu, X.; et al. Plasmonic Nanolaser Using Epitaxially Grown Silver Film. *Science.* **2012**, *337* (6093), 450–453.

(46) Lu, R.; Wang, Y.; Wang, W.; Gu, L.; Sha, J. Epitaxial Growth of Silver Nanoislands on the Surface of Silicon Nanowires in Ambient Air. *Acta Mater.* **2014**, *79*, 241–247.

(47) Coluccio, M. L.; Das, G.; Mecarini, F.; Gentile, F.; Pujia, A.; Bava, L.; Tallerico, R.; Candeloro, P.; Liberale, C.; Angelis, F. De; et al. Silver-Based Surface Enhanced Raman Scattering (SERS) Substrate Fabrication Using Nanolithography and Site Selective Electroless Deposition. *Microelectron. Eng.* **2009**, *86* (4), 1085–1088.

(48) Duan, Y.; Rani, S.; Zhang, Y.; Ni, C.; Newberg, J. T.; Teplyakov, A. V. Silver Deposition onto Modified Silicon Substrates. *J. Phys. Chem. C* **2017**, *121* (13), 7240–7247.

(49) Larciprete, M. C.; Albertoni, A.; Belardini, A.; Leahu, G.; Li Voti, R.; Mura, F.; Sibilia, C.; Nefedov, I.; Anoshkin, I. V; Kauppinen, E. I.; et al. Infrared Properties of Randomly Oriented Silver Nanowires. *J. Appl. Phys.* **2012**, *112* (8), 83503.

(50) Zarkadas, G. M.; Stergiou, A.; Papanastasiou, G. Silver Electrodeposition from $AgNO_3$ Solutions Containing Organic Additives : – Methanol Solvent Systems in the Presence of Electrodeposition from Binary Water – Tartaric Acid. *J. Appl. Electrochem.* **2004**, 607–615.

(51) Xie, B.-G.; Sun, J.-J.; Lin, Z.-B.; Chen, G.-N. Electrodeposition of Mirror-Bright Silver in Cyanide-Free Bath Containing Uracil as Complexing Agent Without a Separate Strike Plating Process. *J. Electrochem. Soc.* **2009**, *156* (3), D79.

(52) De Oliveira, G. M.; Silva, M. R.; Carlos, I. A. Voltammetric and Chronoamperometric Studies of Silver Electrodeposition from a Bath Containing HEDTA. *J. Mater. Sci.* **2007**, *42* (24), 10164–10172.

(53) Lin, Z. Bin; Xie, B. G.; Chen, J. S.; Sun, J. J.; Chen, G. N. Nucleation Mechanism of Silver during Electrodeposition on a Glassy Carbon Electrode from a Cyanide-Free Bath with 2-Hydroxypyridine as a Complexing Agent. *J. Electroanal. Chem.* **2009**, *633* (1), 207–211.

(54) Liu, A.; Ren, X.; Zhang, J.; Li, D.; An, M. Complexing Agent Study for Environmentally Friendly Silver Electrodeposition(II): Electrochemical Behavior of Silver Complex. *RSC Adv.* **2016**, *6* (9), 7348–7355.

(55) Friedrich, J. Methods for Bulk Growth of Inorganic Crystals: Crystal Growth. In *Reference Module in Materials Science and Materials Engineering*; Elsevier, 2016.

(56) Andeen, D.; Loeffler, L.; Padture, N.; Lange, F. F. Crystal Chemistry of Epitaxial ZnO on (1 1 1) $MgAl_2O_4$ Produced by Hydrothermal Synthesis. *J. Cryst. Growth* **2003**, *259* (1–2), 103–109.

(57) Sengupta, S.; Templeman, T.; Chen, C.; Moon, E.; Shandalov, M.; Ezersky, V.; Phillips, J.; Golan, Y. Chemical Epitaxy and Interfacial Reactivity in Solution Deposited PbS on ZnTe. *J. Mater. Chem. C* **2016**, *4* (10), 1996–2002.

(58) Froment, M.; Bernard, M. C.; Cortes, R.; Mokili, B.; Lincot, D. Study of CdS Epitaxial Films Chemically Deposited from Aqueous Solutions on InP Single Crystals. *J. Electrochem. Soc.* **1995**, *142* (8), 2642–2649.

(59) Johnson, G. W. Some Observations on the Epitaxy of Sodium Chloride on Silver. *J. Appl. Phys.* **1950**, *21* (10), 1057–1062.

(60) Johnson, G. W. The Epitaxy of Alkali Chlorides on Metals. *J. Appl. Phys.* **1951**, *22* (6), 797–805.

(61) Pashley, D. W. Epitaxy Growth Mechanisms. *Mater. Sci. Technol.* **1999**, *15* (1), 2–8.

(62) Tsuda, M.; Nakajima, M.; Oikawa, S. Epitaxial Growth Mechanism of Diamond Crystal in CH_4-H_2 Plasma. *J. Am. Chem. Soc.* **1986**, *108* (19), 5780–5783.

(63) La Via, F.; Camarda, M.; La Magna, A. Mechanisms of Growth and Defect Properties of Epitaxial SiC. *Appl. Phys. Rev.* **2014**, *1* (3), 31301.

(64) Yang, H.; Wang, W.; Liu, Z.; Yang, W.; Li, G. Epitaxial Growth Mechanism of Pulsed Laser Deposited AlN Films on Si (111) Substrates. *CrystEngComm* **2014**, *16* (15), 3148–3154.

(65) Konuma, M. Feature and Mechanisms of Layer Growth in Liquid Phase Epitaxy of Semiconductor Materials. In *Chemical Physics of Thin Film Deposition Processes for Micro- and Nano-Technologies*; Pauleau, Y., Ed.; Springer Netherlands: Dordrecht, 2002; pp 43–68.

(66) Nozik, A. J. Photoelectrochemistry: Applications to Solar Energy Conversion. *Annu. Rev. Phys. Chem.* **1978**, *29* (1), 189–222.

(67) Jin, S. What Else Can Photoelectrochemical Solar Energy Conversion Do Besides Water Splitting and CO2 Reduction? *ACS Energy Lett.* **2018**, *3* (10), 2610–2612.

(68) FUJISHIMA, A.; HONDA, K. Electrochemical Photolysis of Water at a Semiconductor Electrode. *Nature* **1972**, *238* (5358), 37–38.

(69) Walter, M. G.; Warren, E. L.; McKone, J. R.; Boettcher, S. W.; Mi, Q.; Santori, E. A.; Lewis, N. S. Solar Water Splitting Cells. *Chem. Rev.* **2010**, *110* (11), 6446–6473.

(70) Michael Grätzel. Photoelectrochemical Cells. *Nature* **2001**, *414*, 338–344.

(71) Kang, D.; Kim, T. W.; Kubota, S. R.; Cardiel, A. C.; Cha, H. G.; Choi, K. S. Electrochemical Synthesis of Photoelectrodes and Catalysts for Use in Solar Water Splitting. *Chem. Rev.* **2015**, *115* (23), 12839–12887.

(72) Musiani, M.; Furlanetto, F.; Bertoncello, R. Electrodeposited PbO_2 + RuO_2 : A Composite Anode for Oxygen Evolution from Sulphuric Acid Solution. *J. Electroanal. Chem.* **1999**, *465*, 160–167.

(73) Yagi, M.; Tomita, E.; Kuwabara, T. Remarkably High Activity of Electrodeposited IrO 2 Film for Electrocatalytic Water Oxidation. *J. Electroanal. Chem.* **2005**, *579*, 83–88.

(74) Blakemore, J. D.; Schley, N. D.; Olack, G. W.; Incarvito, C. D.; Brudvig, G. W.; Crabtree, R. H. Anodic Deposition of a Robust Iridium-Based Water-Oxidation Catalyst from Organometallic Precursors. *Chem. Sci.* **2011**, *2* (1), 94–98.

(75) Blakemore, J. D.; Mara, M. W.; Kushner-Lenhoff, M. N.; Schley, N. D.; Konezny, S. J.; Rivalta, I.; Negre, C. F. A.; Snoeberger, R. C.; Kokhan, O.; Huang, J.; et al. Characterization of an Amorphous Iridium Water-Oxidation Catalyst Electrodeposited from Organometallic Precursors. *Inorg. Chem.* **2013**, *52* (4), 1860–1871.

(76) Zhao, C.; Yu, H.; Li, Y.; Li, X.; Ding, L.; Fan, L. Electrochemical Controlled Synthesis and Characterization of Well-Aligned IrO2 Nanotube Arrays with Enhanced Electrocatalytic Activity toward Oxygen Evolution Reaction. *J. Electroanal. Chem.* **2013**, *688*, 269–274.

(77) Liu, Y. C.; Koza, J. A.; Switzer, J. A. Conversion of Electrodeposited $Co(OH)_2$ to CoOOH and Co_3O_4, and Comparison of Their Catalytic Activity for the Oxygen Evolution Reaction. *Electrochim. Acta* **2014**, *140*, 359–365.

(78) Hill, J. C.; Landers, A. T.; Switzer, J. A. An Electrodeposited Inhomogeneous Metal-Insulator-Semiconductor Junction for Efficient Photoelectrochemical Water Oxidation. *Nat. Mater.* **2015**, *14* (11), 1150–1155.

(79) Cao, X.; Hong, Y.; Zhang, N.; Chen, Q.; Masud, J.; Zaeem, M. A.; Nath, M. Phase Exploration and Identification of Multinary Transition-Metal Selenides as High-Efficiency Oxygen Evolution Electrocatalysts through Combinatorial Electrodeposition. *ACS Catal.* **2018**, *8*, 8273–8289.

(80) Masud, J.; Liyanage, W. P. R.; Cao, X.; Saxena, A.; Nath, M. Copper Selenides as High-Efficiency Electrocatalysts for Oxygen Evolution Reaction. *ACS Appl. Energy Mater.* **2018**, *1* (8), 4075–4083.

(81) Cao, X.; Johnson, E.; Nath, M. Identifying High-Efficiency Oxygen Evolution Electrocatalysts from Co–Ni–Cu Based Selenides through Combinatorial Electrodeposition. *J. Mater. Chem. A* **2019**.

(82) Licht, S. Multiple Band Gap Semiconductor/Electrolyte Solar Energy Conversion. *J. Phys. Chem. B* **2001**, *105* (27), 6281–6294.

(83) Sze, S. M. *Physics of Semiconductor Devices*, 3rd Ed.; Wiley-Interscience, Inc.: New York, 2007.

(84) Liao, S.; Shi, J.; Ding, C.; Liu, M.; Xiong, F.; Wang, N.; Chen, J.; Li, C. Photoelectrochemical Regeneration of All Vanadium Redox Species for Construction of a Solar Rechargeable Flow Cell. *J. Energy Chem.* **2018**, *27* (1), 278–282.

(85) Ray, K. A. Flexible Solar Cell Arrays for Increased Space Power. *IEEE Trans. Aerosp. Electron. Syst.* **1967**, *AES-3* (1), 107–115.

(86) Yu, K. J.; Yan, Z.; Han, M.; Rogers, J. A. Inorganic Semiconducting Materials for Flexible and Stretchable Electronics. *npj Flex. Electron.* **2017**, *1* (1), 4.

(87) Sun, Y.; Rogers, J. A. Inorganic Semiconductors for Flexible Electronics. *Adv. Mater.* **2007**, *19* (15), 1897–1916.

(88) Gates, B. D. Flexible Electronics. *Science.* **2009**, *323* (5921), 1566–1567.

(89) Xu, S.; Yan, Z.; Jang, K.-I.; Huang, W.; Fu, H.; Kim, J.; Wei, Z.; Flavin, M.; McCracken, J.; Wang, R.; et al. Assembly of Micro/Nanomaterials into Complex, Three-Dimensional Architectures by Compressive Buckling. *Science.* **2015**, *347* (6218), 154–159.

(90) Yoon, J.; Baca, A. J.; Park, S.-I.; Elvikis, P.; Geddes III, J. B.; Li, L.; Kim, R. H.; Xiao, J.; Wang, S.; Kim, T.-H.; et al. Ultrathin Silicon Solar Microcells for Semitransparent, Mechanically Flexible and Microconcentrator Module Designs. *Nat. Mater.* **2008**, *7*, 907.

(91) Nathan, A.; Ahnood, A.; Cole, M. T.; Lee, S.; Suzuki, Y.; Hiralal, P.; Bonaccorso, F.; Hasan, T.; Garcia-Gancedo, L.; Dyadyusha, A.; et al. Flexible Electronics: The Next Ubiquitous Platform. *Proc. IEEE* **2012**, *100* (Special Centennial Issue), 1486–1517.

(92) Cheng, I.-C.; Wagner, S. Overview of Flexible Electronics Technology. In *Flexible Electronics: Materials and Applications*; Wong, W. S., Salleo, A., Eds.; Springer US: Boston, MA, 2009; pp 1–28.

(93) Guillén, C.; Herrero, J. TCO/Metal/TCO Structures for Energy and Flexible Electronics. *Thin Solid Films* **2011**, *520* (1), 1–17.

(94) Plichta, A.; Habeck, A.; Knoche, S.; Kruse, A.; Weber, A.; Hildebrand, N. Flexible Glass Substrates. In *Flexible Flat Panel Displays*; John Wiley & Sons, Ltd, 2005; pp 35–55.

(95) Cui, Y.; Hu, L. B.; Kim, H. S.; Lee, J. Y.; Peumans, P. Scalable Coating and Properties of Transparent, Flexible, Silver Nanowire Electrodes. *ACS Nano* **2010**, *4* (5), 2955–2963.

(96) Kim, D.-J.; Kim, H.-J.; Seo, K.-W.; Kim, K.-H.; Kim, T.-W.; Kim, H.-K. Indium-Free, Highly Transparent, Flexible $Cu_2O/Cu/Cu_2O$ Mesh Electrodes for Flexible Touch Screen Panels. *Sci. Rep.* **2015**, *5*, 16838.

(97) Maurer, J. H. M.; González-García, L.; Reiser, B.; Kanelidis, I.; Kraus, T. Templated Self-Assembly of Ultrathin Gold Nanowires by Nanoimprinting for Transparent Flexible Electronics. *Nano Lett.* **2016**, *16* (5), 2921–2925.

(98) Dasgupta, N. P.; Sun, J.; Liu, C.; Brittman, S.; Andrews, S. C.; Lim, J.; Gao, H.; Yan, R.; Yang, P. 25th Anniversary Article: Semiconductor Nanowires – Synthesis, Characterization, and Applications. *Adv. Mater.* **2014**, *26* (14), 2137–2184.

(99) Zardetto, V.; Brown, T. M.; Reale, A.; Di Carlo, A. Substrates for Flexible Electronics: A Practical Investigation on the Electrical, Film Flexibility, Optical, Temperature, and Solvent Resistance Properties. *J. Polym. Sci. Part B Polym. Phys.* **2011**, *49* (9), 638–648.

(100) Nyholm, L.; Nyström, G.; Mihranyan, A.; Strømme, M. Toward Flexible Polymer and Paper-Based Energy Storage Devices. *Adv. Mater.* **2011**, *23* (33), 3751–3769.

(101) Snook, G. A.; Kao, P.; Best, A. S. Conducting-Polymer-Based Supercapacitor Devices and Electrodes. *J. Power Sources* **2011**, *196* (1), 1–12.

(102) Benight, S. J.; Wang, C.; Tok, J. B. H.; Bao, Z. Stretchable and Self-Healing Polymers and Devices for Electronic Skin. *Prog. Polym. Sci.* **2013**, *38* (12), 1961–1977.

(103) Bi, Y. G.; Feng, J.; Ji, J. H.; Chen, Y.; Liu, Y. S.; Li, Y. F.; Liu, Y. F.; Zhang, X. L.; Sun, H. B. Ultrathin and Ultrasmooth Au Films as Transparent Electrodes in ITO-Free Organic Light-Emitting Devices. *Nanoscale* **2016**, *8* (19), 10010–10015.

(104) O'Connor, B.; Haughn, C.; An, K.-H.; Pipe, K. P.; Shtein, M. Transparent and Conductive Electrodes Based on Unpatterned, Thin Metal Films. *Appl. Phys. Lett.* **2008**, *93* (22), 223304.

(105) Jin, Y.; Feng, J.; Zhang, X.-L.; Xu, M.; Bi, Y.-G.; Chen, Q.-D.; Wang, H.-Y.; Sun, H.-B. Surface-Plasmon Enhanced Absorption in Organic Solar Cells by Employing a Periodically Corrugated Metallic Electrode. *Appl. Phys. Lett.* **2012**, *101* (16), 163303.

(106) Zhang, C.; Zhao, D.; Gu, D.; Kim, H.; Ling, T.; Wu, Y.-K. R.; Guo, L. J. An Ultrathin, Smooth, and Low-Loss Al-Doped Ag Film and Its Application as a Transparent Electrode in Organic Photovoltaics. *Adv. Mater.* **2014**, *26* (32), 5696–5701.

(107) Zou, J.; Li, C.-Z.; Chang, C.-Y.; Yip, H.-L.; Jen, A. K.-Y. Interfacial Engineering of Ultrathin Metal Film Transparent Electrode for Flexible Organic Photovoltaic Cells. *Adv. Mater.* **2014**, *26* (22), 3618–3623.

(108) Yoo, J.; Jung, S.; Kim, Y.; Byun, S.; Kim, J.; Choi, N.; Yoon, S.; Kim, C.; Hwang, Y.; Chung, I. Highly Flexible AM-OLED Display With Integrated Gate Driver Using Amorphous Silicon TFT on Ultrathin Metal Foil. *J. Disp. Technol.* **2010**, *6* (11), 565–570.

(109) Gao, F. G.; Bard, A. J. Solid-State Organic Light-Emitting Diodes Based on Tris(2,2'-Bipyridine)Ruthenium(II) Complexes. *J. Am. Chem. Soc.* **2000**, *122* (30), 7426–7427.

(110) Formica, N.; Ghosh, D. S.; Carrilero, A.; Chen, T. L.; Simpson, R. E.; Pruneri, V. Ultrastable and Atomically Smooth Ultrathin Silver Films Grown on a Copper Seed Layer. *ACS Appl. Mater. Interfaces* **2013**, *5* (8), 3048–3053.

VITA

Qingzhi Chen was born in 1990, in Lanzhou, Gansu province, China. Qingzhi Chen obtained his Bachelor of Science degree in Material Science at University of Science and Technology of China in Hefei, Anhui in 2013. During his undergraduate studies, he received research training as an intern at Institute of Modern Physics, Chinese Academy of Science for Nano-material science such as metal nanowire synthesis, Nano-material characterization and surface enhanced Raman scattering (SERS) effect on Au nanowire arrays. This also became part of his undergraduate thesis. In 2013, he was accepted in the chemistry department at Missouri University of Science Technology in Rolla, Missouri. He joined Prof. Jay A. Switzer's lab as a PhD student in August of 2013 working on electrodeposition and characterization of metallic/magnetic nanostructures and epitaxial thin films for energy conversion and flexible electronics. During his PhD, his work on epitaxial gold film on silicon as photoelectrode was published in ACS applied materials and interfaces journal. His work collaborated with group members on flexible single-crystal Au foil which was published in Science journal, and was also highlighted on the U.S. Department of Energy website and the MRS bulletin. He received his PhD in Chemistry from Missouri University of Science and Technology in July 2019.